3D MODELLING OF A TIDAL TURBINE – A NUMERICAL INVESTIGATION OF WAKE PHENOMENA

by

Nicholas A. G. Osbourne

Submitted in partial fulfilment of the requirements
for the degree of Master of Applied Science

at

Dalhousie University
Halifax, Nova Scotia
August 2015

"Consider again that dot. That's here. That's home. That's us. On it everyone you love, everyone you know, everyone you ever heard of, every human being who ever was, lived out there lives. The aggregate of our joy and suffering, thousands of confident religions, ideologies, and economic doctrines, every hunter and forager, every hero and coward, every creator and destroyer of civilizations, every king and peasant, every young couple in love, every mother and father, hopeful child, inventor and explorer, every teacher of morals, every corrupt politician, every "superstar", every "supreme leader", every saint and sinner in the history of our species lived there – on a mote of dust suspended in a sunbeam.

To me, it underscores our responsibility to deal more kindly with one another, and to preserve and cherish the pale blue dot… The only home we've ever known."

-Carl Sagan

Table of Contents

List of Tables

List of Figures

Abstract

A three-dimensional CFD model of a tidal turbine was successfully created. The effect of physical parameters, such as twist axis location and blade trailing edge roundness, were discussed. These were found to have a significant impact on the turbine performance. A mesh convergence study was performed to ensure that wake physics is properly resolved. Likewise, a domain length study ensured a full wake recovery. Model validation was completed wherein the turbine performance was compared to experimental data. The impact of blockage was investigated by increasing the cross-sectional domain size. This exhibited minimal impact on turbine performance but greatly affected wake recovery. It was found that blade tip shed vortices are a major contributor to wake recovery. Blockage impeded this contribution, advecting the wake downstream. A complete wake recovery was modelled for a range of TSRs and a preliminary relation between turbine rotation rate and wake recovery distance was determined.

List of Abbreviations and Symbols Used

Dimensional variables

A	Rotor swept area (m^2)
A_C	Channel area (m^2)
c	Chord length (m)
d	Water depth (m)
D	Diameter of turbine (m)
F_D	Drag force (N)
F_L	Lift force (N)
g	Acceleration due to gravity (m/s^2)
k	Turbulence kinetic energy (m^2/s^2)
L	Characteristic length (m)
p_0	Free-stream pressure (Pa)
p_v	Vapour pressure (Pa)
P	Power (W)
P	Pressure (Pa)
$\bar{P}$	Time-averaged pressure (Pa)
P_{rel}	Relative Pressure (Pa)
Q	Torque (Nm)
r	Local blade radius (m)
R	Radius of turbine (m)
t	Blade thickness (m)
u	Velocity – x direction (m/s)
$\bar{u}$	Time-averaged velocity component – x direction (m/s)

u'	Fluctuating velocity component – x direction (m/s)
v	Velocity – y direction (m/s)
$\bar{v}$	Time-averaged velocity component – y direction (m/s)
v'	Fluctuating velocity component – y direction (m/s)
V_0	Free-stream velocity (m/s)
V	Velocity (m/s)
V_A	Apparent velocity (m/s)
V_B	Blade velocity (m/s)
V_T	True velocity (m/s)
V_{Turb}	Velocity at the turbine (m/s)
V_w	Velocity in the wake (m/s)
w	Velocity – z direction (m/s)
$\bar{w}$	Time-averaged velocity component – z direction (m/s)
w'	Fluctuating velocity component – z direction (m/s)

Dimensionless numbers

a	Axial induction factor
B_r	Blockage ratio (%)
C_P	Power coefficient
C_T	Thrust coefficient
Fr	Froude number
I	Turbulence intensity (%)
Re	Reynolds number
Re_D	Reynolds number based on diameter (VD/υ)

Re_C	Reynolds number based on chord length (VD/υ)
$V_{deficit}$	Velocity deficit
y^+	Y plus
Δy_p	Distance between the first and second grid points off the wall

Greek letters

α	Angle of attack (°)
β	Blade pitch angle (°)
ε	Turbulence eddy dissipation (m^2/s^3)
μ	Molecular (dynamic) viscosity (kg/m·s)
μ_{eff}	Effective viscosity (kg/m·s)
μ_t	Turbulent viscosity (kg/m·s)
υ	Kinematic viscosity (m^2/s)
ρ	Density (kg/m^3)
σ	Cavitation number
τ_w	Wall shear stress (Pa)
τ'_{xx}	Reynolds stress (Pa)
τ'_{xy}	Reynolds stress (Pa)
τ'_{xz}	Reynolds stress (Pa)
Φ	Incidence angle (°)
ω	Turbine rotation rate (rad/s)
ω	Turbulent frequency (s^{-1})
$\vec{\omega}$	Vorticity (s^{-1})

Turbulence model constants

a_1	Turbulence model constant
$C_{\varepsilon 1}$	Turbulence model constant
$C_{\varepsilon 2}$	Turbulence model constant
C_{μ}	Turbulence model constant
$CD_{k\omega}$	Turbulence model constant
F_1	Turbulence model blending factor
F_2	Turbulence model blending factor
P_{kb}	Influence of buoyancy forces
$P_{\varepsilon b}$	Influence of buoyancy forces
P_k	Turbulence production due to viscous forces
S	Invariant measure of the strain rate
α	Turbulence model constant
β	Turbulence model constant
β	Blend factor
β'	Turbulence model constant
ν_t	Turbulence model limiter
σ_k	Turbulence model constant
σ_{ε}	Turbulence model constant
σ_{ω}	Turbulence model constant
$\sigma_{\omega 2}$	Turbulence model constant
Φ_1	Turbulence model blending factor
Φ_2	Turbulence model blending factor
Φ_3	Turbulence model blending factor

Acronyms and abbreviations

BEMT	Blade element momentum theory
CEL	CFX expression language
CFD	Computational fluid dynamics
DES	Detached eddy simulation
DNS	Direct numerical simulation
HATT	Horizontal axis tidal turbine
HAWT	Horizontal axis wind turbine
LES	Large-eddy simulations
LRR	Launder-Reece-Rodi
NACA	The National Advisory Committee for Aeronautics
RANS	Reynolds Averaged Navier-Stokes
SST	Shear stress transport
TSR	Tip speed ratio
VATT	Vertical Axis Tidal Turbine

Acknowledgements

Foremost, I would like to acknowledge my supervisor Dr. Dominic Groulx and my committee members Dr. Jan Haelssig and Dr. Sue Molly. Dom, thank you for your continual support, inspiration and direction throughout my undergrad and graduate studies. Jan and Sue, your willingness to lend a hand when needed was, and is, much appreciated.

I am grateful for the support and encouragement of my family and friends. To Mom and Dad, thank you for fueling my sense of exploration; whether it be hunting for leprechauns, learning different musical instruments or trying to harness the power of the tides. To my love, Heather, you are the constant that got me through this chapter of my life. I would not have been able to achieve what I have without your support. Thanks to the LAMTE crew for seeing me through this: Ben, Louis, Trevor, Moe, Laura, Ali and Tousif. Robynne, many turning points throughout this project were a result of discussions with you; thank you for being there. And thanks to Katie, across the pond at Strathclyde; your friendship and passion for knowledge acted as an inspiration for me. Joel, I have found much enjoyment in our newfound friendship. I am glad that we will be walking across that stage together.

I was fortunate to have the opportunity to spend a semester at the University of Tasmania. Irene, thank you for your support during this time. Your guidance, kindness and hospitality were welcome. I owe much to Phil, Leong and Max for their encouragement and advice during the semester and later with my thesis work. Similar thanks goes to Arno and Aiden; good luck to you both in your schooling and future endeavours.

Lastly, this thesis would not be possible without the financial help of OERA, NSERC and CFI. Their continual support provided me with not only the necessary equipment but also invaluable learning opportunities that would not have arisen otherwise.

CHAPTER 1 INTRODUCTION

1.1. MARINE ENERGY IN THE GLOBAL ENERGY MARKET

Today's global energy market is heavily dominated by fossil fuels. In 2012, the combustion of fossil fuels accounted for 81% of global energy consumption, a slight reduction from 86.7% in 1973 (International Energy Agency, 2014). Total energy consumption is rising dramatically however, increasing two-fold during this span. The energy mix in 2012 consisted of 31.4% oil, 29% coal, 21.3% natural gas, 10% biofuels and waste, 4.8% nuclear, 2.4% hydroelectric, and the remainder (1.1%) from sources such as geothermal, solar and wind. This heavy reliance on fossil fuels is a cause for concern as these sources are inherently finite and their combustion have an indisputable impact on the ecology of our planet. A result of this is the increasing emphasis on the advancement of renewable and sustainable energy industries. Some of these industries, such as on-shore wind, are relatively well established. For example, optimal turbine, generator and tower designs, along with installation and upkeep methodologies, are well accepted. Marine energy industries on the other hand are relatively untapped energy sources and perceptions of approaches and optimal designs vary. Fortunately, initial stage complications can be reduced with lessons learned from other industries.

Marine energy (namely tidal, wave, and ocean thermal) is subject to physical challenges that are not seen in other energy industries. These disincentives include a high fluid density, water salinity, extreme turbulence, environmental impact issues, poor accessibility and high costs of deployment, operation and maintenance. Despite this, marine energy can make for attractive energy sources as they each exhibit their distinct benefits. Tidal energy distinguishes itself in that it is cyclic in nature, being driven by the gravitational pull of the moon and sun. Tides are also decidedly predictable with a high level of accuracy spanning several years in the future. The combination of these attributes make tidal energy appealing, especially for providing a steady base load to electrical grids when adequate storage is available.

There are two prominent methods of extracting energy from the tides: tidal barrages and in-stream tidal turbines. Tidal barrages operate similarly to hydro-electric dams in that they impound water and utilize the potential head difference at ebb tide to generate electricity. This technology has been demonstrated at the 240 MW La Rance barrage in Brittany, France, since 1966. More recently in Sihwa Lake, South Korea, a barrage of capacity 254 MW took advantage of an existing seawall and began operation in 2011, and is to date the world's largest tidal power plant. Canada also operates the only tidal generating plant in North America at the Annapolis Royal Generating Station, a barrage type technology with a capacity of 20 MW located in the Annapolis Basin in Nova Scotia. Challenges to this technology are daunting however and include a significant initial capital investment, local ecological changes on the inland side of the wall and impact to tidal flows on the grander scale. The quantity of materials needed for the wall to withstand the constant loading and the construction costs are seen as major issues facing this technology (Etemadi *et al.*, 2011). The greater shortcoming to barrage systems is their impact on the local ecology. It is expected that walling off a bay or estuary would significantly reduce its flushing rate. This is detrimental to the native marine life as an increase in salinity, changes in turbidity and higher concentrations of pollutants are potential implications (Hooper & Austen, 2013). In fact, due to reduced tidal flushing, an increase in nutrient concentration is expected which could lead to risks of eutrophication (algal blooms). The combination of this, and an increase in pollutants, are thought to have a negative impact in local seafood supply chains as well. In the case of the Sihwa Lake barrage however, the retrofit design of a seawall greatly reduced pollution concentration. Prior to the barrage installation, due to a cut-off from tidal currents, a rapid increase in population and industrial waste loads, the pollution level was considered severe. In re-opening the lake to tidal currents a reduction in pollution has been observed and is expected to play a role in restoring the Lake Sihwa ecosystem (Park, 2007). Finally, relevant to the Bay of Fundy, models suggest that adding a barrage type barrier to the Minas Passage could shift tides towards resonance, increasing the tidal amplitude by 20 to 30 percent along the coast of Maine and Massachusetts (Karsten *et al.*, 2008).

Alternatively, in-stream tidal energy devices operate by utilizing the kinetic energy, rather than potential energy, of the flow. This means that they are able to take advantage of

natural bathymetry which channels tidal flow, creating high velocities. In-stream devices also avoid the aforementioned issues of reduced tidal flushing as, in most cases, tidal walls are not used. Compared to tidal barrages, in-stream tidal devices are in their infancy and current designs vary greatly. In general, two types of turbines are being developed:

- Horizontal axis tidal current turbines – The turbine blades rotate about a horizontal axis that is parallel with the incoming flow;
- Vertical axis tidal current turbines – The turbine blades rotate about a vertical axis that is perpendicular to the incoming flow.

Support structure designs vary as well, with three notable options. The first is a gravity base which consists of a large mass, generally steel and/or concrete, that holds the turbine to the seabed. Second is the pile structure which is pinned to the seabed at one or more locations. Third is the floating structure that is moored to the seabed. The first two benefit by being out of eyesight, or "invisible". Due to the shear effect however, see Fig. 1.1, these turbines may only access a small percentage of the available energy. It is possible as well that they may be damaged or have reduced performance as a result of sediment transport. A floating structure avoids these issues but will have mooring challenges, possible break-away problems, storm effects and will be visible at sea level.

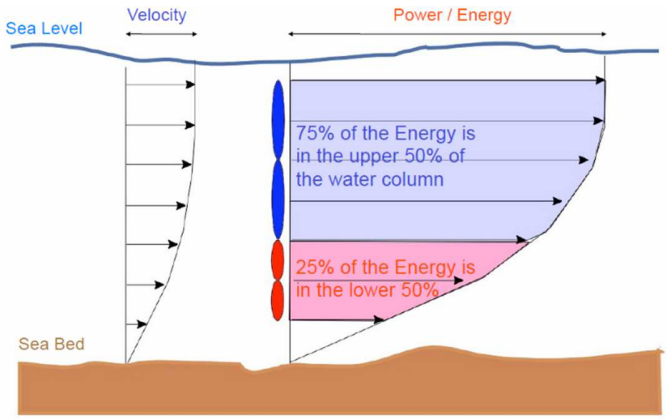

FIGURE 1.1: DEMONSTRATION OF THE SHEAR EFFECT

Figure 1.2 demonstrates some of these variations in design aspects. For example, OpenHydro (a) and Atlantis (c) have subsea based turbines while Black Rock Tidal Power (b) and Minas Energy (d) have floating, or semi-submerged, devices. a) has stationary

blades and b) employs passively pitching blades while c) and d) take advantage of actively pitching blades. Ebb and flow tides are enjoyed by: a) stationary turbine base aligned with the predominant tidal flow, b) passively yawing structure, c) actively yawing structure, and d) actively pitching blades to 180°. Finally, b), c), and d) utilize varying numbers of three bladed turbines while a) employs a ten bladed turbine. For design demonstration and analysis, these four turbines are set to be installed at The Fundy Ocean Research Centre for Energy (FORCE) in Parrsboro, Nova Scotia. FORCE provides the berths and electrical infrastructure for turbine developers to deploy, monitor and operate their devices at full-scale. A similar facility is the European Marine Energy Centre (EMEC), based in Orkney, Scotland which has been operating as a tidal turbine testing facility since May 2005. Centres like these are able to offer turbine developers the opportunity to test full-scale grid-connected prototype devices in a true marine environment.

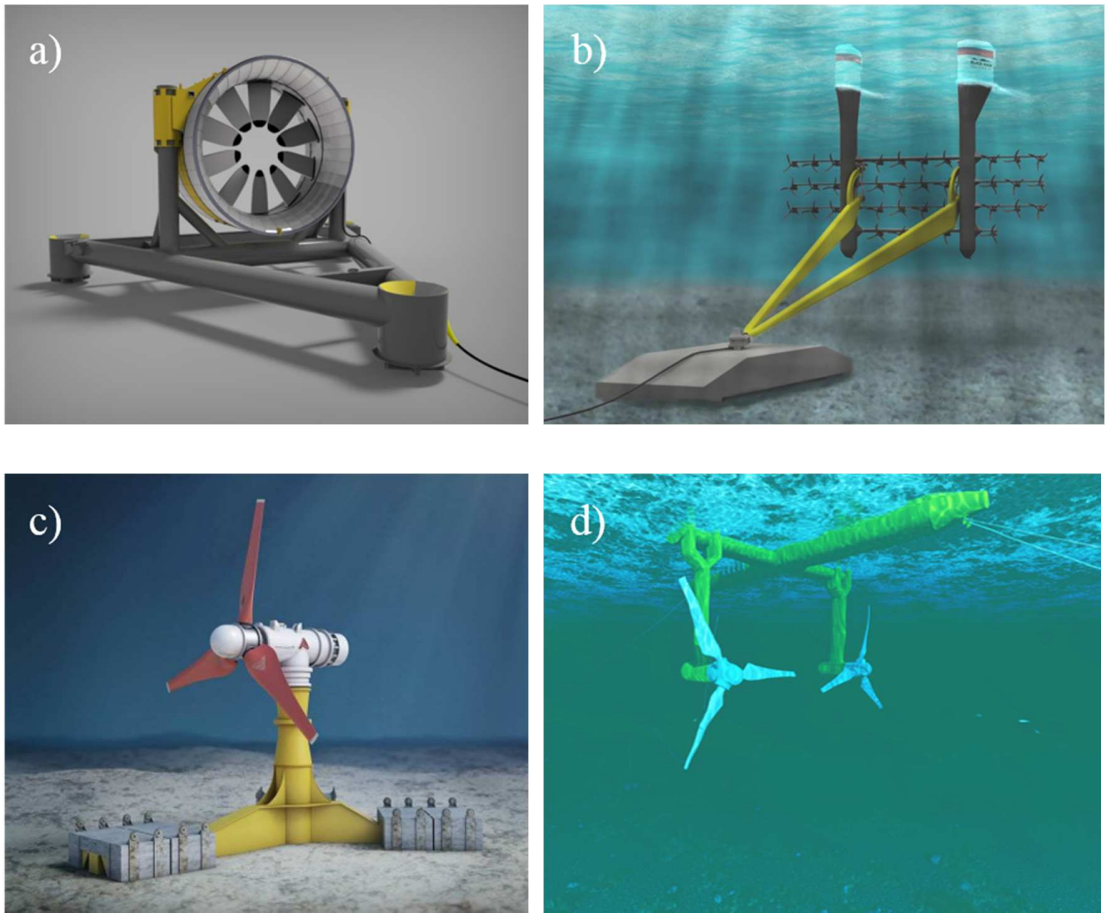

FIGURE 1.2: FOUR BERTH HOLDERS AT FORCE: A) OPENHYDRO, B) BLACK ROCK TIDAL POWER, C) ATLANTIS, D) MINAS ENERGY

Full-scale testing is costly and sometimes not an option for researchers and developers. Pre-deployment testing, a combination of small-scale testing and numerical modelling, is a key step in determining optimum designs and investigating unknown features (*e.g.* wake, turbulence, loading, *etc.*).

In addition to needing improved methods of optimization, there is a pressing need for insight in the wake flow of tidal turbines. Often, sites of large tidal energy are spatially confined in bathymetric channels (estuaries, inlets, between islands) and will require multiple turbine arrays to be financially viable. Wake characteristic parameters, such as velocity deficit and turbulence intensity, are essential to multi-turbine array investigations as they will have direct impact on the performance and loading effects of subsequent lateral and downstream turbines. Vortex shedding is a dynamic phenomenon which would also impact performance, along with durability of such array turbines.

1.2. PROBLEM STATEMENT

Pre-deployment testing of in-stream tidal turbines is key for the development of designs and studying the resulting fluid dynamic effects. Numerical modelling of tidal turbines has become prominent in the growing marine energy industry as it is a cost effective method of addressing both of these issues. Modelling techniques have been borrowed and modified from both the wind industry and ship propeller design, with continuous advancements. Many techniques exist, modelling and experimental, with each exhibiting their own strengths and weaknesses. A better understanding of these methods and their respective applications will help drive innovation and growth of the industry.

Furthermore, an application of this knowledge using an appropriate technique will allow for investigation of turbine performance, wake characteristics, and possible implications of varying flow scenario parameters.

1.2.1. RESEARCH QUESTIONS AND OBJECTIVES

The objectives of this research project are:

1. Develop a numerical modelling methodology, using ANSYS CFX, enabling reliable study of turbulent flow over an in-stream tidal turbine. This includes

analyzing geometric effects on the solution and determining which turbulence model ($k-\varepsilon$, $k-\omega$, SST) is the best suited for this application.

2. Validate the numerical models using experimental results from the University of Southampton (Bahaj *et al.*, 2007a).

3. Characterize the nature of the turbulent flow within the wake generated past the in-stream turbine (length, zone of impact, strength of turbulence).

Objective 1: Develop a numerical modelling methodology

This objective aims to investigate the best techniques for modelling and post-processing the performance and fluid dynamic effects of a tidal turbine. A two-dimensional model will first be created to validate the numerical setup. Near wake turbulence is of interest so it was chosen to explicitly model the turbine and blades. Due to this, much emphasis will be placed on the building of the turbine geometry. The effect of parameters such as trailing edge roundness and twist axis location will be studied. Additionally, the effect of computational mesh density within the wake, downstream domain length, and cross-sectional domain size on the turbine performance and wake evolution will be considered.

Objective 2: Validate the models

It is essential to compare and validate a numerical model to experimental data to give confidence in the numerical results. This will be accomplished by comparing the numerical results to experimental data from the University of Southampton, by way of comparison of power and thrust coefficients at a range of tip speed ratios. The experimental researchers investigated the turbine performance in both a cavitation tunnel and towing tank, at five pitch angles (from 15° to 30°), four yaw angles (from 0° to 30°), and two tip-immersion depths in the towing tank (0.55D and 0.19D). This research project will focus solely on the 0° yaw scenario in the cavitation tunnel, with a pitch angle of 25°, situated mid-plane in the tank.

Objective 3: Characterize the flow

Turbulence intensity, downstream vorticity, velocity and pressure contours, along with other analysis tools will be used to study the zone of impact of the resultant wake of the turbine. This includes wake recovery distances, turbulent intensity within, and near wake eddy shedding. This information will be important for future studies that will aim to determine multiple turbine interaction.

1.3. TIDAL FLOWS

Some properties were mentioned above that differentiate tidal flows from wind flows and are discussed in greater detail here, as well as a definition of the wake. The impact of the tidal flow properties on the performance and wake are discussed. It is important to understand these properties when undergoing investigative research, especially when simplifying assumptions are made.

1.3.1. WAKE DEFINITION

A consequence of mass conservation is that the extraction of energy from a tidal flow, by way of a momentum reduction, forces a flow expansion. It is this expanding, slow moving flow that is defined as the wake. The expansion typically occurs 0 to 1 diameter lengths downstream of the device. Additionally, it is likely that the device will impart some mechanical motions as wake swirl and vortex shedding from the structure, blade roots and blade tips. Vortices shed from the blade tips will generally bound the slow wake flow from the free-stream flow. At some point downstream of the turbine this bounded flow is broken up by ambient turbulence. This wake region is often called the *near wake*, typically lasting 0 to 3/4D (Bahaj *et al.*, 2007b), while *far wake* regions persist much further downstream.

1.3.2. TIDAL FLOW PROPERTIES

Tidal flow properties that must be taken into consideration by tidal investigators are listed here:

1. *Blockage*: Tidal flows will tend to be bound by the water surface, the seabed and bathymetric channels. This effect, called blockage, increases the velocity in zones where the turbine will be placed. Blockage is also seen in experimental setups and

can be described using a blockage ratio, often reported as a percentage. Blockage ratio is defined as the ratio of turbine (A) area to the flow channel area (A_C), as in:

$$B_r = \frac{A}{A_C} \tag{1.1}$$

In some cases, it is desirable to apply a blockage correction to experimental results with the goal of approximating a free-stream flow scenario. Analytical approximations can be applied to achieve this effect. For example, Barnsley and Wellicome (Barnsley & Wellicome, 1990) modified Glauert's propeller specific blockage correction (Glauert, 1947) for application in wind turbine experimentation. This approach is commonly used and has been adopted for tidal flow investigations (Bahaj *et al.*, 2007a). Alternatively, specific to numerical studies, the researcher can extend the computational domain cross-section to reduce the blockage ratio.

2. *Cavitation*: Cavitation, the formation of vapour cavities in a fluid, occurs when the local static pressure (p_0) is reduced to the fluid's vapour pressure (p_v). These pockets implode when subjected to high pressures, often causing severe damage to machinery and creating minor shockwaves. In rotating machinery, *e.g.* tidal turbines, this process can create harsh cyclical loading. It is useful in experimentation to define a cavitation number which allows the researcher to quantify the inception of a cavitation envelope. This number is defined as:

$$\sigma = \frac{p_0 - p_v}{\frac{1}{2}\rho V^2} \tag{1.2}$$

Lee *et al.* numerically investigated cavitation mitigation in a blade design analysis (Lee *et al.*, 2012). By introducing a winglet at the blade tip they observed a slight increase in performance, particularly at low tip speed ratios (TSR). TSR, a numeric that describes the relationship of the tangential blade tip velocity and the inflow velocity, it is calculated using the following relation:

$$TSR = \frac{\omega R}{V_0} \tag{1.3}$$

High incidence angles are a result of low TSRs, and rapid flow separation on the blade leads to severe pressure gradients and cavitation. However, Batten *et al.* completed a numerical analysis wherein the prediction of cavitation was carried out. The researchers found that cavitation could be avoided with an appropriate selection of hydrofoil and device operation (Batten *et al.*, 2008).

3. *Energy Density*: Energy density is useful in assessing the potential of different energy sources. This value is dependent linearly on the kinetic energy of the fluid. The density of seawater, 1027 kg/m^3, is roughly 800 times that of air. It is expected for most in-stream tidal devices to operate in flows of approximately 2.5 m/s, or one third to one sixth of the velocity for a typical wind turbine. Consequently, in-stream tidal devices will experience an energy density roughly fourteen to twenty times greater than wind turbines. This allows for the tidal turbine to be fourteen to twenty times smaller than an equally rated wind turbine, a positive finding as many sites will be limited to a water depth of 30-50 m (Karsten *et al.*, 2008).

4. *Availability and Capacity Factors*: Availability and capacity factors are convenient for evaluating power plants. Availability factor is the ratio of the amount of time of electricity production during a period and the total amount of time in that period. This will be device specific with factors such as cut in speed, load capping, yawing, *etc*. Capacity factor is the ratio of electrical output during a period of time and the total possible production if the plant were to run at full capacity in that period. This value is expected to be high for in-stream tidal devices. Marine Current Turbines, for example, reported a 66% capacity factor for their SeaGen prototype in Northern Ireland's Strangford Lough ("Marine Current Turbines to deploy tidal farm off Orkney after securing Site Lease from the Crown Estate,"). For contrast, the Burton Wold Wind Farm of 20 MW capacity, consisting of ten Enercon E70-E4 wind turbines, reported a 20% capacity factor in 2014 ("Burton Wold Windfarm - A Output,").

5. *Predictability*: A key attribute to tidal power is its predictability and consistency. A lunar day lasts 24 hours and 50 minutes. This means that there is 6 hours and 12.5 minutes between tidal peaks. Figure 1.3 provides a simplified example of tidal height and current speed in a 24 hour period. Note the shift between these two such that the peaks in tide height (slack tide) correspond with zero current.

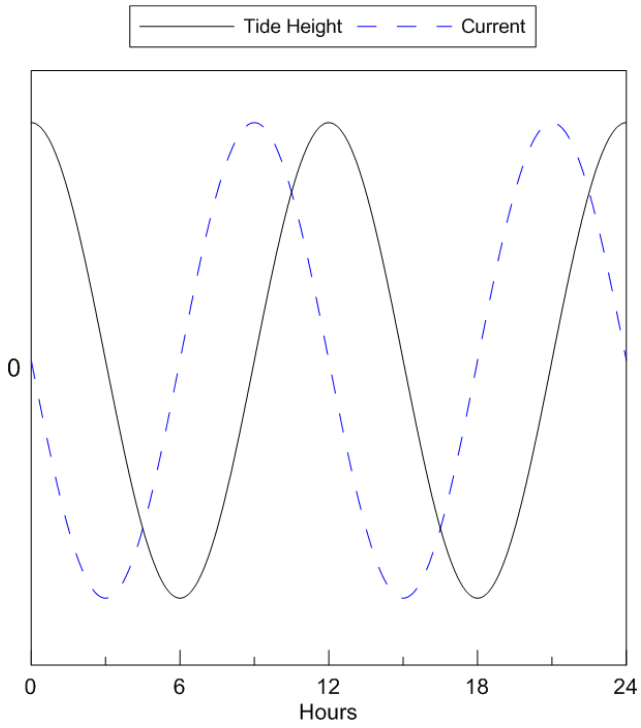

FIGURE 1.3: TIDAL HEIGHT AND CURRENT SPEED

6. *Ambient and Structure Induced Turbulence*: Flow turbulence in a marine setting can be generated from a range of sources at varying length scales. Seabed makeup and bathymetric interference are of concern for seabed mounted turbines, while waves and storm effects will impact the performance and loading of turbines higher in the water column (Evans *et al.*, 2013). As mentioned earlier, eddies will be shed from the device as well. The scale and intensity of the turbulence will depend on device and support structure used, but in general eddy shedding will take place from the structure, blade root and blade tip. These turbulent pockets may negatively impact downstream array turbines but will also act in re-energising the wake by breaking up the slow moving wake flow.

Reynolds number, a non-dimensional ratio of inertial and viscous forces, can be used as a measure of turbulence, and turbulent length scales, within a flow. This is an important parameter for experimental scaling, *i.e.* many researchers will ensure flow properties or characteristic lengths in an experimental setup to match the Reynolds number of a typical full scale design.

$$\mathrm{Re} = \frac{VL}{\nu} \tag{1.4}$$

7. *Free Surface Effects*: It is important to consider the Froude number, comparing inertial forces to external forces (commonly due to gravity), as the presence of the free surface allows for a change in water depth. As water flows over the turbine, and energy is extracted, it experiences a water channel depth drop. This drop is potentially inconsequential for an individual turbine but the effect may be compounded in multi-turbine arrays. The change in depth will increase velocity and blockage downstream of the turbine. Also, the Froude number is another parameter to be considered when scaling for experimental studies.

$$\mathrm{Fr} = \frac{V}{\sqrt{gd}} \tag{1.5}$$

Unfortunately, Froude and Reynolds numbers cannot be linearly scaled together while designing an experimental model. When scaling down a full scale prototype to a typical experimental tank the Froude number can be large due to a small tank depth. The velocities required to achieve Froude number matching can be high and unrealistic for a test setup. For this reason, as in the case of the validation study for this report, Reynolds scaling is often the choice scaling method.

1.4. EXPERIMENTAL TECHNIQUES

Tidal turbine developers and academic researchers are able to take advantage of small scale testing for relatively low cost proof-of-concept and fluid phenomena investigations. Typically, for instream tidal devices, these studies are carried out in towing tanks, flume tanks or cavitation tunnels. For example, Doman *et al*. recently carried out performance tests on a 1/20th scale rotor in the towing tank at Strathclyde University (Doman *et al.*,

2015). The team emphasised the quantification of uncertainty in the calibration and measurement equipment. The intention of the uncertainty assessment was to give increased confidence in the data set for future validation of numerical models. Currently, the research team is developing a BEMT-based development tool for blade design that will use this data set for comparison.

Likewise, Bahaj *et al*. completed performance analyses on a scale turbine in both a towing tank and a cavitation tunnel (Bahaj *et al.*, 2007a). It is this cavitation tunnel data set that will be used later in this thesis for model validation. A variety of tests were completed wherein in rotor velocity, fluid velocity, yaw angle, tip immersion and twin rotor interference were studied. Turbine performance was presented in terms of power and thrust coefficients over a range of tip speed ratios. As expected, a significant reduction in performance was observed when the turbine was yawed away from the flow direction. A reduction in power was also observed with a reduced tip immersion. This result carries the implication that, as mentioned in Section 1.3.2, the turbine depth should be a consideration for small and full scale instream tidal designs. The researchers found that the addition of a lateral twin rotor had minimal impact on the turbine performance, a result with positive implications towards turbine arrays. Finally, it was shown that cavitation can be avoided with careful turbine design.

A lesser amount of experimental data sets are available which focus on wake measurement and characterization. One method of experimental wake analysis is to simulate the turbine with a porous disk. Bahaj *et al*. employed this method in a flume tank at the University of Southampton (Bahaj *et al.*, 2007b). The intention of this experiment was to study the governing parameters affecting the wake structure and dissipation. It was observed that the free surface and tank floor bounded the wake, impeding expansion. Velocity deficit along the centreline and vertical profile were also examined, showing a wake persisting beyond 20 diameter lengths downstream. This data set was later used to tailor an eddy-viscosity actuator disk numerical model (Harrison *et al.*, 2009).

More recently, Mycek *et al*. studied the impact of a two rotor system on both turbine performance and wake evolution. Tests were completed in the towing tank at IFREMER

in France that varied the axial (streamwise) distance between turbines as well as employed two upstream turbulence intensities (I = 3% and 15%) (Mycek *et al.*, 2013; Mycek *et al.*, 2014a, 2014b). It was shown that the latter had a greater effect on turbine performance as higher ambient turbulence intensities will accelerate the attenuation of wake effects. For example with I = 15%, a global turbine efficiency of 90% was reached with a 6D inter-turbine distance while, with I = 3%, a global efficiency of 50% was reached with a 12D spacing.

Often the experimental data set is used to validate a numerical model. Computational testing grants superior flexibility to the researcher as it tends to be faster, cheaper and allows for detailed analysis into physical phenomena. The following section provides greater detail into this approach as it is the focus of the presented work herein.

1.5. NUMERICAL TECHNIQUES

Unlike the wind industry where the three bladed turbine has become ubiquitous, perceptions on optimal marine energy designs vary greatly. However, the proven feasibility of each can be costly. Numerical computation can help reduce start-up costs and streamline optimization. It can also be used to analyse hydrodynamic characteristics; whether they be wake flow, turbulent structure visualization or bathymetric influences. A literature review was performed to determine the most common numerical approaches for studying wind and tidal turbine flows. It was found that two approaches are primarily used for turbine analysis: blade element momentum theory (BEMT) and computational fluid dynamics (CFD).

1.5.1. BEMT

BEMT, initially conceptualized by Rankine (Rankine, 1865), W. Froude (Froude, 1878) and R. E. Froude (Froude, 1889), and developed by Glauert (Glauert, 1935), consists of dividing the turbine blade into a number of isolated two-dimensional elements. Thrust and power coefficients are derived by determining the lift and drag coefficients of each element from hydrodynamic theory and integrating them across the blade length. This technique has been useful in the helicopter and wind energy industries (Johnson, 1980; Sørensen & Kock, 1995). More recently BEMT has been applied to in-stream tidal investigations and

has been useful in turbine design (Batten *et al.*, 2008; Clarke *et al.*, 2006). Batten *et al.* applied BEMT to a horizontal axis tidal turbine (HATT) design and showed good agreement with experimental results (Batten *et al.*, 2008). This study partially focussed on the inception of cavitation for the experimental scenario of shallow tip immersion. It was found that cavitation could be avoided with the use of suitable designs and choice of two-dimensional sections. Drawbacks of the BEMT approach include a lack of wake expansion and unresolved tip and root losses. In addition, Lee *et al*. completed a BEMT model of a three bladed HATT and found that power was under-estimated at low tip speed ratios (Lee *et al.*, 2012). It was suggested that the under-estimation was due to a phenomena called stall delay. In BEMT it is assumed that there is zero spanwise fluid flow (along the blade). In reality, centrifugal forces on the rotating turbine causes unstable cross-flow along the blade, resulting in stationary and travelling cross-flow vortices. These instabilities cause separation delays, lift increase and drag reduction.

Mathematical corrections can be applied to garner improved correlation with other methods. For example, Masters *et al*. included Prandtl corrections for hub and tip losses (Masters *et al.*, 2011). Through validation with Garrad Hassan's Tidal Bladed Software (GH Tidal Bladed) they showed an improved correlation in power and thrust coefficients, particularly in the regions outside of optimum flow. Still, limitations exist which render the method ineffective for some tidal investigations. Particular to turbine wake analysis for array investigations BEMT is insufficient and another modelling tool must be employed.

1.5.2. BEMT-CFD COUPLING

Due to an increase in computational resources, CFD has become more prevalent recently for tidal related investigations. This approach involves discretizing the fluid domain and solving the Navier-Stokes equations for the resultant finite volumes. CFD is more robust than BEMT in that it can provide greater detail in the far wake region and, depending on the technique used, in the near wake. Several combinations of BEMT-CFD coupling have been developed to reduce the shortcomings of the BEMT model. This approach has been successful for ship propellers (Phillips *et al.*, 2009) as well as in-stream tidal turbines (Malki *et al.*, 2012; Malki *et al.*, 2013; Masters *et al.*, 2012; Masters *et al.*, 2013; Turnock *et al.*, 2011). In this case BEMT is implemented to characterize turbine source terms,

which are then applied to a CFD model to approximate the interaction between the turbine blades and the incoming fluid. Malki *et al*. used this approach to investigate non-uniform flow by imposing a negative gradient to the top surface of the model domain corresponding to the water surface (Malki *et al.*, 2012). This technique was compared to two experimental data sets with good agreement; It paired well to a towing tank setting with the output power coefficient (Bahaj *et al.*, 2007a) and velocity deficit from flume tank data for porous disks which had detailed wake data (Myers & Bahaj, 2010).

1.5.3. CFX – ACTUATOR THEORY

An alternative CFD approach, the actuator disk method has been shown to be valuable for modelling the far wake of a turbine but provides little insight in the near turbine regions (Harrison *et al.*, 2009). This method substitutes the turbine with a porous disk using an imposed momentum source. It is beneficial as it eliminates some scaling issues and can greatly reduce mesh density in the rotor region. Recently, advancements have been made in this technique, including the actuator line method. Instead of distributing the forces over the disk face, this method contains rotating source areas which represent the blades. Keck applied this to a simplified horizontal axis wind turbine (HAWT) design and observed good agreement of wind conditions with both BEMT and field measurements (Keck, 2012). Alternatively, Shives and Crawford have applied alterations to the SST turbulence model within an actuator disk model (Shives & Crawford, 2014). The two key implemented changes were limits on eddy-viscosity near the turbine rotor and induced turbulent kinetic energy sources in the near wake. Thus far the augmentation has improved agreement in velocity and turbulent intensity amidst the turbulent wake.

1.5.4. CFD – FULLY RESOLVED GEOMETRY

Fully resolving the turbine structure and blades in a CFD analysis provides the most detail when considering local and near wake turbulent structures. As a result, this approach has become popular for analyzing tidal turbines in recent years (Afgan *et al.*, 2013; Arnold *et al.*, 2013; Bai *et al.*, 2013; Faudot *et al.*, 2013; Gretton *et al.*, 2009; Jo *et al.*, 2012; Kang *et al.*, 2012; Khalid *et al.*, 2013; Lawson *et al.*, 2011; Lee *et al.*, 2012; Lloyd *et al.*, 2013; Marsh *et al.*, 2012; Mason-Jones *et al.*, 2012; McNaughton *et al.*, 2012; McSherry *et al.*, 2011; O'Doherty *et al.*, 2009; Sheng *et al.*, 2013; Yang & Lawn, 2011). This approach also

allows for direct comparison, and scaling if necessary, with experimental results (McSherry *et al.*, 2011). Afgan *et al.* were successful in creating and validating a CFD model for a three bladed HATT (Afgan *et al.*, 2013). The $k-\omega$ based SST and LRR turbulence models were used for validation and methodology testing, at which point large-eddy simulations (LES) were performed. Jo *et al.* similarly created a model of a three bladed HATT for analysis of wake flow characteristics (Jo *et al.*, 2014) to ultimately study turbine interactions. A main tool used for wake analysis was velocity deficit, a normalized view at downstream and upstream velocity difference at multiple slices in the wake. This study was a follow up of an investigation which utilized the explicitly resolved blades, analyzing vibration characteristics of the turbine using three-dimensional unsteady simulations (Jo *et al.*, 2013).

CFD offers the ability to quickly analyse and optimize turbine designs as well as gain a deeper insight into flow characteristics that cannot be captured with BEMT. In addition to the BEMT-CFD model discussed above, Lee *et al.* modelled a three bladed HATT using the ANSYS Fluent package (Lee *et al.*, 2012). The researchers focussed on three blade types: The first, called baseline, was a lofted three-dimensional airfoil with an abrupt tip; the second incorporated a rounded tip edge to reduce tip vortex creation; the third had a raked tip, often called a winglet in aeronautics. The raked tip design showed improved performance, particularly at low TSRs, as tip vortex creation at high incidence angles was mitigated. Lawson and Li, from the National Renewable Energy Laboratory (NREL), completed a design model of a two bladed HATT (Lawson *et al.*, 2011). Initially, blade design was completed using BEMT in conjunction with a genetic optimization algorithm where XFOIL was used to predict the NACA airfoil's lift, drag and pressure coefficients. The blade design was then transferred to a three-dimensional CFD study using STAR-CCM+. Steady state simulations were run for a grid resolution study followed by transient simulations to determine the effect of time-dependent flow phenomena. It was found that the effect of the computational timestep was minimal and the results from the steady state and transient simulations were in good agreement. They suggest however that transient simulations would be necessary in flow scenarios where a high level of separation is observed.

1.5.5. TURBULENCE MODELLING

Current research is being done to determine the most appropriate turbulence model to use in a tidal turbine CFD simulation. The reason for, and application of, turbulence models is discussed in detail in later chapters. The most commonly used turbulence models today are the $k-\varepsilon$ and $k-\omega$ eddy-viscosity models, Shear Stress Transport (SST), the Launder-Reece-Rodi (LRR) Reynolds stress model and the Large Eddy Simulation (LES) model. SST, found to have the most repeated use in current literature, is a two equation eddy viscosity model that employs $k-\omega$ in the inner boundary layer and transitions to $k-\varepsilon$ further in the free stream. Each model alone have their limitations, *e.g.* $k-\varepsilon$ tends to underpredict force components (McNaughton *et al.*, 2012) while $k-\omega$ is sensitive in free-shear flows. The $k-\varepsilon$ turbulence model is acceptable for initial use to reduce computational cost (Masters *et al.*, 2013) but is insufficient by itself for detailed turbine simulation. Yang and Lawn were the only researchers found in recent years to exclusively utilize the $k-\omega$ turbulence model (Yang & Lawn, 2011). This particular investigation was a two-dimensional, quasi-steady state, CFD analysis of a vertical axis tidal turbine (VATT) with flapping blades that are hinged on a revolving drum. The focus of the study was the performance of the turbine, however, and wake flow physics were not reported. It is unclear as to the turbulence model impact on their turbulent mixing results.

The SST model by Menter (Menter, 1994) utilizes $k-\omega$ in the inner boundary regions and $k-\varepsilon$ in the free-stream regions. This model is capable of acceptably resolving turbulence (McSherry *et al.*, 2011), as is LRR (McNaughton *et al.*, 2012). A shortcoming of this level of turbulence modelling is an underprediction of the power coefficient. To achieve a higher resolution of the turbulence in the near and far regions, while requiring less computational effort than a Direct Numerical Simulation (DNS), an LES model can be used. LES has been proven as a viable option for tidal turbine turbulence simulations (Afgan *et al.*, 2013). This approach has significant computational effort however, and few studies could be found that employ it for this application. Most recent investigations tend to suffice with using SST.

1.6. THESIS ORGANIZATION

This thesis is organized into seven chapters, Chapter 1 of which previously presented the relevant background and research objectives.

Chapter 2 presents the theory behind the approach taken, including a general overview of the governing Navier-Stokes and continuity equations, Reynolds Averaged Navier-Stokes (RANS) based modelling, turbulence modelling and near wall treatment in fluid numerical models.

Chapter 3 presents the model development. The geometry construction approach is discussed, as well as the impact of geometry variations such as twist axis location and trailing edge roundness. Fluid parameters such as boundary conditions are then described. Turbulence models used in the investigation are introduced as well as methods of creating a suitable computational mesh are discussed. Finally, the methodologies for convergence and sensitivity studies to be carried out are outlined.

Chapter 4 provides and discusses the results from convergence and sensitivity studies. These studies included the impact of the computational mesh density in the wake, domain downstream length, and domain cross-sectional size on the turbine performance and wake evolution.

Chapter 5 presents the results for both the two-dimensional and three-dimensional cases. These are compared to numerical and experimental results, respectively, for validation.

Chapter 6 briefly compares three popular turbulence models and finally the wake physics are analysed using contour plots of velocity and pressure, iso-surfaces of vorticity and velocity deficit.

Chapter 7 summarizes the work completed, presenting the conclusions and recommendations for future work.

CHAPTER 2 THEORY

The following chapter outlines the principal theories and methods employed in this project. The reader is encouraged to review the CFX-Solver Theory Guide for greater detail (ANSYS, 2013).

2.1. CFD FUNDAMENTALS

The fundamental objective for CFD analyses is to determine the velocity and pressure fields in a flowing fluid by solving the Navier-Stokes equations. In doing so, CFX employs a fully implicit finite volume approach to obtain the solution set. The software uses a coupled solver to solve the hydrodynamic equations of pressure and velocity as a single system. A co-located grid layout is employed such that the control volumes are identical for all transport equations. A modified Rhie-Chow interpolation scheme, proposed by Rhie and Chow (Rhie & Chow, 1982) and modified by Majumdar (Majumdar, 1988), is employed to avoid decoupling as a result of using a non-staggered grid. A high resolution advection scheme was employed in all simulations. This method is a blend between a 2nd order accurate central difference scheme and a 1st order accurate upwind scheme. The blend factor, β, is computed throughout the simulation to be as close to 1 as possible, favouring the central difference scheme.

The Reynolds Averaged Navier-Stokes equations were used for all simulations presented in this thesis. Two simplifying approaches are taken to modify the Navier-Stokes equations: describing the turbulent velocity field as a superposition of the time-averaged velocity $\bar{u}$ and fluctuating velocity component u' and time-averaging the individual components of the Navier-Stokes equations. The first process is not specific to the RANS approach but will be considered henceforth, and is described as:

$$u(x, y, z, t) = \bar{u}(x, y, z) + u'(x, y, z, t) \tag{2.1}$$

A simple, time dependent, example of this can be visualized in Fig. 2.1. Here, the solid blue line indicates the actual, turbulent velocity, and the black dashed line indicates the

average velocity. For simplicity this figure demonstrates a steady state solution of the averaged velocity component, i.e. $\bar{u}$ is not time dependent.

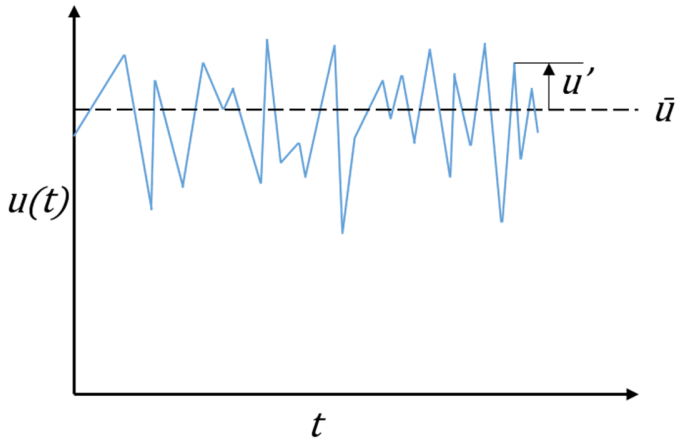

FIGURE 2.1: TURBULENT VELOCITY DECOUPLING

The effect of this turbulent velocity decoupling is demonstrated below, where the incompressible momentum equation in the *x*-direction is:

$$\rho\left[\frac{\partial u}{\partial t}+\frac{\partial}{\partial x}(u^2)+\frac{\partial}{\partial y}(uv)+\frac{\partial}{\partial z}(uw)\right] = -\frac{\partial P}{\partial x}+\mu\left[\frac{\partial^2 u}{\partial x^2}+\frac{\partial^2 u}{\partial y^2}+\frac{\partial^2 u}{\partial z^2}\right] \tag{2.2}$$

For brevity, only the first two components in the left-hand brackets will be examined here.

$$\frac{\partial u}{\partial t}=\frac{\partial \bar{u}}{\partial t}+\frac{\partial u'}{\partial t}=\frac{\partial u'}{\partial t} \tag{2.3}$$

Note that, for a steady state case, the average velocity component $\bar{u}$ has a zero time derivative and drops out. Secondly,

$$\frac{\partial}{\partial x}(u^2)=\frac{\partial}{\partial x}[(\bar{u}+u')]^2=\frac{\partial}{\partial x}(\bar{u}^2+2\bar{u}u'+u'^2) \tag{2.4}$$

The time averaging used in RANS stipulates that the time average of u' be 0. Carrying this through for all components of Eq. (2.2) provides the steady state RANS momentum equation, again cited in one dimension for conciseness:

$$\rho\left[\frac{\partial}{\partial x}(\bar{u}^2)+\frac{\partial}{\partial y}(\bar{u}\bar{v})+\frac{\partial}{\partial z}(\bar{u}\bar{w})\right]$$
$$=-\frac{\partial \bar{P}}{\partial x}$$
$$+\left[\frac{\partial}{\partial x}\left(\mu\frac{\partial \bar{u}}{\partial x}-\rho\overline{u'^2}\right)+\frac{\partial}{\partial y}\left(\mu\frac{\partial \bar{u}}{\partial y}-\rho\overline{u'v'}\right)\right.$$
$$\left.+\frac{\partial}{\partial z}\left(\mu\frac{\partial \bar{u}}{\partial z}-\rho\overline{u'w'}\right)\right] \tag{2.5}$$

The same approach is taken for the incompressible mass conservation (continuity) equation:

$$\frac{\partial u}{\partial x}+\frac{\partial v}{\partial y}+\frac{\partial w}{\partial z}=0$$

$$\frac{\partial(\bar{u}+u')}{\partial x}+\frac{\partial(\bar{v}+v')}{\partial y}+\frac{\partial(\bar{z}+z')}{\partial z}=0 \tag{2.6}$$

$$\frac{\partial \bar{u}}{\partial x}+\frac{\partial \bar{v}}{\partial y}+\frac{\partial \bar{z}}{\partial z}=0$$

At this point, there are seven unknown variables: pressure (P), three time-averaged velocity components ($\bar{u}$, $\bar{v}$, $\bar{w}$) and three fluctuating velocity components (u', v', w'). The three momentum and one continuity Navier-Stokes equations are insufficient. However, the turbulent velocity decoupling and time-averaging introduced three new stresses, hereafter called Reynolds stresses:

$$\rho\overline{u'^2}=\mu_t\frac{\partial \bar{u}}{\partial x}=\tau'_{xx}$$

$$\rho\overline{u'v'}=\mu_t\frac{\partial \bar{u}}{\partial y}=\tau'_{xy} \tag{2.7}$$

$$\rho\overline{u'w'}=\mu_t\frac{\partial \bar{u}}{\partial z}=\tau'_{xz}$$

where μ_t is the turbulent viscosity. This states that the Reynolds stresses are proportional to the mean velocity gradients and eddy (turbulent) viscosity. This defines an eddy viscosity model. An effective viscosity is then defined as:

$$\mu_{eff} = \mu + \mu_t \tag{2.8}$$

This approach provides the opportunity to close the RANS equations with turbulence (closure) models that solve for the effective viscosity.

2.2. TURBULENCE MODELLING

This section will focus on the three eddy viscosity models which will be employed in this study. The models herein are two equation models that use separate transport equations to indirectly solve for the turbulent velocity and turbulent length scale; the turbulent viscosity is then determined as a product of these two variables. In two-equation models, the turbulence velocity scale is computed from the turbulent kinetic energy, while the turbulent length scale is estimated from two properties of the turbulence field. The turbulence models discussed hereafter are based on empirical coefficients, further details of which can be found in the product documentation (ANSYS, 2013).

2.2.1. THE $k-\varepsilon$ MODEL

k is the turbulence kinetic energy, defined as the variance of the fluctuations in velocity, while ε is the turbulence eddy dissipation. These can be directly solved for from the following transport equations:

$$\rho\frac{\partial k}{\partial t} + \rho\frac{\partial}{\partial x}(\bar{u}k) = \frac{\partial}{\partial x}\left[\left(\mu + \frac{\mu_t}{\sigma_k}\right)\frac{\partial k}{\partial x}\right] + P_k - \rho\varepsilon + P_{kb} \tag{2.9}$$

$$\rho\frac{\partial \varepsilon}{\partial t} + \rho\frac{\partial}{\partial x}(\bar{u}\varepsilon) = \frac{\partial}{\partial x}\left[\left(\mu + \frac{\mu_t}{\sigma_\varepsilon}\right)\frac{\partial \varepsilon}{\partial x}\right] + (C_{\varepsilon 1}P_k - C_{\varepsilon 2}\rho\varepsilon + C_{\varepsilon 1}P_{\varepsilon b}) \tag{2.10}$$

where $C_{\varepsilon 1}$, $C_{\varepsilon 2}$, σ_k and σ_ε are constants of the model with values of 1.44, 1.92, 1.0 and 1.3, respectively. P_{kb} and $P_{\varepsilon b}$ represent the influence of buoyancy forces and P_k is the

turbulence production due to viscous forces. Both P_{kb} and $P_{\varepsilon b}$ will have values of 0 as this buoyancy was neglected in this work.

The turbulent viscosity is then determined by:

$$\mu_t = C_\mu \rho \frac{k^2}{\varepsilon} \tag{2.11}$$

where C_μ is a constant with the value 0.09.

2.2.2. THE WILCOX $k-\omega$ MODEL

The $k-\omega$ model developed by Wilcox (Wilcox, 1986) solves for *k*, the turbulent kinetic energy, and ω, the turbulent frequency using the following relationships:

$$\rho \frac{\partial k}{\partial t} + \rho \frac{\partial}{\partial x}(\bar{u}k) = \frac{\partial}{\partial x}\left[\left(\mu + \frac{\mu_t}{\sigma_k}\right)\frac{\partial k}{\partial x}\right] + P_k - \beta' \rho k \omega + P_{kb} \tag{2.12}$$

$$\rho \frac{\partial \omega}{\partial t} + \rho \frac{\partial}{\partial x}(\bar{u}\omega) = \frac{\partial}{\partial x}\left[\left(\mu + \frac{\mu_t}{\sigma_\omega}\right)\frac{\partial \omega}{\partial x}\right] + \alpha \frac{\omega}{k} P_k - \beta \rho \omega^2 + P_{\omega b} \tag{2.13}$$

where β', α, β, σ_k and σ_ω are model constants of values 0.09, 5/9, 0.075, 2 and 2, respectively.

The turbulent viscosity is then determined by:

$$\mu_t = \rho \frac{k}{\omega} \tag{2.14}$$

2.2.3. THE SHEAR STRESS TRANSPORT (SST) MODEL

The SST model was developed to take advantage of the benefits of the previous models while doing away with their deficiencies. Specifically, $k-\varepsilon$ is superior in free shear flows while $k-\omega$ is better suited to resolving the viscous sublayer, introduced in Section 2.3. SST is preferable to other blending models as it applies a limiter on the formulation of eddy viscosity to account for transport of the turbulent shear stress in the boundary layer. This approach properly predicts the onset of flow separation from smooth surfaces. This limiter is described as:

$$\nu_t = \frac{a_1 k}{max(a_1\omega, SF_2)} \tag{2.15}$$

where S is an invariant measure of the strain rate. F_2, and soon defined F_1, are blending functions, defined by the following:

$$F_1 = tanh(arg_1{}^4) \tag{2.16}$$

$$arg_1 = min\left(max\left(\frac{\sqrt{k}}{\beta'\omega y}, \frac{500\nu}{y^2\omega}\right), \frac{4\rho k}{CD_{k\omega}\sigma_{\omega 2}y^2}\right) \tag{2.17}$$

$$CD_{k\omega} = max\left(2\rho\frac{1}{\sigma_{\omega 2}\omega}\frac{\partial k}{\partial x}\frac{\partial \omega}{\partial x}, 1.0x10^{-10}\right) \tag{2.18}$$

and

$$F_2 = tanh(arg_2{}^2) \tag{2.19}$$

$$arg_2 = max\left(\frac{2\sqrt{k}}{\beta'\omega y}, \frac{500\nu}{y^2\omega}\right) \tag{2.20}$$

The coefficients of the SST model are determined by blending a linear combination of the $k-\varepsilon$ and $k-\omega$ models following the relation:

$$\phi_3 = F_1\phi_1 + (1 - F_1)\phi_2$$

where ϕ_3 represents coefficients of the SST model, ϕ_1 represents coefficients of the $k-\omega$ model and ϕ_2 represents coefficients of the $k-\varepsilon$ model.

2.3. NEAR WALL TREATMENT

No-slip wall conditions require special consideration as they result in strong gradients in the dependent variables. The resultant boundary layer can be described in two divisions. The innermost layer, called the viscous sublayer, is mostly laminar and momentum and heat transfer are dominated by the local viscosity. Further into the flow is the logarithmic layer where turbulence dominates the mixing processes. Figure 2.2 shows a visual representation of these divisions.

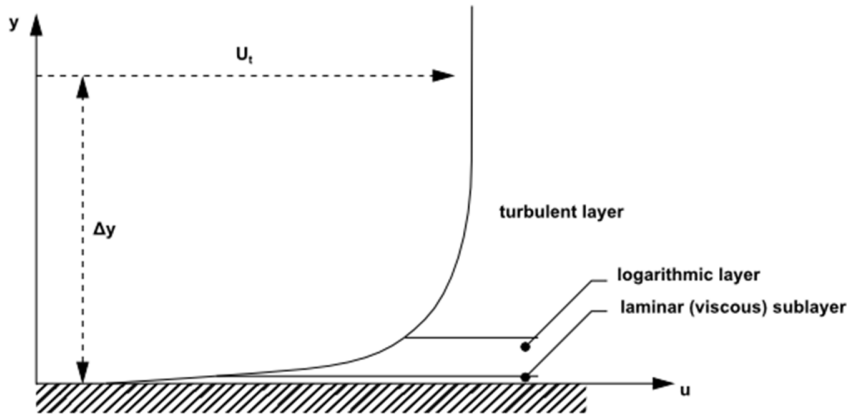

FIGURE 2.2: NEAR WALL (ANSYS, 2013)

Two common approaches to model the flow in the near-wall region are the wall function method and the Low-Reynolds-Number method. Wall functions apply empirical coefficients to the near wall flow to create a logarithmic estimate of the boundary layer. This approach benefits from requiring minimal mesh resolution at the wall but is insufficient for predicting laminar to turbulent transition, as well as detailed investigations. The Low-Reynolds-Number method however fully resolves the boundary layer flow. This approach is more computationally intensive as it requires a high refinement of the mesh at the boundary. Very small mesh length scales in the direction normal to the wall are necessary; this mesh region is called an inflation layer.

A convenient parameter that helps define the near wall method, and determine the adequacy of the inflation layer, is the dimensionless wall distance y^+, colloquially called "y plus", which is defined as:

$$y^+ = \frac{\Delta y_P}{\nu}\sqrt{\frac{\tau_w}{\rho}} \tag{2.21}$$

Standard boundary layer theory can be used to estimate the wall shear stress and boundary layer thickness. The first node distance can then be derived by incorporating the desired number of inflation elements and the applied growth rate. The value for y^+ can then be post-processed in ANSYS CFD-Post, at which point meshing adjustments can be made if necessary. Further detail is provided in Section 3.3.4 regarding the near wall meshing approach.

2.4. PERFORMANCE METRICS

Various metrics will be used throughout this study as convergence criteria, for model validation and for post-processing purposes. Thrust and power coefficients will be used as convergence criteria as well as for model validation. The power coefficient is a measure of the power produced compared to the theoretical power in the approaching fluid. The thrust coefficient is not so directly related to efficiency, but considers how the energy extraction process affects the fluid flow (wake expansion). This metric can also be a tool for examination of axial loading on the device. These coefficients are expressed in the following ways:

$$C_T = \frac{T}{\frac{1}{2}\rho A {V_0}^2} \tag{2.22}$$

$$C_P = \frac{P}{\frac{1}{2}\rho A {V_0}^3} = \frac{\omega Q}{\frac{1}{2}\rho A {V_0}^3} \tag{2.23}$$

Velocity deficit and turbulence intensity will also be considered as convergence criteria. Velocity deficit is a normalized comparison of upstream and downstream velocity while turbulence intensity is a measure of the turbulent velocity fluctuations to the mean flow. These metrics are also of consideration for the sensitivity studies described in Section 3.4. These values provide insight into the occurring wake physics, and are described as:

$$V_{deficit} = 1 - \frac{V_w}{V_0} \tag{2.24}$$

$$I = \frac{u'}{\bar{u}} = \frac{100}{V_0}\sqrt{\frac{2}{3}k} \tag{2.25}$$

Finally, vorticity will also be considered for wake analysis. This is defined as the curl of the velocity field, a measure of rotation in the fluid, as shown in:

$$\vec{\omega} = \nabla \times \vec{V} \tag{2.26}$$

CHAPTER 3 MODEL DEVELOPMENT

ANSYS CFX, a commercially available general purpose CFD code with RANS modelling capabilities, was chosen as a software platform as it has been proven to be applicable to similar scenarios. The development of the models is outlined in the following sections.

Figure 3.1 illustrates the definition of angle of attack (α), pitch angle (β), and incidence angle (Φ). These angles are functions of the chord plane, rotation plane, and direction of relative (apparent) velocity. The apparent velocity (V_A) is the vector subtraction of the true fluid velocity (V_T) and the blade velocity (V_B). A consequence of a rotating blade is that the angle of attack decreases near the tip due to an increased tangential velocity. For this reason, it is typical to incorporate a twist throughout the blade to maintain an optimal angle of attack. The subject of twist angle will be further discussed in Section 3.2. Additionally, Fig. 3.2 outlines the lift and drag forces experienced as a result of a flow induced pressure differential. These forces are used in calculating lift and drag coefficients.

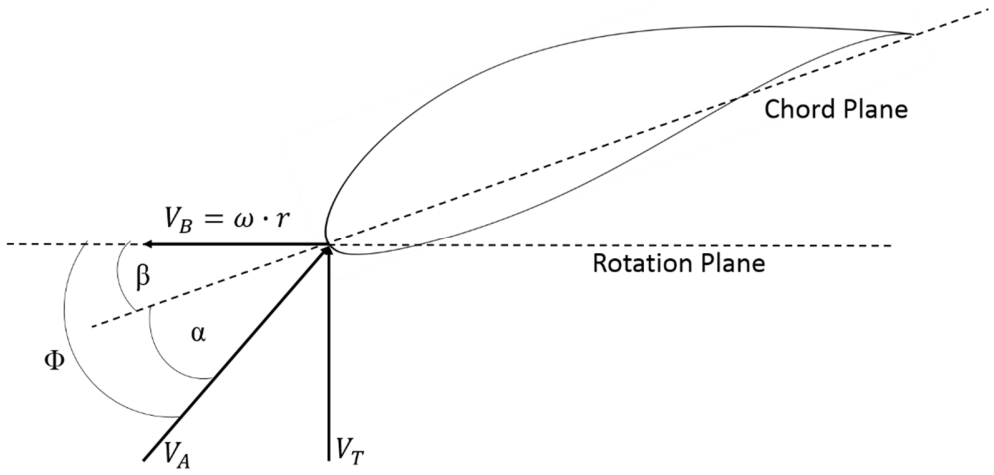

FIGURE 3.1: ANGLE DEFINITION

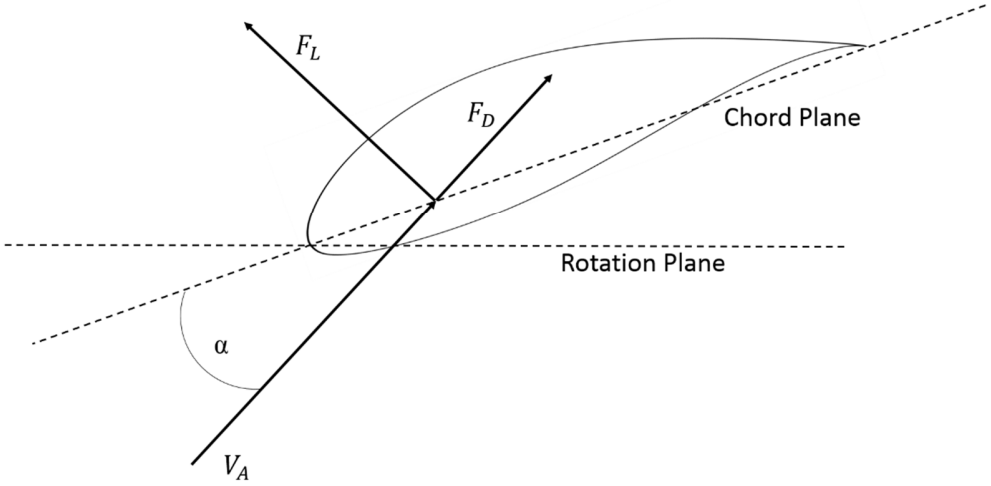

FIGURE 3.2: LIFT AND DRAG FORCES

3.1. TWO-DIMENSIONAL GEOMETRY

A two-dimensional model was created to better understand and validate the fluid physics applied in CFX. A four digit profile, NACA 1408, was chosen to compare to XFOIL, a theoretical airfoil design and analysis program created at MIT. A range of angles of attack were investigated (-7.5° to 15°). Lift and drag coefficients were used for this analysis and are defined as:

$$C_L = \frac{F_L}{\frac{1}{2}\rho A {V_0}^2} \tag{3.1}$$

$$C_{\boldsymbol{D}} = \frac{F_{\boldsymbol{D}}}{\frac{1}{2}\rho A {V_0}^2} \tag{3.2}$$

ANSYS Geometry, Mesher and CFD-Pre were used to set up the two-dimensional test case using the ANSYS workbench functionality. As CFX does not support two-dimensional models, this fluid domain in fact has a thickness of 1 mm. It was attempted to keep a one cell thickness throughout the domain during the meshing process. Symmetry walls were placed on the front and back faces to simulate an infinitely long blade, effectively removing any three-dimensional effects. A chord length of 1 m was chosen, the fluid is water, and all simulations were defined such that Re = 500,000. Figure 3.3 provides a visual of the domain size, a case with 5° angle of attack.

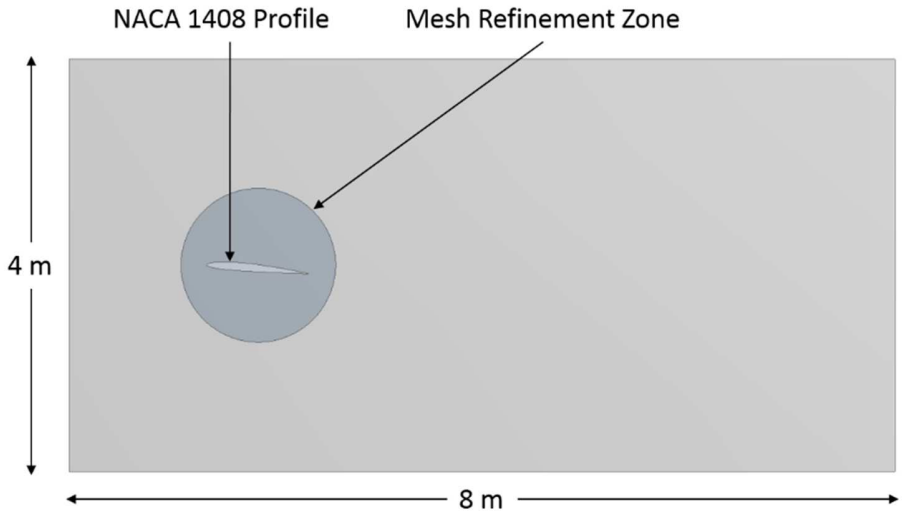

FIGURE 3.3: TWO-DIMENSIONAL DOMAIN

All two-dimensional models, results of which are presented in Section 5.1, incorporated a mesh of ≈ 370,000 cells and a $y^+ \approx 1$. Figure 3.4 demonstrates a typical mesh used while Fig. 3.5 provides a detailed view of the mesh refinement around the blade. A mesh refinement zone was incorporated to provide finer spatial resolution in key areas of separation and eddy shedding. This methodology is used in subsequent three-dimensional studies. Turbulence modelling and boundary conditions match that of the three-dimensional models, save the symmetry walls, and are further discussed in Section 3.3.

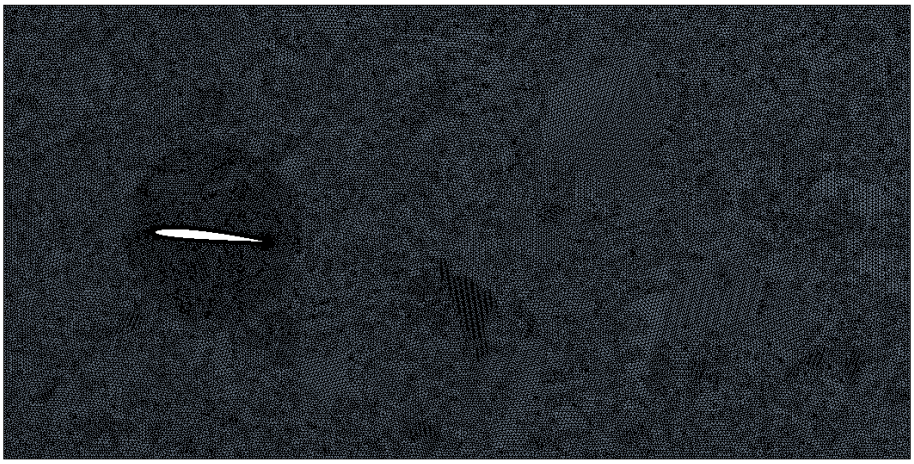

FIGURE 3.4: TWO-DIMENSIONAL MESH

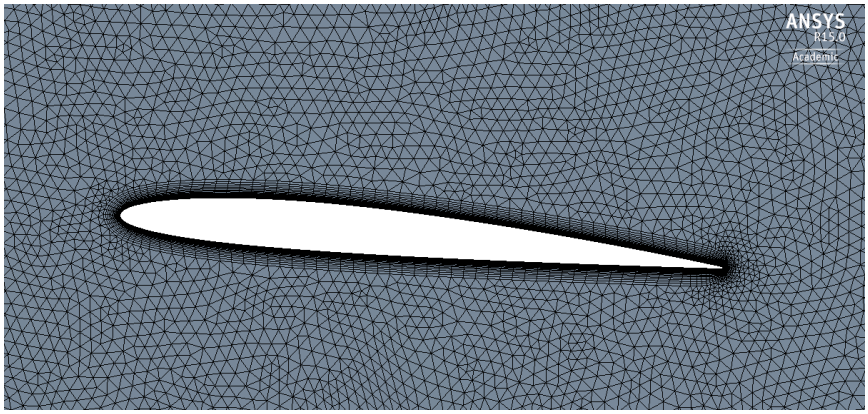

FIGURE 3.5: DETAILED VIEW OF MESH REFINEMENT

3.2. THREE-DIMENSIONAL GEOMETRY

This investigation focussed on a three bladed horizontal axis tidal turbine; specifically, a geometry to match experiments from the University of Southampton (Bahaj *et al.*, 2007a). Figure 3.6 demonstrates the arrangement of the 800 mm diameter rotor within the cavitation tunnel. The orientation provided matches that of this numerical investigation in that the zero yaw scenario was considered with a hub height set at mid-depth.

Blade parameters were provided by way of 17 cross-sectional profiles. Chord, pitch and thickness to chord ratios were given for varying radii and are provided below in Table 3.1.

FIGURE 3.6: PHOTOGRAPH OF EXPERIMENTAL SETUP IN THE CAVITATION TUNNEL (BAHAJ *ET AL.*, 2007A)

TABLE 3.1: BLADE PARAMETERS (BAHAJ *ET AL.*, 2007A)

r/R	Radius [mm]	*c/R*	Pitch Distribution [deg]	*t/c* [%]
0.2	80	0.125	15	24
0.25	100	0.1203	12.1	22.5
0.3	120	0.1156	9.5	20.7
0.35	140	0.1109	7.6	19.5
0.4	160	0.1063	6.1	18.7
0.45	180	0.1016	4.9	18.1
0.5	200	0.0969	3.9	17.6
0.55	220	0.0922	3.1	17.1
0.6	240	0.0875	2.4	16.6
0.65	260	0.0828	1.9	16.1
0.7	280	0.0781	1.5	15.6
0.75	300	0.0734	1.2	15.1
0.8	320	0.0688	0.9	14.6
0.85	340	0.0641	0.6	14.1
0.9	360	0.0594	0.4	13.6
0.95	380	0.0547	0.2	13.1
1.0	400	0.05	0	12.6

The experimental blades consisted of five, 6 series, NACA 63-8XX profiles: NACA 63-812, NACA 63-815, NACA 63-818, NACA 63-821, and NACA 63-824. A nominal profile was obtained and then twisted/scaled using Matlab to achieve the seventeen sections shown in Fig. 3.7. The Matlab codes that achieved this can be viewed in Appendix A. As can be seen in the fourth column of Table 3.1, the blade twists throughout as a consequence of increasing tangential velocity farther along the blade. A total twist change of 15° is experience between the blade root and tip. Figure 3.8 demonstrates that, with a constant fluid speed, an increasing blade velocity (low, medium, high) reduces the incidence angle. As the local tangential velocity of the blade is a function of *r*, a blade twist must be used to maintain the angle of attack. Notice in Fig. 3.7 that the blade tip twists away from the fluid flow, maintaining a desired angle of attack.

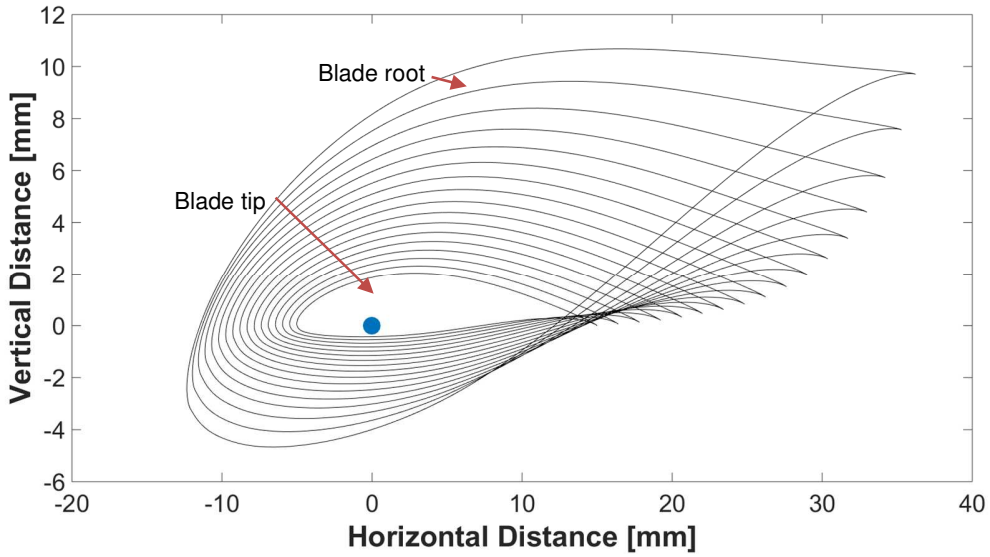

FIGURE 3.7: BLADE CROSS-SECTIONAL PROFILES

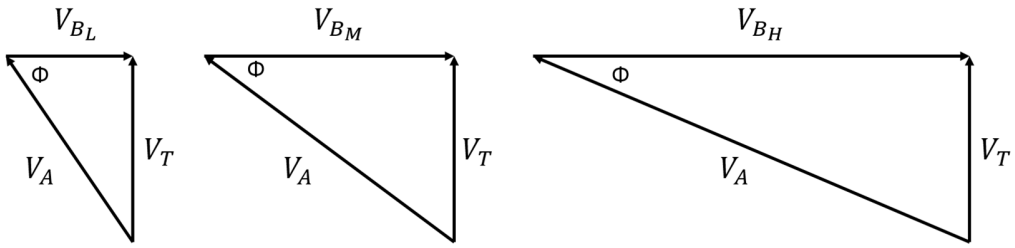

FIGURE 3.8: BLADE VELOCITY AND ANGLE OF ATTACK RELATION

The point in the centre of Fig. 3.7 symbolizes the position of the axis of rotation, representing 25% of the chord from the leading edge for each cross-section. This decision was made through a sensitivity study, see Fig. 3.9, and to match typical industry design. It was shown that the overall power coefficient was impacted significantly in shifting the twist axis away from the leading edge. However, this parameter seemed relatively independent of twist axis location beyond 10% of chord twist length.

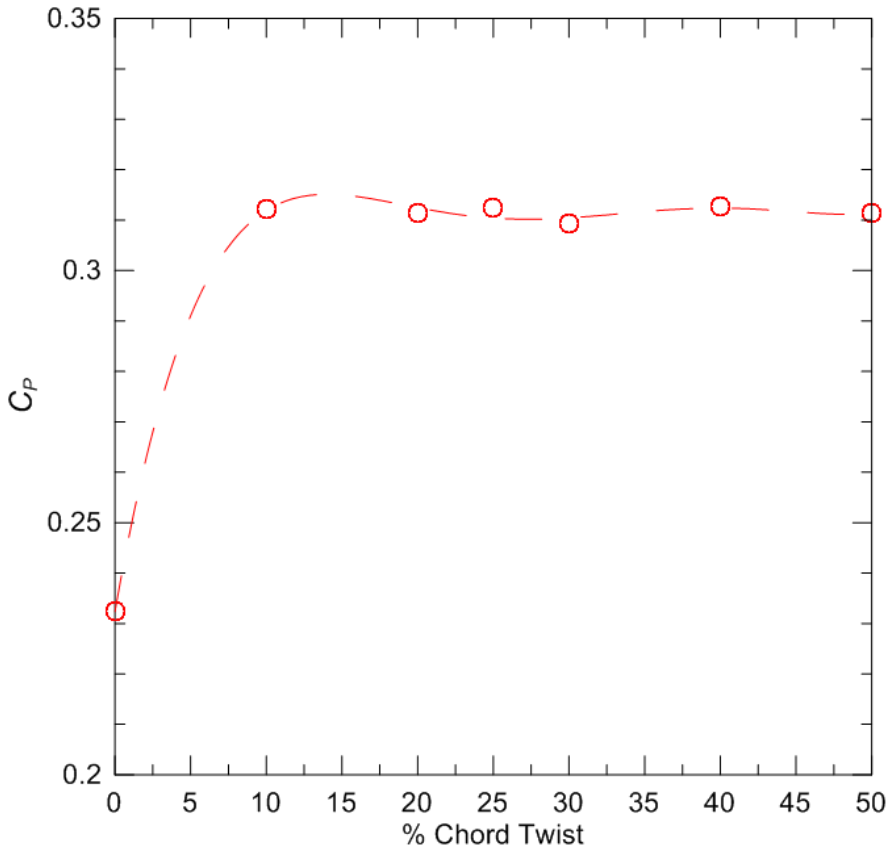

FIGURE 3.9: C_P AS A FUNCTION OF THE BLADE TWIST POSITION – TSR 5

In addition to the twist axis location sensitivity study, a trailing edge roundness study was conducted to determine the impact of trailing edge shape on the performance of the blade. This study used a 5 mm section of the blade starting from the root (r80), an angle of attack of 25° and an inflow speed of 1 m/s. All other flow conditions and angles of attack matched that of the full three-dimensional study. The resulting effect of trailing edge sharpness on the lift force is shown in Fig 3.10. It was shown that adjusting the trailing edge roundness diameter, even to a completely sharp tip, had a significant impact on the lift produced. All results presented henceforth employed a sharp trailing edge.

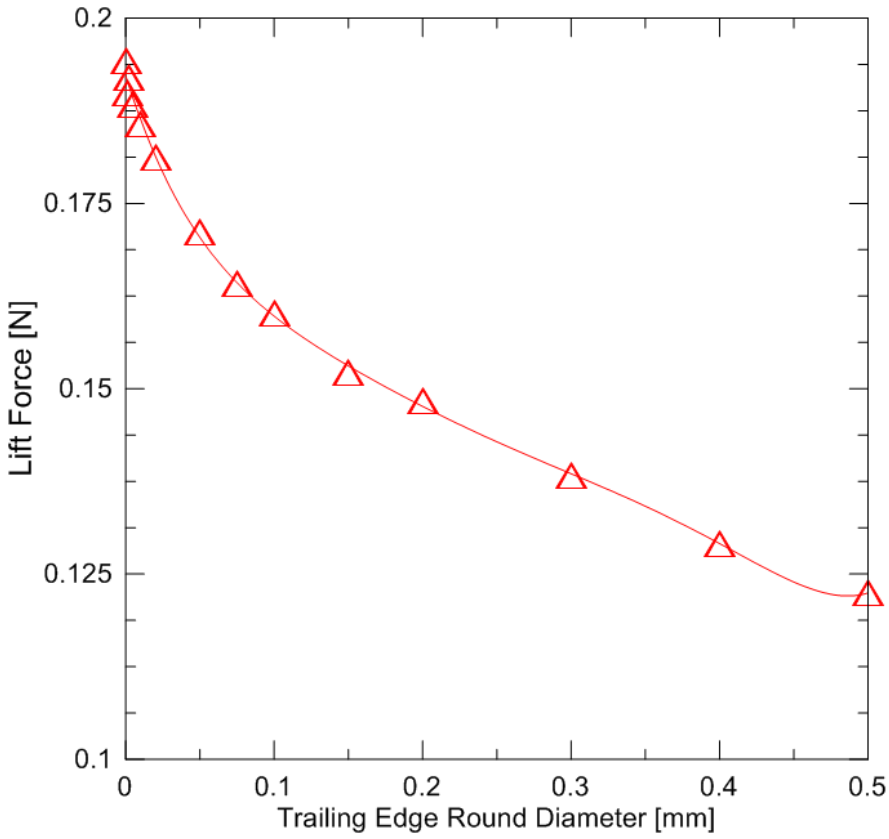

FIGURE 3.10: LIFT FORCE AS A FUNCTION OF THE TRAILING EDGE ROUNDNESS

The fourth column in Table 3.1 presents the ratio of maximum thickness to chord, a ratio that is described in the last two digits of the 6 series NACA designation. The experimental blade has a relatively linear transition from root to tip so a linear transition was applied to the numerical blade. A second Matlab code was created, provided in Appendix B, such that the appropriate seventeen sections be blended together, creating a linear distribution. Figure 3.11 demonstrates the linear distribution method used. The top value (*e.g.* r80) represents the cross-sectional profile at that specific radial distance from the hub centre in mm. Likewise, the lower value (*e.g.* 24 x 1) represents the proportion of NACA 63-8XX used at that cross-section. This specific example indicates that only the NACA 63-824 profile is considered at the radial position of r80. However, the profiles of NACA 63-824 and NACA 63-821 are blended together at r100 with the proportions of 75% and 25%, respectively.

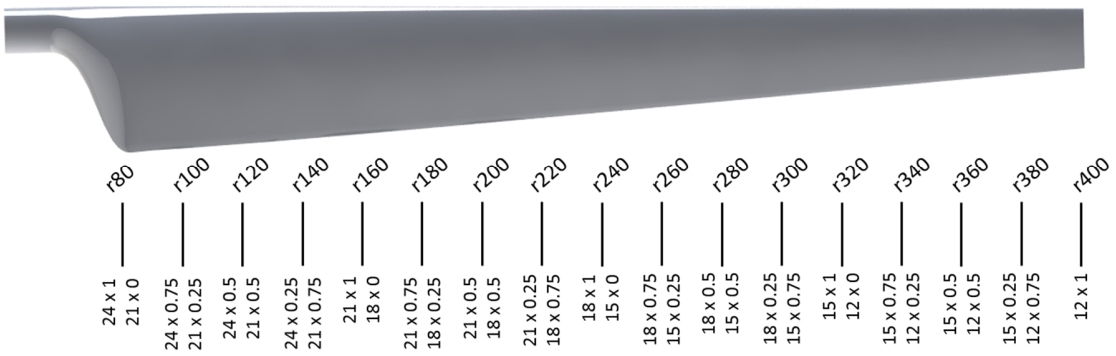

FIGURE 3.11: LINEAR DISTRIBUTION METHOD

Additional profiles near the root were created at 85 mm, 90 mm, and 95 mm to aide in lofting the two-dimensional profiles into a three-dimensional form. These three additional profiles are shown in Fig. 3.12 as dashed lines, between the 80 mm and 100 mm profiles.

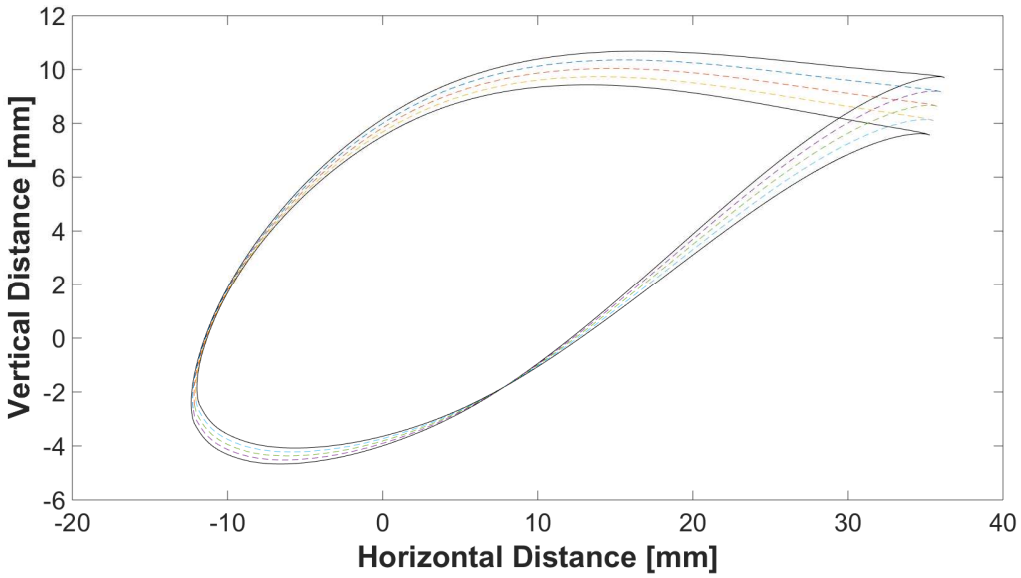

FIGURE 3.12: ADDED ROOT PROFILES

The seventeen profiles, plus the additional three near the root, were exported and lofted in SolidWorks to create the three-dimensional geometry shown in Fig. 3.13. The nacelle and support structure geometries were estimated from review of publications, dimensions of which are provided in Table 3.2. A range of hub pitch angles (15°, 20°, 25°, 27°, and 30°) had been measured using a digital inclinometer during experimentation, where here the angle is set numerically. This investigation focussed on a hub pitch angle of 25° with an inflow velocity of 1.54 m/s.

FIGURE 3.13: THREE-DIMENSIONAL BLADE AND TURBINE GEOMETRIES

TABLE 3.2: NACELLE GEOMETRY DIMENSIONS

Parameter	Dimension
Nacelle Diameter	100 mm
Nacelle Length (tip to tip)	750 mm
Rotor depth	600 mm

3.3. NUMERICAL MODELLING

This section outlines the methodologies employed for the three-dimensional simulations. This includes the fluid domain parameters, boundary conditions and turbulence models used, and the building of the computational mesh.

The majority of simulations were performed using 26 to 30 cores on a Dell Precision T7810, 16 cores (2.4 GHz) hyper-threaded with 128 GB of RAM. Hyper-threading is the name given to processors who can perform as two virtual cores for each physical one; thus, 16 hyper-threaded physical cores can act as 32 virtual cores. A few scenarios were performed using 6 cores on a Dell Precision T5500, 6 cores (3.33 GHz) with 24 GB of RAM. All simulations were run for 1000 iterations, while power and thrust coefficients were used as convergence criteria, ensuring their stability.

3.3.1. FLUID DOMAIN

Experimental tests were completed, in 2007, in the cavitation tunnel at QinetiQ, Haslar, Gosport and in the towing tank at the Southampton Institute (Bahaj *et al.*, 2007a). The cavitation tunnel test-set was chosen for validation purposes. Dimensions of the experimental setup and testing parameters are provided in Table 3.3. These are represented in the numerical fluid domain, save the tank length. Inlet and outlet lengths of 2*D* and 5*D* (where *D* denotes the turbine diameter) are used, respectively. This application of domain size parameters is visually presented below in Fig. 3.14. The rectangular fluid domain has a 1 m diameter, cylindrical subdomain which encapsulates the turbine. In later studies the outlet length, hereafter called downstream domain length, was increased to a maximum of 30*D* for analysis; the methodology and results of which are presented in Sections 3.4.2 and 4.2. For convenient visualization, figures in this chapter representing the fluid domain incorporate a downstream domain length of 5*D*.

TABLE 3.3: CAVITATION TUNNEL PARAMETERS (BAHAJ *ET AL.*, 2007A)

Parameter	Magnitude	Model Magnitude
Length	5 m	7*D* – 32*D*
Breadth	2.4 m	2.4 m – 7.2 m
Height	1.2 m	1.2 m – 3.6 m
Maximum flow speed	8 m/s	1.54 m/s
Pressure range	0.2-1.2 atm	N/A

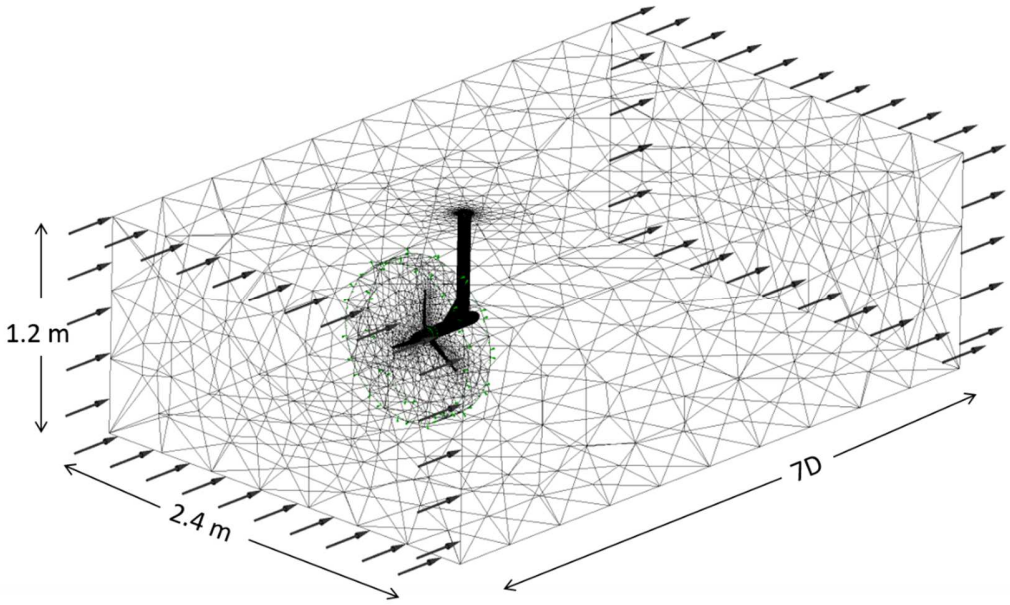

FIGURE 3.14: NUMERICAL FLUID DOMAIN WITH 5*D* DOWNSTREAM DOMAIN LENGTH

A disadvantage of experimental validation is the effect of blockage on fluid phenomena. As the turbine extracts energy from the flow via a momentum drop it causes a flow expansion around/behind it to satisfy the conservation of mass. Incoming flow will see this expansion and be accelerated around it. The tank walls confine this flow and can consequently increase the fluid velocity through the turbine, giving unrealistic results. The tank walls will also limit the expansion of the wake, possibly reducing the recovery distance. With a turbine diameter of 0.8 m these tests experienced a high blockage ratio of $Br = 17\%$. Blockage corrections can be implemented to give a free-stream estimate of the corresponding physics. A blockage correction factor can be applied as a numerical estimate, which is the case for the published experimental results. The experimental researchers applied corrections, originally for propellers, that had been modified for wake expansion (Barnsley & Wellicome, 1990). However, this approach only modifies the resultant turbine performance and neglects blockage effects on the wake.

Another method, computationally, is to expand the domain cross-section area to approximate a free-stream flow. This method both modifies the power and thrust coefficient as well as giving the wake a larger expansion area. This method was applied and compared to the original results. The domain's height and width were both doubled in size. The results of this study are provided and discussed in Section 5.3.

3.3.2. NUMERICAL SETUP

ANSYS CFX determines the pressure and velocity fields in the fluid through the resolution of the Navier-Stokes equations introduced in Chapter 2. For convenience the continuity equation and one direction of the momentum equations are repeated below.

$$\frac{\partial \bar{u}}{\partial x} + \frac{\partial \bar{v}}{\partial y} + \frac{\partial \bar{z}}{\partial z} = 0 \tag{3.3}$$

$$\rho\left[\frac{\partial}{\partial x}(\bar{u}^2)+\frac{\partial}{\partial y}(\bar{u}\bar{v})+\frac{\partial}{\partial z}(\bar{u}\bar{w})\right] = -\frac{\partial \bar{P}}{\partial x} + \left[\frac{\partial}{\partial x}\left(\mu\frac{\partial \bar{u}}{\partial x}-\rho\overline{u'^2}\right)+\frac{\partial}{\partial y}\left(\mu\frac{\partial \bar{u}}{\partial y}-\rho\overline{u'v'}\right) + \frac{\partial}{\partial z}\left(\mu\frac{\partial \bar{u}}{\partial z}-\rho\overline{u'w'}\right)\right] \tag{3.4}$$

Boundary conditions are employed to resolve these differential equations, and are provided in Table 3.4. The fluid domain consists of two sub-domains, one rotating enveloping the turbine and one stationary, see Fig. 3.14. The rotating speed of the cylindrical domain, or of the reference frame when using the Frozen Rotor (quasi-steady state) option, is set to achieve a desired tip speed ratio.

TABLE 3.4: BOUNDARY CONDITIONS

Boundary	Condition
Inlet	Normal Speed = 1.54 m/s
Inlet Turbulence	Zero Gradient
Outlet	P_{rel} = 0 Pa
Outer Walls	Free-Slip Condition
Turbine Walls	No-Slip Condition
Domain Interfaces	Frozen Rotor

The alternate rotation model in CFX was used. "This model advects the absolute frame velocity, rather than the relative frame velocity. The alternate rotation model makes a significant reduction in numerical error when the absolute frame flow is essentially a constant flow parallel to the axis of rotation. For example, the approaching flow to a fan or propeller is nearly constant in the absolute frame, but highly rotating flow in the relative frame" (ANSYS, 2013).

Cavitation inception was neglected in the model as this adds unnecessary complexity. The experimental data set used as validation in this study also investigated the onset of cavitation. It was found that cavitation typically appeared at TSR values greater than 7, and even then in only a few scenarios (Bahaj *et al.*, 2007a).

It is convenient for model development, solution monitoring and post processing to create expressions and variables. This is done by writing functions in CFX Expression Language (CEL) format, an example of which is found in Appendix C. For example, rather than changing multiple inputs for varying scenarios, the user need only adjust the desired TSR. The angular velocity is then defined as a function of TSR, which is then used to calculate and monitor the power coefficient during simulation. This approach can also be used to aide in post-processing. For example, turbulence intensity can quickly be analysed in CFD-Post by accessing the CEL for *turbIntensity* which utilizes the pre-defined function of Turbulence Kinetic Energy.

3.3.3. TURBULENCE MODELS

Table 3.5 reveals the local velocity magnitude, Reynolds number and angle of attack experienced in the model for five points along the blade at three TSRs. In general, on the length scale of the blade chord, the boundary layer is expected to be turbulent when assessing the Reynolds number. On the turbine scale the flow is also expected to be turbulent with a $Re_D = 1.38 \times 10^6$. Re_D indicates that the turbine diameter, and inflow speed, are being used to determine the Reynolds number while Re_C indicates that the appropriate blade chord and apparent speed are used.

There is quite a high angle of attack experienced along the majority of the blade for low rotation rates. High angles of attack result in flow separation, a phenomena which is associated with low lift and high drag (discussed in Section 5.1). For this reason it is imperative to choose a turbulence model which is capable of accurately modelling viscous effects in the viscous sublayer. It should also be noted that the blade tip experiences negative angles of attack at high TSRs. Again, flow separation will be a factor and appropriate choice of turbulence model is key. A dramatic drop in lift is expected in this region while drag will be effected less so in moderately negative angles of attack.

TABLE 3.5: LOCAL VELOCITY, REYNOLDS NUMBER, AND ANGLE OF ATTACK

	Location	V_A (m/s)	Re_C	α
TSR 3.5	r80 (Root)	1.078	1.38×10^8	30.01
	r160	2.156	2.35×10^8	19.44
	r240	3.234	2.90×10^8	13.06
	r320	4.312	3.04×10^8	8.75
	r400 (Tip)	5.390	2.76×10^8	5.95
TSR 5	r80 (Root)	1.540	8.63×10^7	20.00
	r160	3.080	1.47×10^8	10.46
	r240	4.620	1.81×10^8	6.03
	r320	6.160	1.90×10^8	3.14
	r400 (Tip)	7.700	1.73×10^8	1.31
TSR 8	r80 (Root)	2.464	1.38×10^8	7.01
	r160	4.928	2.35×10^8	1.25
	r240	7.392	2.90×10^8	-0.63
	r320	9.856	3.04×10^8	-2.02
	r400 (Tip)	12.32	2.76×10^8	-2.87

The Shear Stress Transport (SST) turbulence model was chosen for the bulk of this investigation as it has been proven to have an acceptable balance between accuracy and computational effort. This model blends the $k - \varepsilon$ and $k - \omega$ models using the relations presented in Section 2.2.3. One flow scenario (TSR 5) has been completed using both the $k - \varepsilon$ and $k - \omega$ models to ascertain their deficiencies. The impact on the wake of this study and turbine performance are discussed in Section 6.1.

3.3.4. COMPUTATIONAL MESH

The computational mesh was built in ANSYS Mesher using unstructured tetrahedral elements to allow for the best representation of the geometry. Figure 3.14 is a representative example of a mesh used. The majority of the domain is expressed as a stationary domain, whereas a cylindrical mesh subdomain envelopes the turbine and rotates at prescribed rates.

Figure 3.15 demonstrates the approach taken to ensure a sharp trailing edge on the blade. A set of six bodies were created in SolidWorks that envelopes the blade and are meshed individually. However, the inflation layer around the blade does not fill these bodies. This approach also allows for local mesh refinement, *e.g.* curvature on the leading edge.

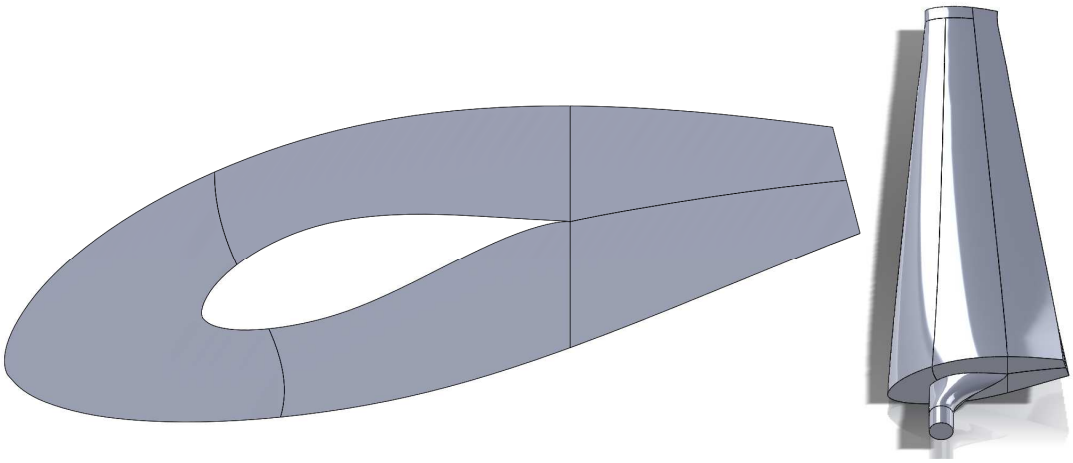

FIGURE 3.15: REFINEMENT MESH REGION SURROUNDING BLADE

Inflation layers are incorporated at the turbine and nacelle walls to better resolve the boundary layer flow, see Fig. 3.16 for an example of the blade mesh. The inflation layer around the blade does not fill the fluid domain shown in Fig. 3.15, however this subdivision allowed for localized and ordered mesh refinement.

It was desired to numerically resolve the boundary layer rather than use wall functions. The Low-Reynolds-Number method was employed by ensuring an adequate inflation layer was used. The boundary layer mesh was refined until $y^+ \approx 4$, which is acceptable as $y^+ < 11$ indicates that the first node is within the laminar sublayer and Low Reynolds Method will be employed (ANSYS, 2013). Figures 3.17, 3.18 and 3.19 provide detailed views of the refined mesh at the hub and blade root. Table 3.6 presents the range of y^+ values for the blades and nacelle. With the exception of a small zone on the blade tip with a value of 43.5, y^+ values remain below 8 at the blades.

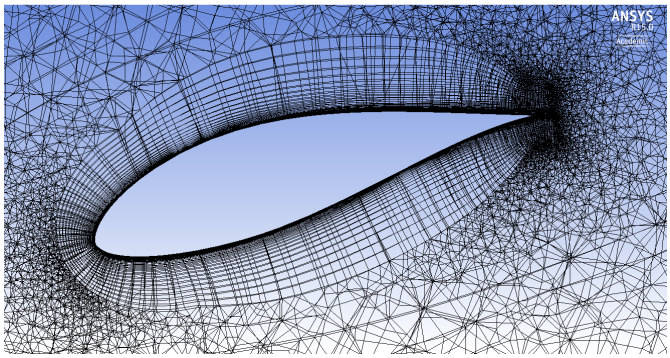

FIGURE 3.16: DETAILED VIEW OF BLADE INFLATION LAYER

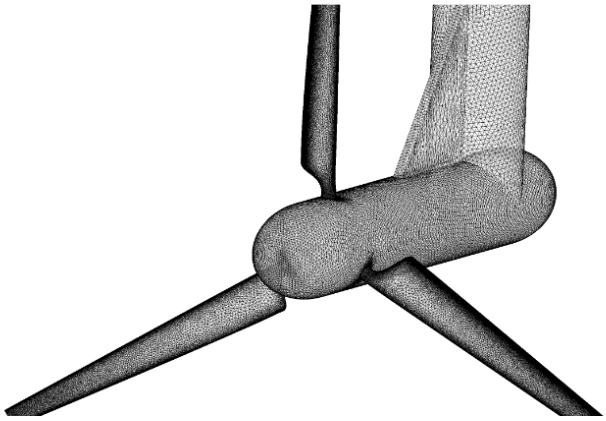

FIGURE 3.17: DETAILED VIEW OF TURBINE MESH

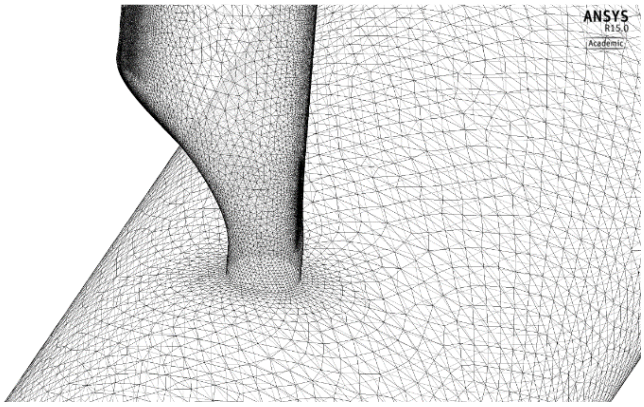

FIGURE 3.18: DETAILED VIEW OF BLADE ROOT

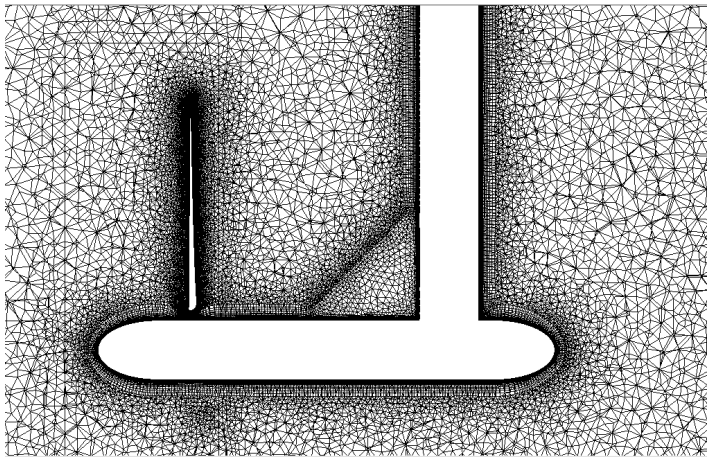

FIGURE 3.19: DETAILED VIEW OF TURBINE INFLATION MESH

TABLE 3.6: LOCALIZED y^+ RANGE

	y^+ - Blades	y^+ - Nacelle
Minimum	0.140849	0.188931
Maximum	43.5406	8.61866
Average	3.70865	4.01792

3.4. MESH CONVERGENCE AND SENSITIVITY STUDIES

This section will introduce the motives and methodologies behind the mesh convergence and sensitivity studies considered for this study. The results of these studies will be provided later in Chapter 4.

Mesh convergence studies were completed to ensure result independence of any finer spatial resolutions. Refinement included adjustments of maximum cell face size, minimum cell size and curvature normal angle. A wake mesh density convergence study was then completed in which the cell size was restricted within a body of influence behind the turbine. Both the thrust and power coefficients are considered for convergence criteria. They are also used later for validation purposes. Velocity deficit and turbulence intensity are also considered as convergence criteria. In addition, they are of consideration for downstream domain length and cross-section are sensitivity studies. These values provide insight into the occurring wake physics.

3.4.1. WAKE MESH STUDY

A wake convergence study was completed wherein a body of influence, a zone of localized mesh controls in ANSYS Mesher, was imposed. Figure 3.20 demonstrates that a cylindrical body of influence was used with a specified local maximum cell size. Six meshes were studied with varying local wake mesh size, see Table 3.7. Results from this convergence study are discussed in Section 4.1. Mid-plane cross-sections and rear views of meshes 1 through 6 are shown in Fig. 3.21, illustrating the method of local mesh refinement.

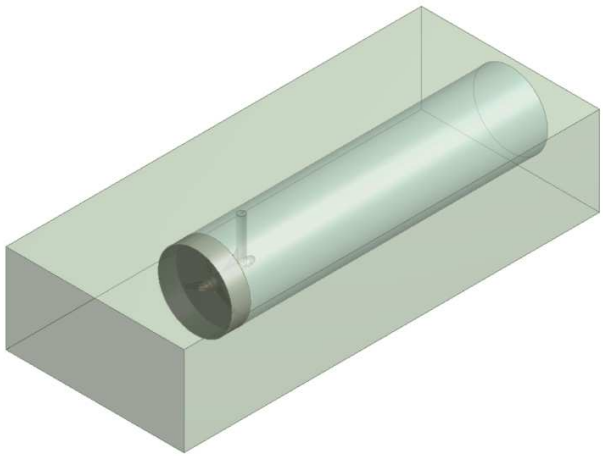

FIGURE 3.20: BODY OF INFLUENCE

TABLE 3.7: WAKE MESH CONVERGENCE PARAMETERS

	Wake Cell Size [m]	# of Elements	Min. Quality	Max. Quality	Avg. Quality
Mesh 1	0.3	35,282,156	2.7345×10^{-4}	0.9999	0.6799
Mesh 2	0.2	35,285,617	2.7345×10^{-4}	0.9999	0.6800
Mesh 3	0.1	35,323,980	2.7345×10^{-4}	0.9999	0.6801
Mesh 4	0.05	35,556,852	2.7345×10^{-4}	0.9999	0.6812
Mesh 5	0.025	37,400,883	2.7345×10^{-4}	0.9999	0.6829
Mesh 6	0.0125	50,978,189	2.7345×10^{-4}	0.9999	0.7314

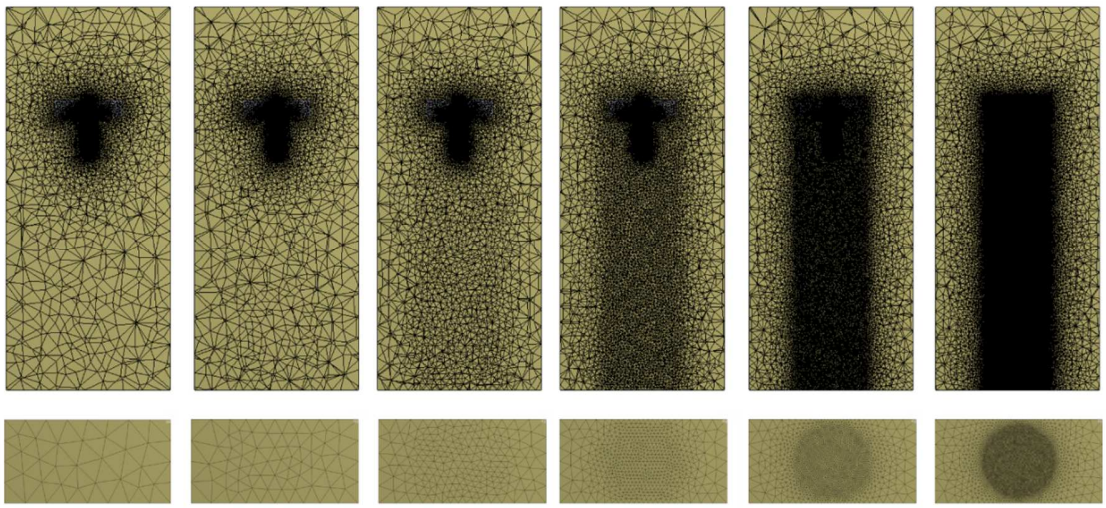

FIGURE 3.21: MID-PLANE CROSS-SECTIONS AND REAR VIEWS – MESHES 1 THROUGH 6

3.4.2. DOMAIN LENGTH STUDY

This study initially employed a downstream domain lengths of 5*D*. It was of interest however to determine the effect the domain length has on turbine performance as well as wake recovery. A domain length sensitivity study was carried out, applying the same body

of influence method provided above, in which the effect of downstream distance was studied. Domain lengths of 5*D*, 10*D*, 20*D*, and 30*D* were studied. Methods of analysis mainly focussed on wake physics (velocity deficit, centreline velocity, *etc.*) but power and thrust coefficient were also calculated. Only a TSR of 5 was applied in these studies. Mesh 5 was used in all domain length studies as Mesh 6 drastically increased the element count beyond a reasonable value. The element count for the varying domain lengths are provided in Table 3.8.

TABLE 3.8: DOMAIN LENGTH STUDY ELEMENT COUNT

	# of Elements	Min. Quality	Max. Quality	Avg. Quality
5*D*	37,400,883	2.7345×10^{-4}	0.9999	0.6829
10*D*	41,652,842	1.7891×10^{-3}	0.9999	0.6903
20*D*	43,787,009	5.2025×10^{-4}	0.9999	0.7122
30*D*	46,431,002	$5.9063e10^{-4}$	0.9999	0.7249

3.4.3. BLOCKAGE EFFECTS

As discussed in Section 3.3.1, expanding the domain cross-section allows for analysis of the blockage effect on both the turbine performance as well as wake expansion. The effect of blockage on the turbine performance was determined by doubling the cross-sectional area of the fluid domain. By increasing the domain height and width to 4.8 m and 2.4 m the blockage ratio was decreased from 17% to 8.5%. Likewise, for one case, a domain with a tripled aspect ratio was used, reducing the blockage ratio to 5.6%. Figure 3.22 presents a visual representation of these domains. The results of this study are discussed in Sections 5.3 and 6.2.1.

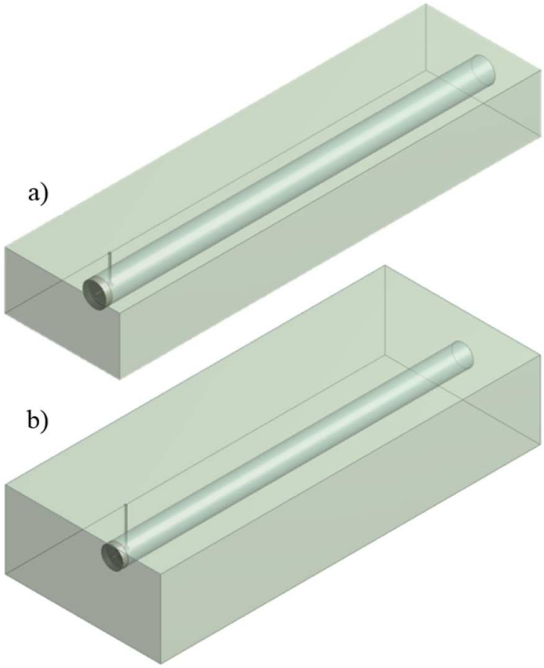

FIGURE 3.22: FLUID DOMAIN WITH AN INCREASED CROSS-SECTIONAL AREA: A) DOUBLE AND B) TRIPLE

CHAPTER 4 MESH CONVERGENCE AND SENSITIVITY STUDIES

This section will provide the results and discussion of the mesh convergence and sensitivity studies outlined in the previous chapter. Power and thrust coefficients will be used to analyse the effects on turbine performance while velocity deficit and turbulence intensity are used to study the wake effects.

One method of analysis used henceforth is examination of key variables along sample lines of the wake solution. Figure 4.1 demonstrates the horizontal, vertical, and centreline sampling method. This image shows samples at 1D, 2D, 3D, 4D, and 5D in the wake while longer domain solutions may examine further at 8D, 10D, 12D, 15D, 18D, 20D, and 30D.

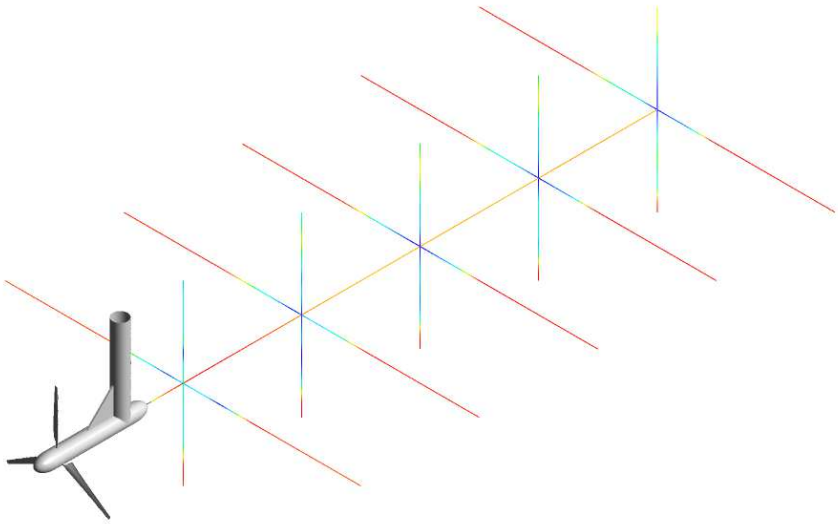

FIGURE 4.1: SAMPLE LINE DEMONSTRATION

4.1. WAKE MESH CONVERGENCE STUDY

A wake mesh convergence study was completed as described in Section 3.4.1. Simulation times ran from 4 hours for the coarser Mesh 1 to 23 hours for the finest Mesh 6. It was found that the effect of wake mesh density on the turbine power and thrust coefficients was insignificant, see Fig. 4.2. This result is promising for researchers who are more interested in design optimization than wake physics as a relatively coarse wake mesh would possibly suffice. Velocity deficit and downstream turbulence intensity were chosen as additional

metrics to determine the impact of mesh sizing on the downstream flow. These are described in Eqs. (2.24) and (2.25).

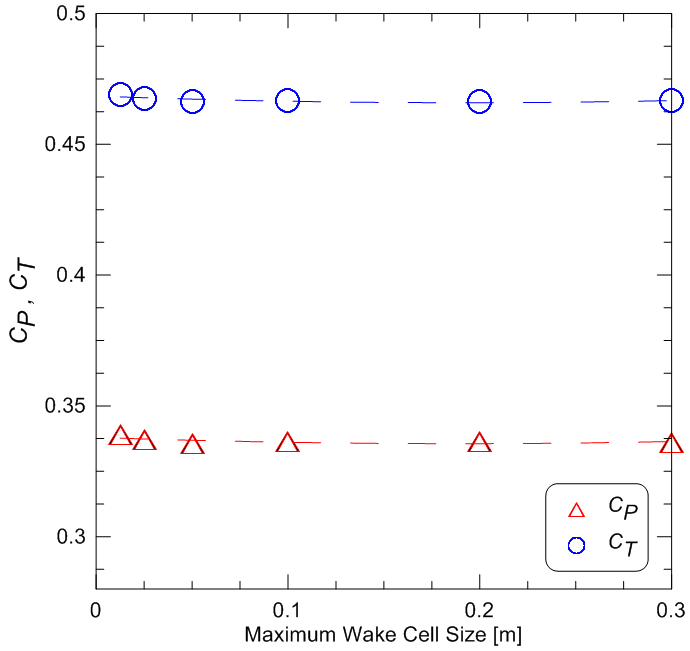

FIGURE 4.2: C_P AND C_T AS A FUNCTION OF THE MAXIMUM WAKE CELL SIZE FOR TSR 5

Figures 4.3a), c), e) show velocity deficit along horizontal sample lines at 1D, 3D and 5D downstream of the turbine for TSR 5; on the figures, x/D and y/D = 0 indicates the hub centre position. By three diameter lengths away from the turbine the coarsest meshes show significant recovery in wake velocity. Meshes 1 and 2 demonstrate the necessity of mesh convergence studies. Mesh 2, while slightly finer than Mesh 1, gives the fastest wake recovery with complete recovery at five diameter lengths downstream. Velocity deficit begins to converge as mesh density is increased in the wake regions. Likewise, Figs. 4.3b), d), f) show velocity deficit at vertical sample lines. Greater fluctuations are observed on the vertical sample line due to flow interaction with the mast. The two finest meshes tend to capture these fluctuations. In the vertical sample line there is a peak velocity deficit, particularly pronounced at 5D, at the y/D position of -0.5. This location corresponds with the blade tip. As mentioned earlier, it is typical for the near wake to be bound by tip-shed vortices. It is expected that convective and turbulent processes will break down the wake, energizing it further downstream.

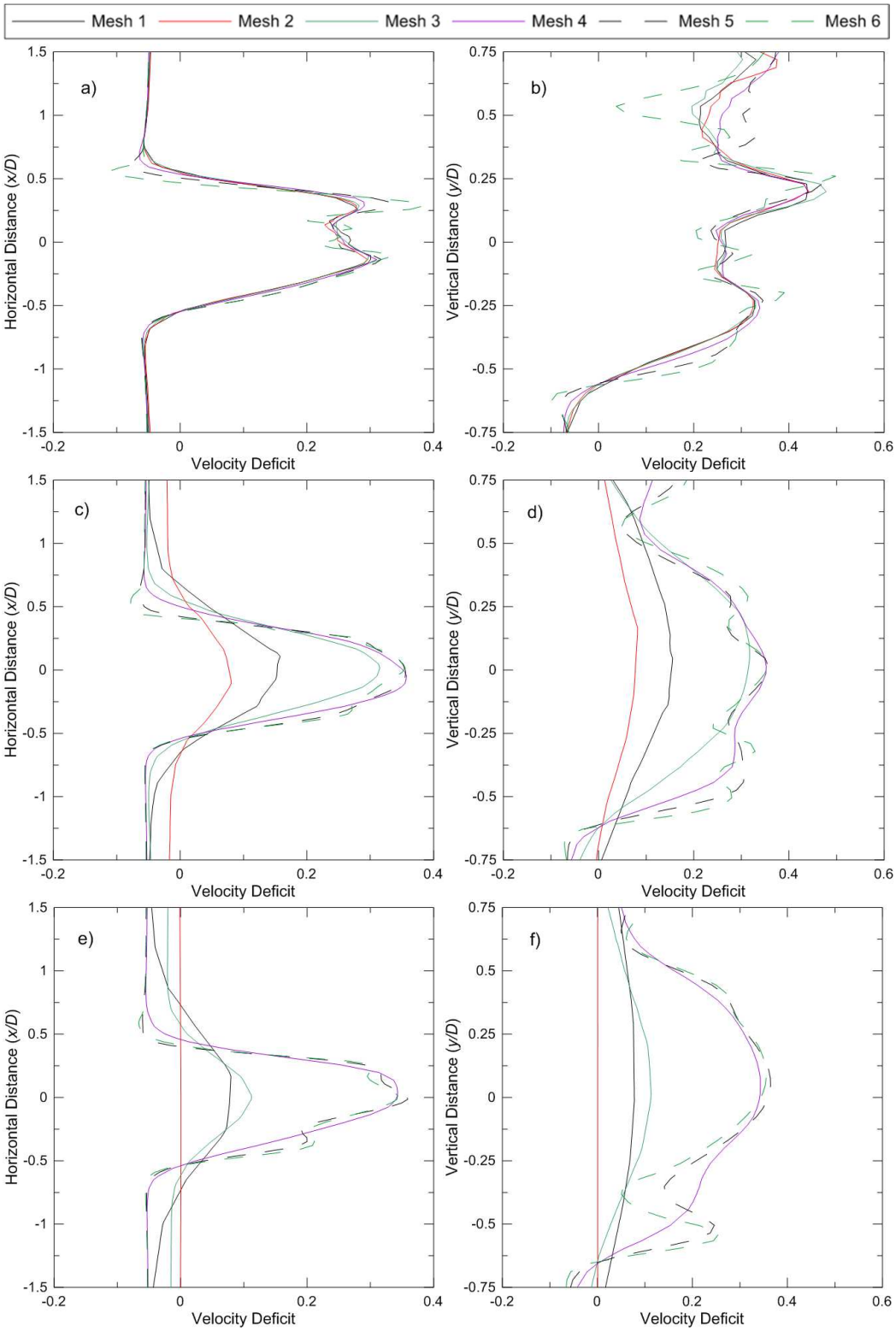

FIGURE 4.3: VELOCITY DEFICIT: A) HORIZONTAL – 1D, B) VERTICAL – 1D, C) HORIZONTAL – 3D, D) VERTICAL – 3D, E) HORIZONTAL – 5D, F) VERTICAL – 5D

Similarly, Figs. 4.4a), c), e) and Figs. 4.4b), d), f) provide horizontal and vertical turbulence intensities at 1*D*, 3*D* and 5*D* for TSR 5. All mesh solutions generally agree with each other at 1*D* but deviate further downstream. Mesh 1 for example exhibits a full wake recovery by 5*D* while mesh 6 still experiences maximum turbulence intensities of 5.35% and 5.0% at the outlet on the horizontal and vertical sample lines, respectively. Non-symmetry in the horizontal solution is attributed to a combination of swirl in the wake due to rotating machinery and fluid interaction with the nacelle support structure. The same effect can be said for the vertical sample line, with greater turbulence intensity near the top of the domain.

The vertical samples of turbulence intensity display three distinct peaks. The peaks, located at $y/D = 0$ and ± 0.5, correspond to blade root and blade tip turbulence. These two areas of abrupt planform change are commonly associated with vortex creation. A corollary of this is an increase in turbine drag and a possible increase in wake propagation. The addition of slight design modifications, *e.g.* winglets, could help reduce this unnecessary loading and noise scenario as well as mitigate wake encapsulation.

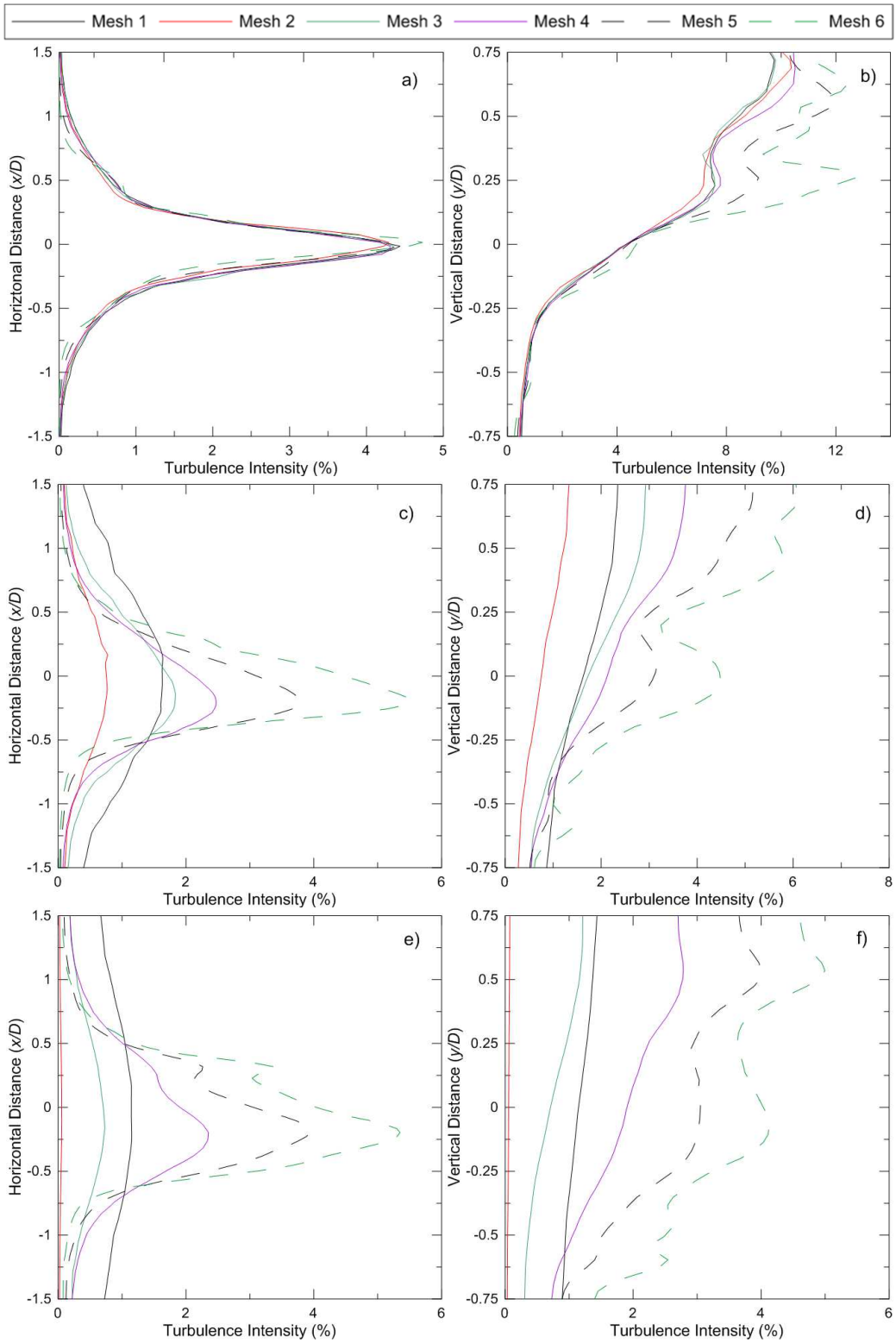

FIGURE 4.4: TURBULENCE INTENSITY: A) HORIZONTAL – 1D, B) VERTICAL – 1D, C) HORIZONTAL – 3D, D) VERTICAL – 3D, E) HORIZONTAL – 5D, F) VERTICAL – 5D

Figure 4.5 shows the normalized velocity flow-field of Mesh 1 and Mesh 6 for a visual comparison of the impact of mesh density in the wake. Mesh 1 shows a quick recovery with almost no deficit by 5*D* while the Mesh 6 wake extends well beyond the domain. A partition is formed in the Mesh 6 wake in which there is localized flow acceleration; this occurrence can be seen graphically in Fig. 4.3f) and is discussed in Section 6.2. Mesh 6 is also more capable of capturing recirculation directly behind the nacelle support structure. Figure 4.6 highlights the finer mesh's ability of capturing the von Kármán vortex street shed from the support structure. This aerial view is a slice taken at $y/D = 0.56$, just above the top blade's tip. It is believed that the tip-shed vortices initialized the repeating swirling flow at the mast. This event would be better captured with a transient simulation as this phenomenon is truly unsteady.

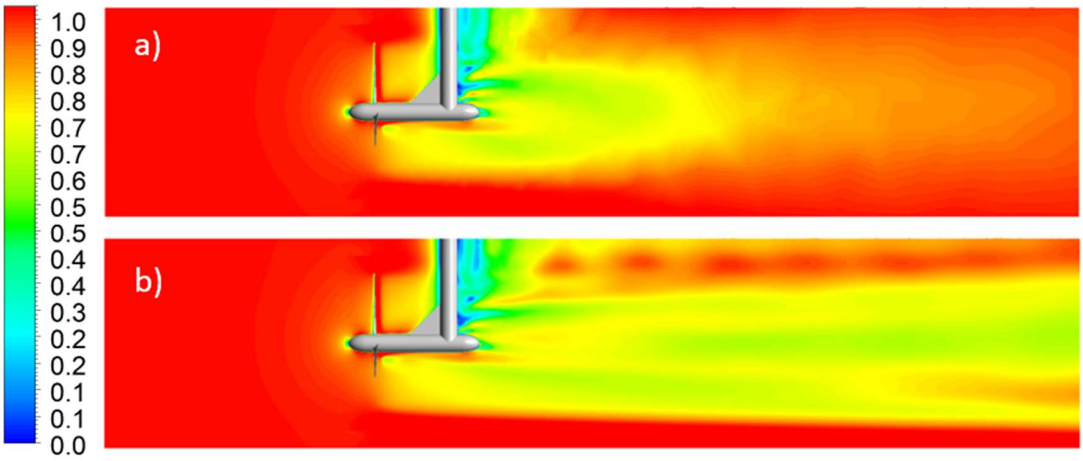

FIGURE 4.5: NORMALIZED VELOCITY V/V_0 ON MID-VERTICAL PLANE A) MESH 1, B) MESH 5

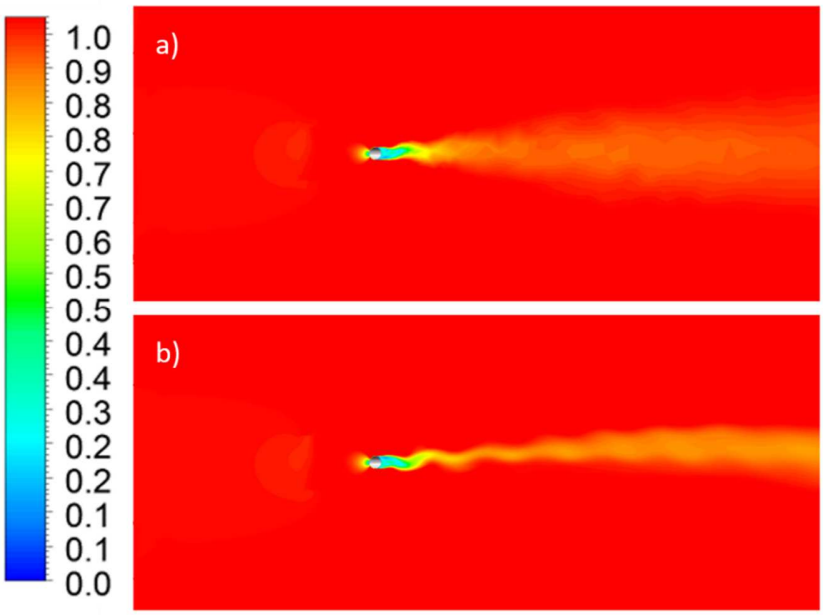

FIGURE 4.6: NORMALIZED VELOCITY V/V_0 AT AERIAL VIEW OF $Y/D = 0.56$ A) MESH 1, B) MESH 5

Mesh 6, the most refined wake mesh, resolved fluid turbulence that was undetected or under-estimated otherwise. However, Mesh 5 resolved wake physics comparable to Mesh 6 while no appreciable difference in turbine performance was observed. Mesh 5 required less effort to generate and enjoyed a significantly reduced computation time. For the TSR 5 scenario computation times were 16 hours and 23 hours for Mesh 5 and Mesh 6, respectively.

For this reason, Mesh 5 was chosen for all subsequent studies. It is clear from this study that a downstream fluid domain length of 5*D*, for wake physics analyses, is inadequate but is acceptable if turbine performance is the soul concern. Mesh 6 has a maximum velocity deficit of 0.35 and maximum turbulence intensity of 5.35% at 5*D*, roughly at hub height and mid-plane. An investigation into domain length sensitivity is reported on in Section 4.2.

4.2. DOMAIN LENGTH SENSITIVITY STUDY

A domain length sensitivity study was completed wherein the downstream domain length ranged from 5*D* to 30*D*. All simulations for this sensitivity study used Mesh 5 described in Section 3.4.1 as Mesh 6 resulted in an unreasonable element count for the longer domains. Simulation times ranged from 16 hours for 5*D* to 20 hours for 30*D*. It was

observed that increasing the downstream domain length has minimal effects on the turbine performance. This is portrayed in Table 4.1, tabulating the power and thrust coefficients for the four cases.

TABLE 4.1: C_P AND C_T AS FUNCTIONS OF DOMAIN LENGTH – TSR 5

	C_P	C_T
5D	0.336958	0.467428
10D	0.337000	0.467390
20D	0.337175	0.467231
30D	0.336249	0.466072

Table 4.2 outlines turbine performance for a full TSR range with the 5D and 20D downstream domain lengths. Again, there is no appreciable difference in turbine performance at all flow scenarios with an increased domain length.

TABLE 4.2: C_P AND C_T AT 5D AND 20D DOMAIN LENGTHS – TSR 5

TSR	C_P - 5D	C_P - 20D	Rel. Diff. (%)	C_T - 5D	C_T - 20D	Rel. Diff. (%)
3.5	0.2883	0.2876	-0.3	0.3940	0.3933	-0.2
4	0.3174	0.3164	-0.3	0.4306	0.4296	-0.2
5	0.3389	0.3372	-0.5	0.4691	0.4672	-0.4
5.5	0.3336	0.3315	-0.6	0.4734	0.4707	-0.6
6	0.3186	0.3176	-0.3	0.4688	0.4674	-0.3
7	0.2649	0.2644	-0.2	0.4403	0.4398	-0.1
7.5	0.2261	0.2259	-0.1	0.4179	0.4175	-0.1
8	0.1774	0.1792	1.0	0.3894	0.3911	0.4

Figure 4.7a) presents the centreline velocity deficit for the domain length study results. In all cases there is a sharp decline initially as a result of an area of stagnation behind the nacelle support. There is a period of a general recovery trend between 3 and 7.5 diameter lengths downstream. After this period a slope of fast recovery occurs until there is virtually no deficit at 11 diameter lengths. Similarly, Fig. 4.7b) shows a slow reduction in vorticity between 3D and 7.5D and a sharp decline beyond 8D. There is a noticeable spike in vorticity at 8D, possibly contributing to the increased rate of wake recovery. This spike is likely due to the interaction of reflected flow from the domain walls with spiralling tip-shed vortices.

This unexpected early recovery could be due to blockage. Bahaj *et al.* reported on porous disks experiments, with a blockage ratio of 2%, in which full recovery was not seen even at 20 diameter lengths (Bahaj *et al.*, 2007b). The blockage ratio of this investigation is 17%, the effect of which is discussed in Sections 5.3 with regards to turbine performance. It is possible that the wake begins to interact with the tank walls and reflect inward near 8*D* downstream. For this reason a scenario was considered for twice the domain cross-section and a 20 diameter length downstream distance. The results for this are given in Section 6.2.1.

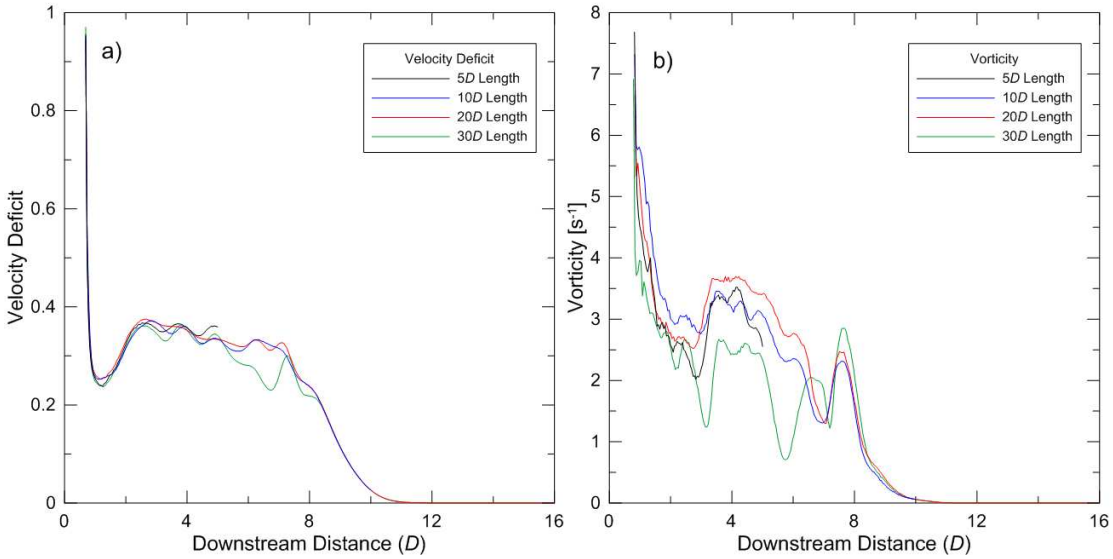

FIGURE 4.7: CENTRELINE RESULTS FROM DOMAIN LENGTH SENSITIVITY STUDY: A) VELOCITY DEFICIT, B) VORTICITY

Figures 4.8a), c), e) and 4.9a), c), e) provide velocity deficit and turbulence intensity results for the horizontal sample line at 1*D*, 3*D*, and 5*D*, respectively, for the four downstream domain length cases. Likewise, Figs. 4.8b), d), f) and 4.9b), d), f) provide the same results but for the vertical sample line. In general, all domain lengths provide the same level of detail in wake flow. This result indicates that a downstream domain length of 5*D* is sufficient for both turbine performance analysis and near wake analysis, for this turbine setup. However, it is clear that a 5*D* domain length is insufficient for capturing full wake recovery. Henceforth, the majority of the presented results were gleaned from a 20*D* downstream domain length. The exception is the turbulence model comparison test, see Section 6.1, which used a 5*D* downstream domain length.

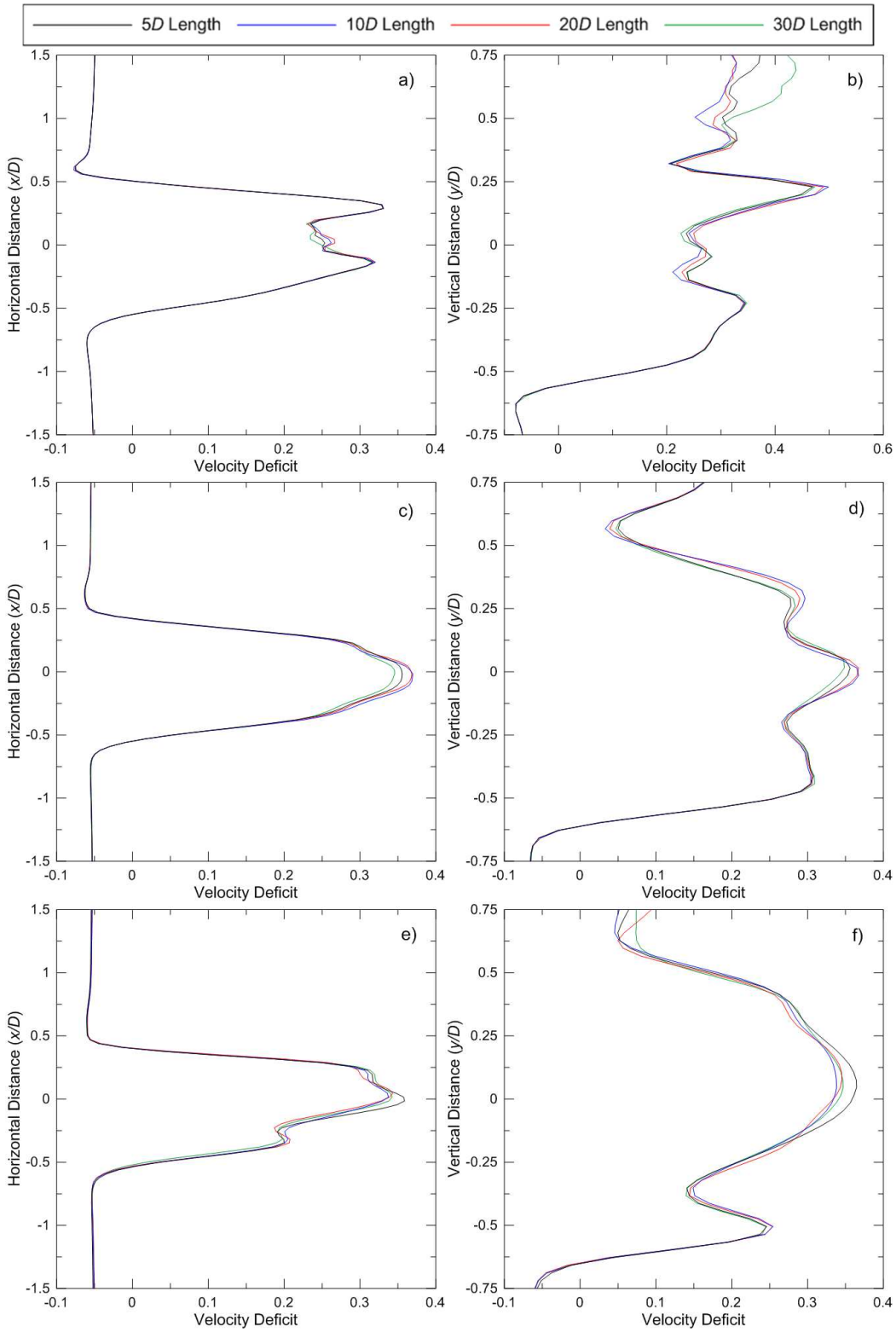

FIGURE 4.8: VELOCITY DEFICIT WITH VARYING DOWNSTREAM DOMAIN LENGTHS: A) HORIZONTAL – 1D, B) VERTICAL – 1D, C) HORIZONTAL – 3D, D) VERTICAL – 3D, E) HORIZONTAL – 5D, F) VERTICAL – 5D

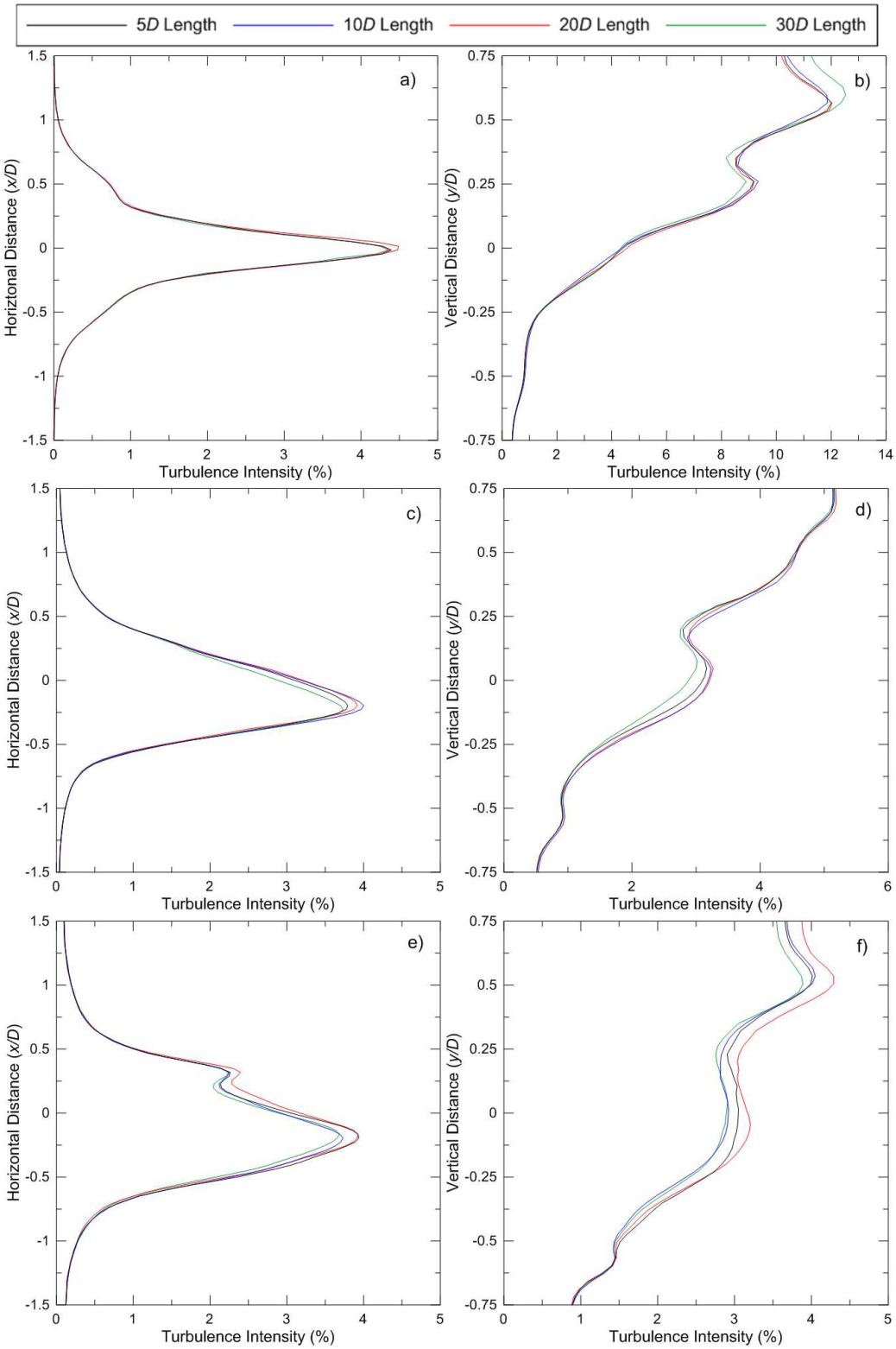

FIGURE 4.9: TURBULENCE INTENSITY WITH VARYING DOWNSTREAM DOMAIN LENGTHS: A) HORIZONTAL – 1D, B) VERTICAL – 1D, C) HORIZONTAL – 3D, D) VERTICAL – 3D, E) HORIZONTAL – 5D, F) VERTICAL – 5D

CHAPTER 5 MODEL VALIDATION

5.1. TWO-DIMENSIONAL VALIDATION

A two-dimensional analysis of a NACA 1408 airfoil was run over a range of angles of attack. Both lift, Fig. 5.1, and drag, Fig. 5.2, coefficients showed good agreement until an angle of attack of 10°. The CFX prediction reaches stall much sooner than XFOIL, causing a reduction in lift and increase in drag. This divergence from expected results is due to severe separation at high angles of attack, a fluid physics that is difficult to resolve numerically. The validation data set was collected using an inviscid version of XFOIL; thus, a true separation would not be captured. Figures 5.1b) and 5.2b) compare the results from an angle of attack range of -7.5° to 7.5°. This region had an average relative difference of 5.7% and absolute difference of 0.005 for the lift coefficient and 45% and 0.009 for the drag coefficient. This result is considered acceptable; this study focussed more on the result magnitude and trends rather than absolute values as the data for comparison derived from a simplified potential flow model.

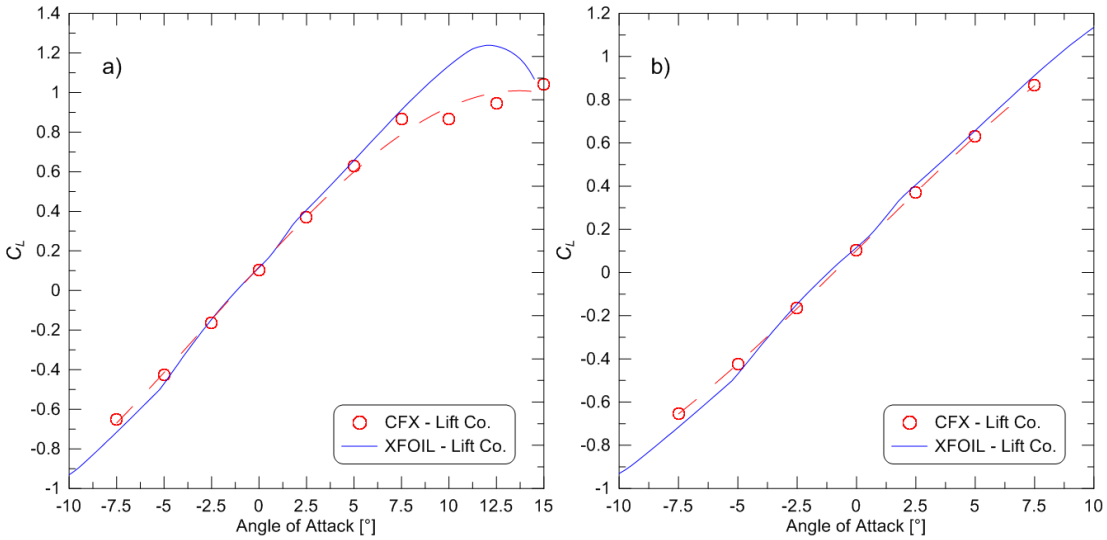

FIGURE 5.1: LIFT COEFFICIENTS: A) FULL RANGE, B) STABLE RANGE

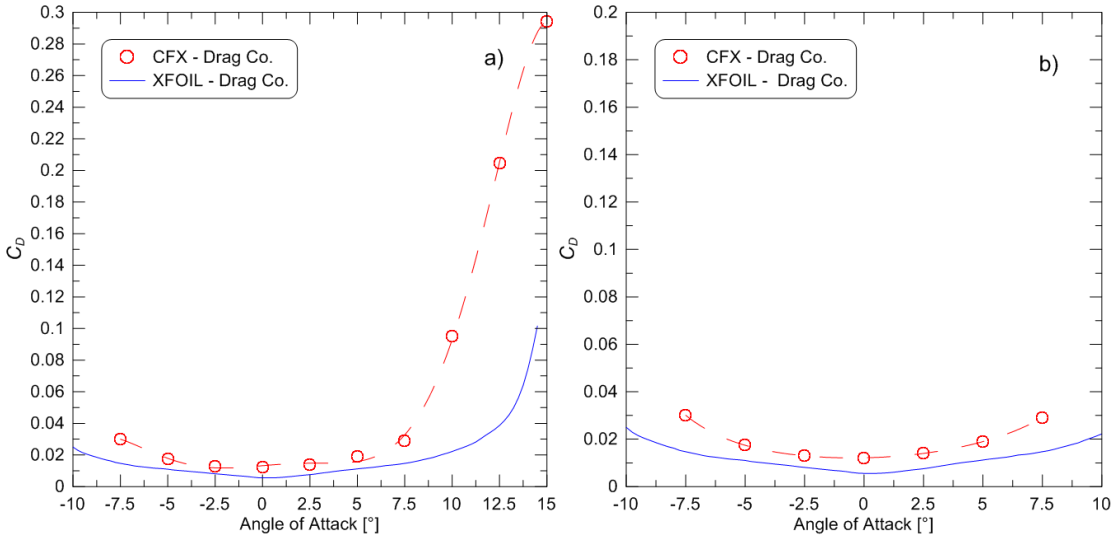

FIGURE 5.2: DRAG COEFFICIENTS: A) FULL RANGE, B) STABLE RANGE

Figure 5.3 shows the streamline result for four angles of attack: 0°, 7.5°, 10°, and 12.5°. The colouring of the streamline represents the fluid velocity. Note that there is a smooth, attached, flow over the blade surface at the lower angles, while separation begins to occur at 10°. This correlates well with the previous results. Indeed, a boundary layer separation is observed in Fig. 5.3c) where a portion of the boundary layer has reversed in direction. This phenomena is well linked to an increase in drag force and reduction in lift.

Flow separation occurs when the boundary layer has moved far enough along an adverse pressure gradient that its relative velocity to the boundary becomes zero. At such a point the flow becomes separated from the wall, replaced by zones of vortices. Low angles of attack, often called feathering for wind and tidal turbines, tend to result in both low drag and lift. Feathering can be desired to reduce thrust loading when the turbine experiences high fluid velocity.

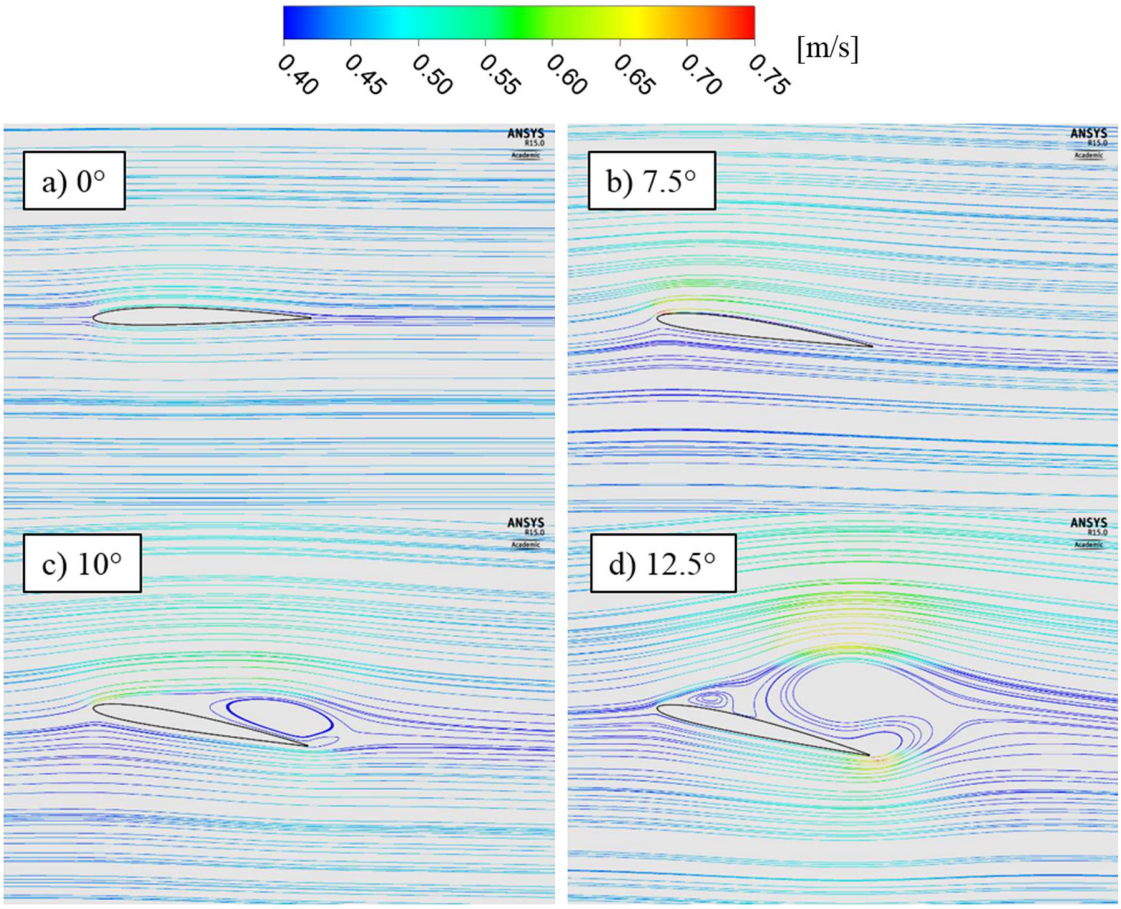

FIGURE 5.3: STREAMLINE RESULT – A) 0°, B) 7.5°, C) 10°, D) 12.5°

5.2. THREE-DIMENSIONAL VALIDATION

Model validation was done by comparison of the turbine performance to experimental data from the University of Southampton (Bahaj *et al.*, 2007a). Figures 5.4a) and b) show experimental and numerical comparisons of C_P and C_T, respectively, as a function of TSR for the 25° hub pitch configuration.

The numerical results follow similar trends but are under-predicted from experimental data. In the TSR range of 3.5 to 8, the predicted C_P curve has an average relative difference of 6.0% with an average absolute difference of 0.023 below experimental values. Similarly, the predicted C_T curve has an average relative difference of 15.8% and an average absolute difference of 0.082. It can be seen that at high TSRs, the experimental power coefficient drops off sharply while the thrust is affected less so. This sharp descent is less pronounced in the numerical results perhaps due to the exclusion of cavitation inception. Guo *et al.*

showed that power capture is greatly affected by cavitation while thrust is less so (Guo *et al.*, 2015). The under-prediction also could be attributed to possible inaccuracies in the geometry and the unknown state of the incoming flow. These results are considered acceptable considering the unknown experimental uncertainty.

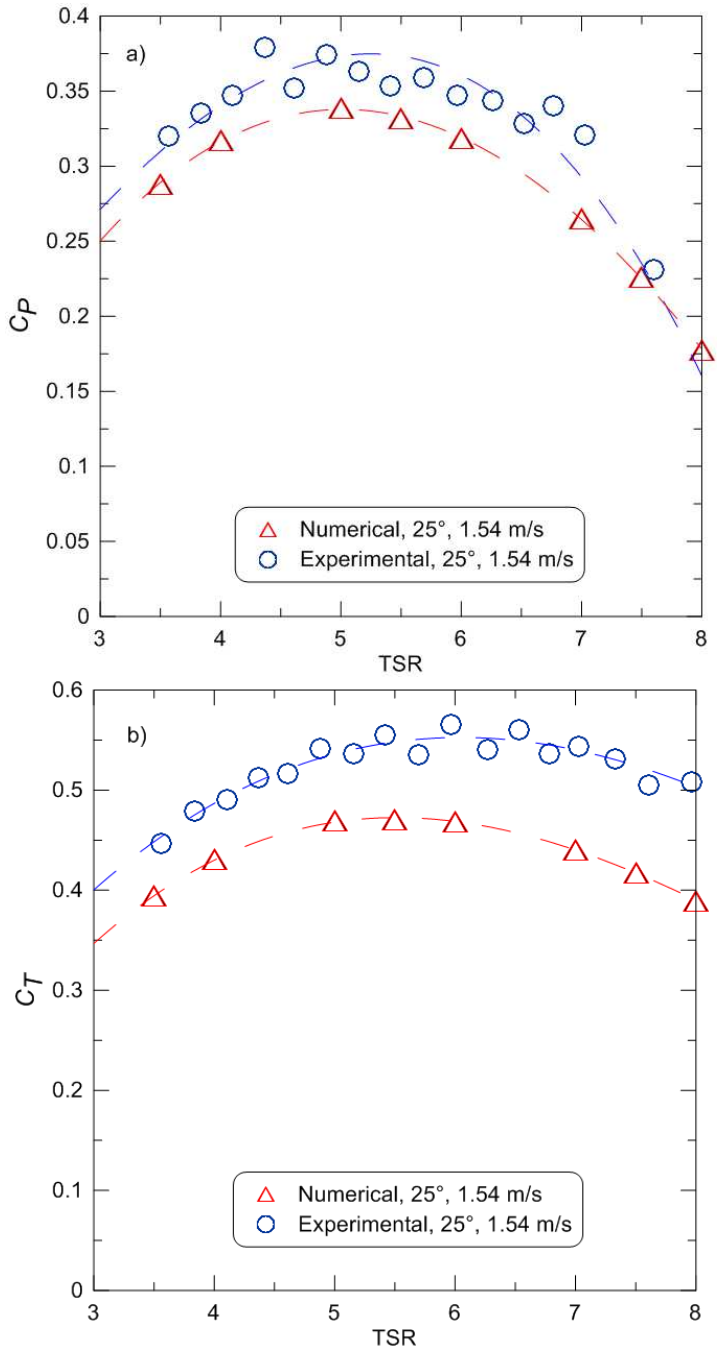

FIGURE 5.4: EXPERIMENTAL AND NUMERICAL COMPARISON – MESH 5, 20D DOMAIN LENGTH: A) C_P AS A FUNCTION OF TSR, B) C_T AS A FUNCTION OF TSR

5.3. BLOCKAGE EFFECT ON TURBINE PERFORMANCE

Presented in Fig. 5.5 is the effect of a blockage correction on the performance of the turbine. In this example the fluid domain cross-section was doubled in size, see Fig. 3.2, reducing the blockage ratio in half from 17% to 8.5%. It was shown that by increasing the domain size the power coefficient and thrust coefficient were reduced on average by 4.25% and 2.86% of the original numerical results, respectively. Likewise, a scenario was completed for a tripled domain size for TSR 6. This resulted in a decrease in power and thrust coefficients by 7.08% and 4.35% of the original results, respectively. These small differences are considered inconsequential for the purposes of this study. For this reason, the majority of the results presented hereafter incorporated a domain cross-section with the original dimensions. However, it was of interest to study the effect of this blockage correction on the wake physics. The results of this are provided and discussed in Section 6.2.1.

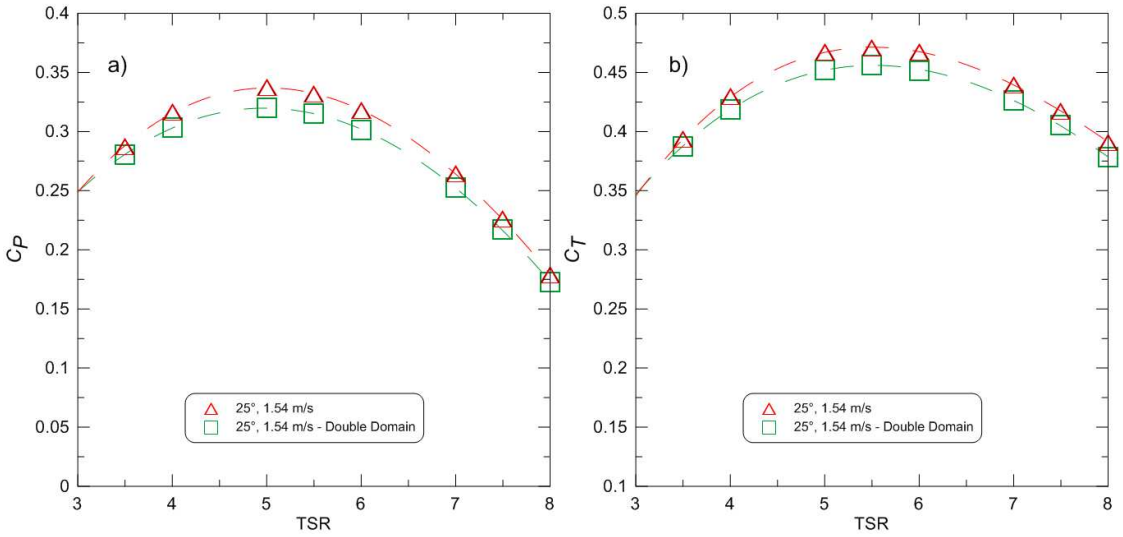

FIGURE 5.5: BLOCKAGE IMPACT ON TURBINE PERFORMANCE: A) C_P AS A FUNCTION OF TSR, B) C_T AS A FUNCTION OF TSR

CHAPTER 6 RESULTS AND DISCUSSION

This chapter presents the numerical results of the wake investigation. Vorticity, turbulence intensity, velocity deficit and normalized velocity are used extensively for analysis. For clarity, presented results henceforth were attained from models using Mesh 5 in the wake with a $20D$ downstream domain length. That is, all results save the turbulence model comparison. Three turbulence models were also employed to analyse their resultant differences in both turbine performance and near wake physics. A $5D$ downstream domain length was employed for this study as turbine performance was the main interest. Finally, the impact of blockage on wake recovery is studied for a variety of tip speed ratios. For this the domain's cross-sectional area was increased, reducing the blockage ratio by half.

6.1. TURBULENCE MODEL COMPARISON

Three turbulence models, ($k-\varepsilon$, $k-\omega$, SST) were compared for the TSR 5 case. All scenarios used a downstream domain length of $5D$ as the impact on the turbine performance and near wake was of key interest. The performance characteristics are provided below in Table 6.1. All models predicted power and thrust coefficients within a small range of one another. It should be noted however that the $k-\varepsilon$ model was highly unstable. All simulations presented in this thesis were carried out for 1000 iterations, while $k-\varepsilon$ experienced a fatal error after 800 iterations. Figure 6.1 provides the output Root-Mean-Square (RMS) values of the momentum and mass conservation equations for the three turbulence model test cases. In this case P-Mass, U-Mom, V-Mom and W-Mom represent the solutions residuals to the continuity equations and three momentum equations. The high degree of divergence in the $k-\varepsilon$ case, and ultimate failure, is likely due to the use of wall functions in the sharp tipped blade mesh region.

TABLE 6.1: C_P AND C_T AS FUNCTIONS OF TURBULENCE MODEL – TSR 5

	C_P	C_T
$k-\varepsilon$	0.357557	0.496195
$k-\omega$	0.346216	0.484925
SST	0.336958	0.467428

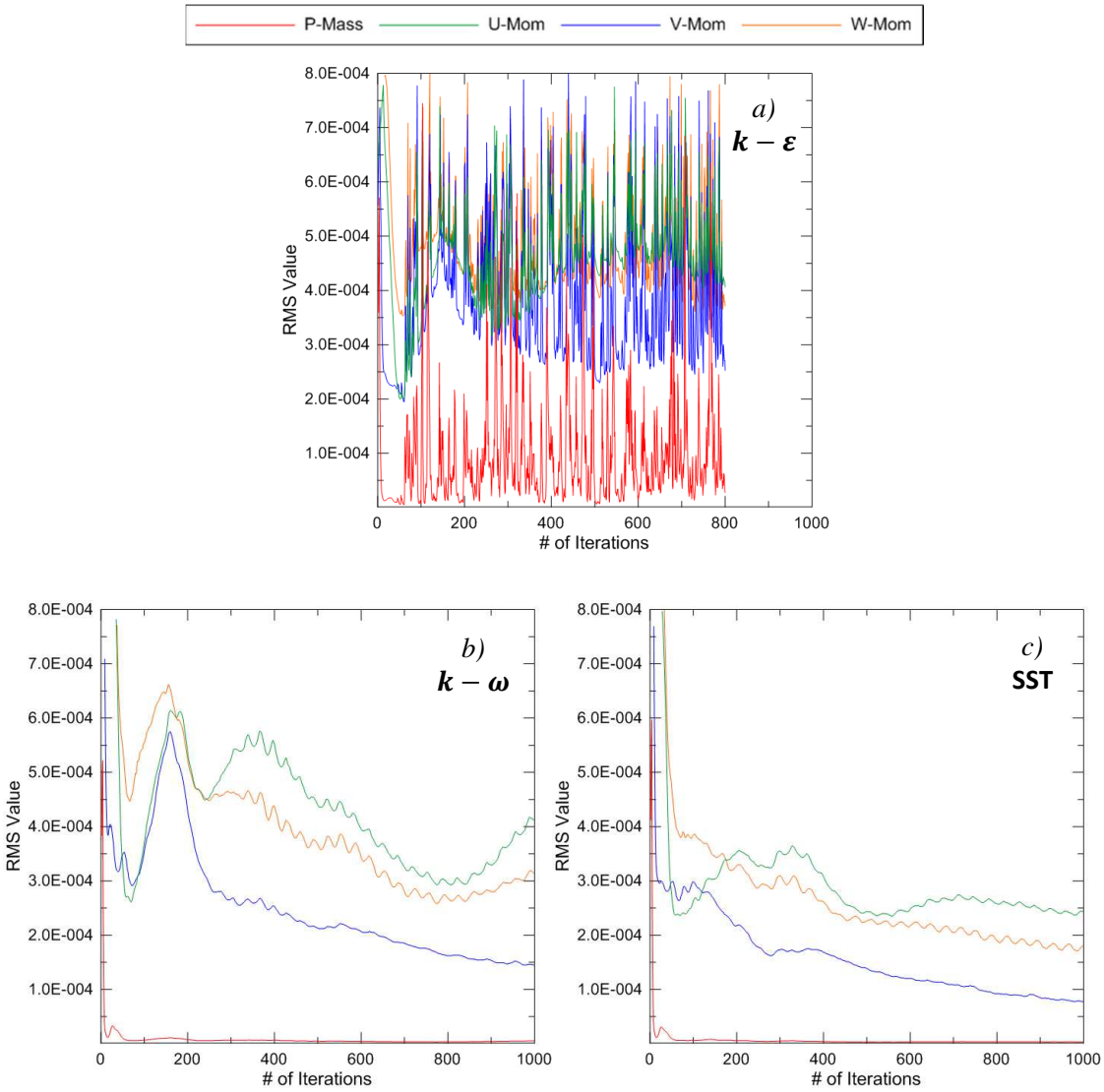

FIGURE 6.1: RMS OF VARIABLES FOR VARYING TURBULENCE MODELS: A) $k-\varepsilon$, B) $k-\omega$, C) SST

Likewise, the determined power coefficient was monitored as a secondary measure of solution convergence. Figure 6.2 illustrates this result for the three turbulence models. The instability of the $k-\varepsilon$ case is exemplified here, demonstrating a high level of solution fluctuation. Both $k-\omega$ and SST are able to quickly converge on one value, roughly by 200 iterations. The reason that SST predicts a lower power coefficient than $k-\omega$ is likely due to slight differences in resolving flow around the blades. For this reason, a review of the near wake for the three models is provided below. It is unfortunate that the

experimental validation data set did not include information pertaining to the wake for comparison.

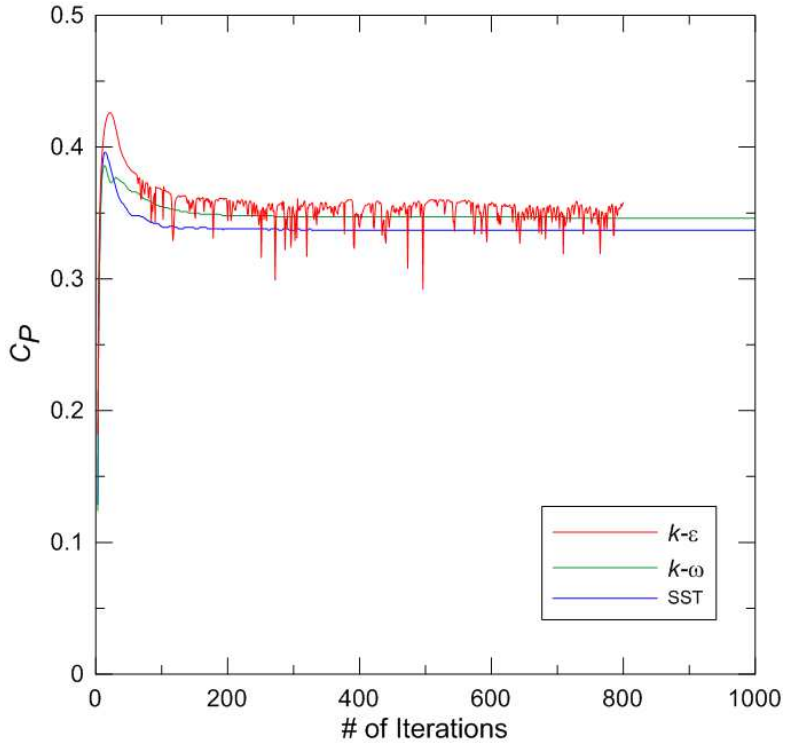

FIGURE 6.2: POWER COEFFICIENT MONITOR

Figure 6.3 depicts the normalized velocity flow-field for the three turbulence model solutions. All cases broadly encompass the same wake physics. The wake partition, as seen above in Section 4.1, is captured for each model, but in slightly different locations. It is expected that had the wall functions of the $k-\varepsilon$ model sufficed, providing a converged solution, the partition location would be similar to that of the SST model as the same modelling technique is used in the wake. Furthermore, the von Kármán vortex street is visible in each case, the most notable with $k-\omega$; This result is expected as $k-\omega$ tends to be highly sensitive in free-shear flows. Finally, Fig. 6.4 presents the centreline solutions of velocity deficit (a) and turbulence intensity (b). Due to its free-shear sensitivity, $k-\omega$ exhibits both the highest deficit and turbulence intensity throughout the domain. The discrepancy between the $k-\varepsilon$ and SST wake solution is attributed to the difference in near wall treatment methodology. It can be seen that the physics near the turbine ($<1D$) is similar for $k-\omega$ and SST as they treat the near-wall region equivalently.

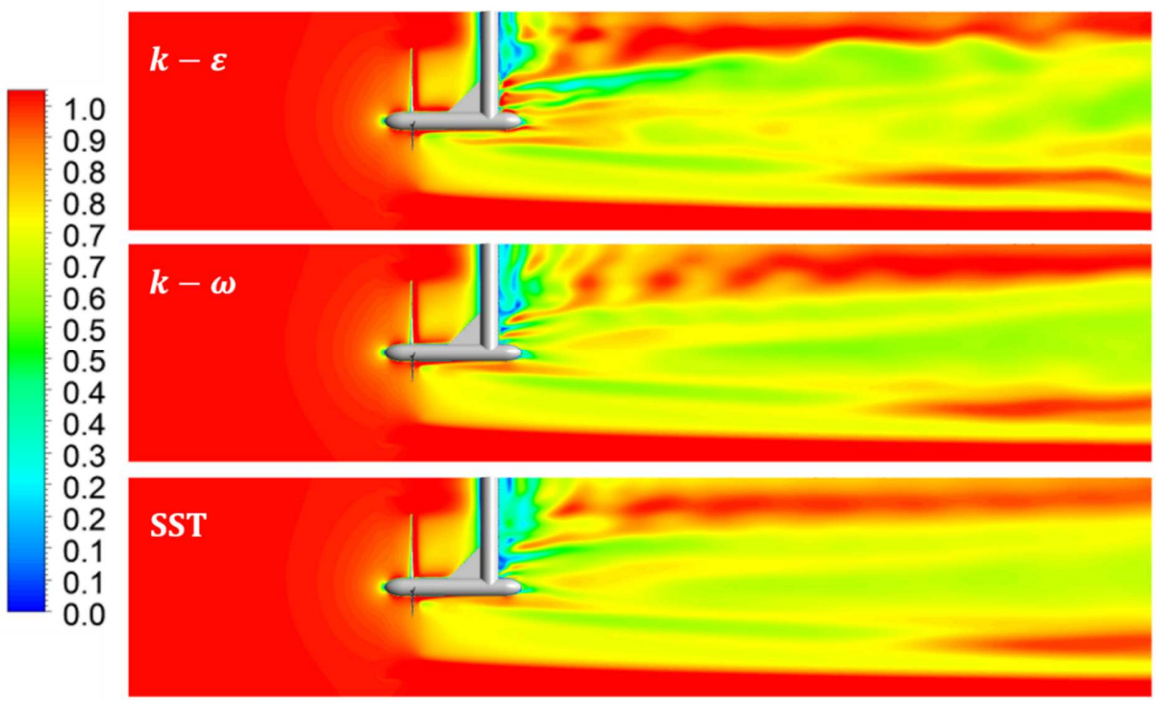

FIGURE 6.3: NORMALIZED VELOCITY V/V_0 ON MID-VERTICAL PLANE FOR THREE TURBULENCE MODELS

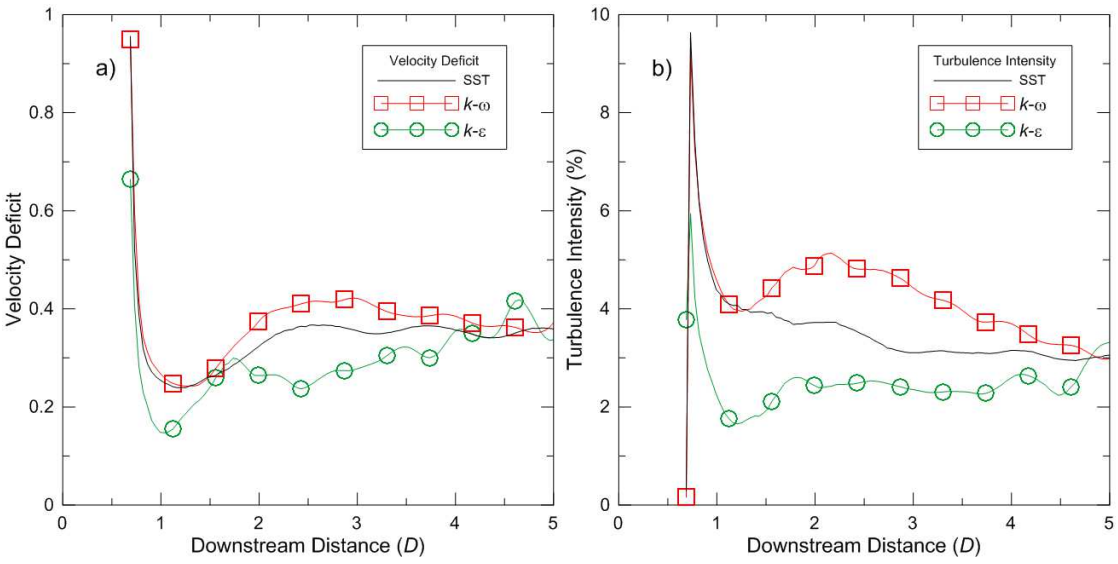

FIGURE 6.4: CENTRELINE SOLUTION: A) VELOCITY DEFICIT, B) TURBULENCE INTENSITY

SST and $k-\omega$ are shown to be superior to $k-\varepsilon$ in this instance as they both not only converge to one value of power coefficient but do so quickly. It is likely that, with a more suitable blade mesh, the $k-\varepsilon$ model solution would converge to a passable estimate. However, wall functions are thought to be insufficient as the near wall treatment at the blade is of utmost importance. Though $k-\omega$ provided a power coefficient closer to the numerical result for TSR 5 the model is known to be overly sensitive in zones of large gradients, *e.g.* the turbine wake. These findings corroborate with current literature, as $k-\varepsilon$ and $k-\omega$, if used at all, are only employed to initialize a more appropriate turbulence model. For these reasons, the shear stress transport turbulence (SST) model was employed in the remainder of simulations.

6.2. WAKE PHYSICS ANALYSIS

This section presents an analysis of the wake propagation, utilizing vorticity contours and line samples, turbulence intensity line samples and normalized velocity contour plots. Additionally, the impact of blockage on the wake is studied.

Figure 6.5 shows normalized velocity at TSR 5 in a shortened section of the $20D$ solution for clarity; Results visualizing the complete $20D$ domain will be provided later in this section. As mentioned above, the turbulent wake from the support structure is evident at the top. Velocity deficits are also notable from both blade tips and blade roots/nacelle. The interaction of upper blade tip wake and support structure is perceptible directly behind the structure in a zone of high turbulence. There is a partition in the wake occurring at roughly $3D$. This result could be due to the mixing nature of the overall rotating wake structure and smaller spiral wake zones stemming from the blade tips. This could also be a result of blockage, as the wake confinement is clear in the figure below. The three stars identify three specific points at the wake edge that will be discussed later.

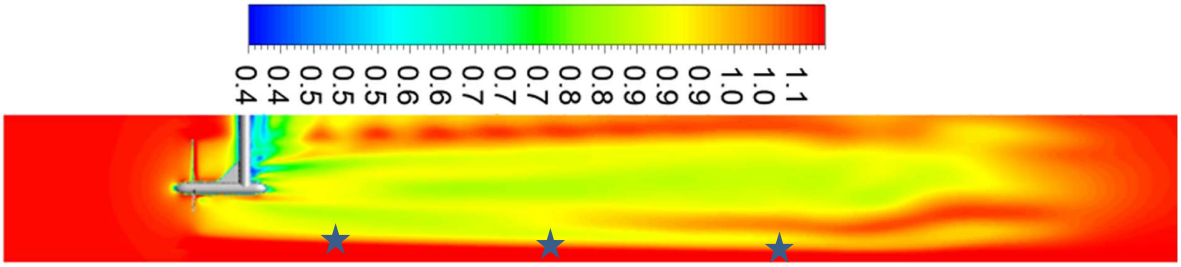

FIGURE 6.5: NORMALIZED VELOCITY V/V_0 ON MID-VERTICAL PLANE FOR TSR 5

Figure 6.7 shows vorticity on horizontal and vertical sample lines at downstream distances ranging from 1*D* to 20*D* downstream of the turbine. Similarly observed in turbulence intensity and velocity deficit in Section 4.1, vorticity shows peaks in the horizontal sample at x/D = 0 and ± 0.5. These peaks correspond to vorticities shed from the blade root and tip, and nacelle structure interaction. Similar peaks are observed in the vertical sample line but is more sporadic as a result of interaction with the support structure. These three peaks are most notable in the near wake (<5*D*) but are still perceptible in some cases as far as 20*D*. This finding would suggest, at least for the current flow scenario and rotor design, that blade root and tip losses perpetuate through and impact the far wake. This has implications into model methodologies for future far wake analysis.

It is readily noticeable from Fig. 6.7 that not all TSR solutions have completely resolved wakes by 20*D*. TSR 4 for example exhibits moderate levels of vorticity by the end of the fluid domain, in both the horizontal and vertical sample lines. It is proposed that three factors affecting the recovery distance are the thrust, blockage and the turbine rotation rate. Thrust is directly related to axial induction factor (a), a fractional decrease in fluid velocity at the turbine, which impacts wake expansion and advection. The relation between the thrust coefficient and axial induction factor is:

$$C_T = 4a(1 - a) \tag{6.1}$$

where

$$a = \frac{V_0 - V_{Turb}}{V_0} \tag{6.2}$$

The expansion and fluid movement of the wake due to a velocity reduction may be impeded by the confinement of the domain. The impact of blockage is studied in Section 6.2.1. Lastly, turbine rotation rates impact swirling effects in the wake, a process which is thought to help break down the wake structure by facilitating the mixture of high and low velocity fluid.

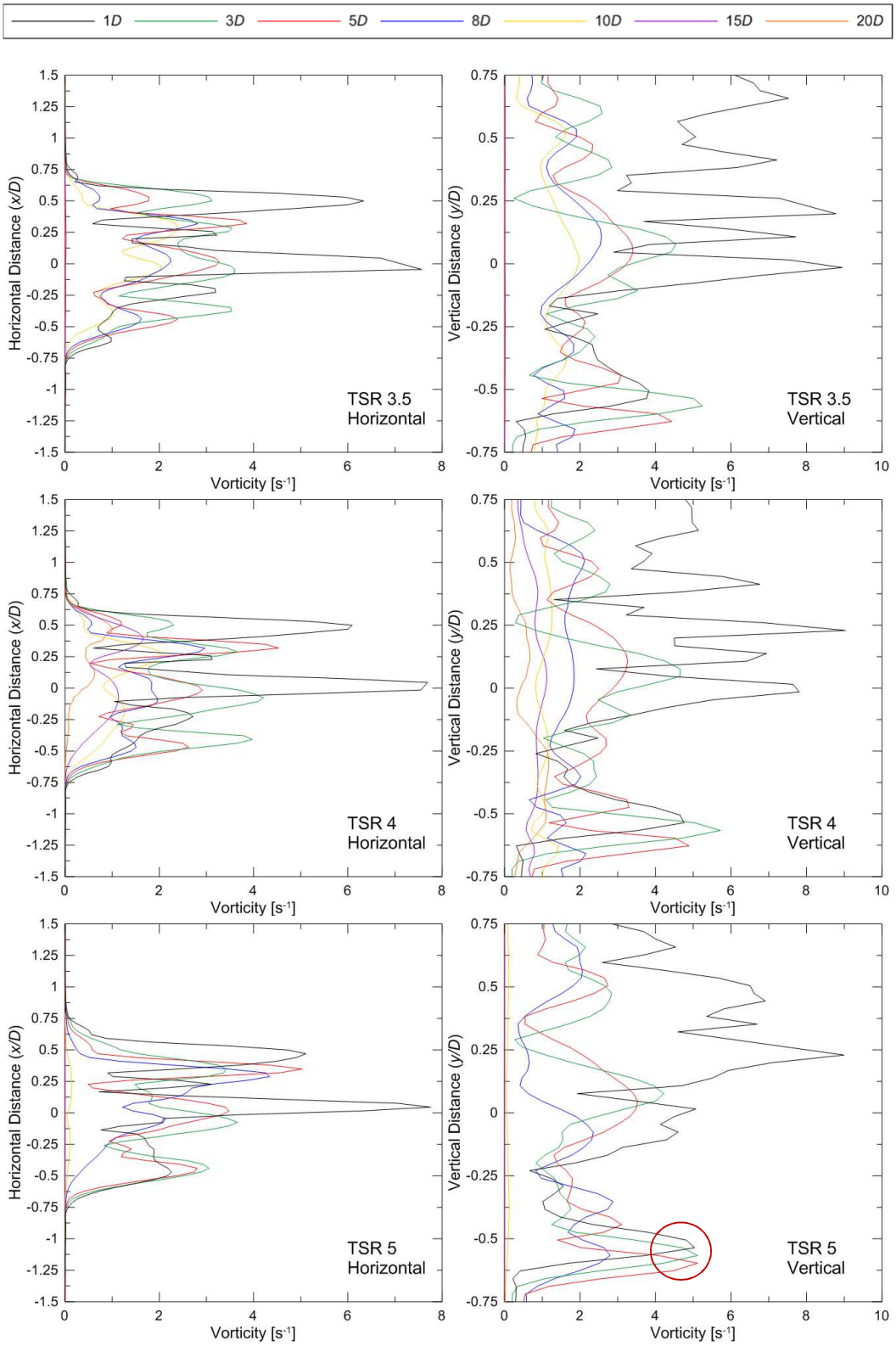

FIGURE 6.6A: HORIZONTAL AND VERTICAL VORTICITY SAMPLES AT VARYING TSRS

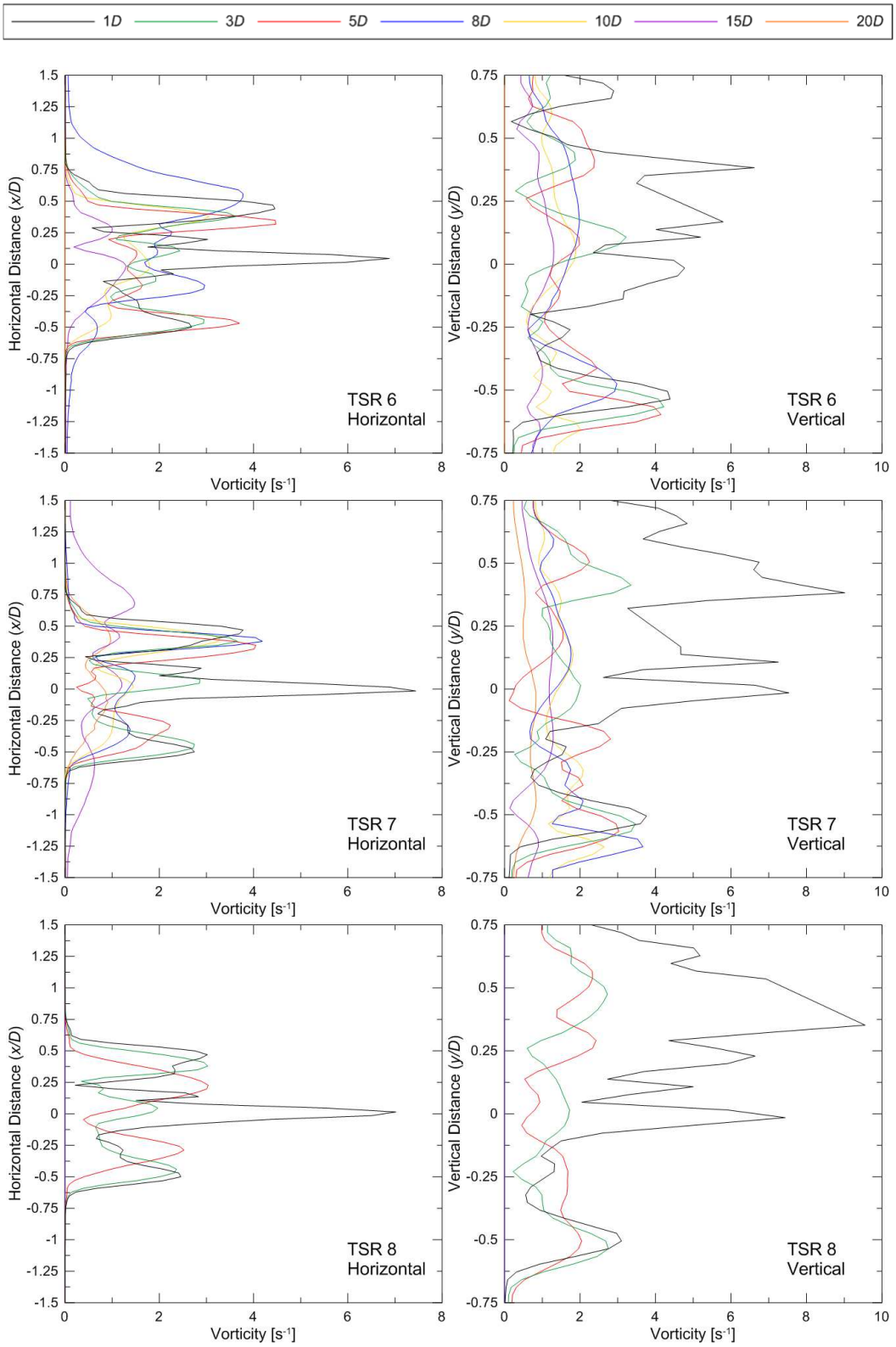

FIGURE 6.7B: HORIZONTAL AND VERTICAL VORTICITY SAMPLES AT VARYING TSRS

One specific peak of the vertical sample at TSR 5, highlighted in Fig. 6.7, corresponds to the wake edge. These locations are pointed out in Fig. 6.5 using blue stars. Values for these three points are given in Table 6.2. This same observation can be made for the $x/D = \pm 0.5$ locations discussed earlier for the horizontal vorticity line. This finding complements the earlier statement of a zone of near wake encapsulation, specifically due to tip shed vortices. This approach could possibly be refined to help characterise the shape and expansion rate of the wake. However, this technique may not be effective or pragmatic due to the complex nature of the dynamic and non-symmetric wake.

TABLE 6.2: PEAK VORTICITIES

	Peak Vorticity [s-1]	Location (y/D)
1D	7.1	-0.536
3D	7.8	-0.597
5D	6.9	-0.628

Figure 6.8 provides cross-sectional contours of vorticity at downstream distances between 1D and 10D for TSR 5. Three distinct zones of impact from the blades are evident in the wake at 1D. These propagate downstream, rotating counter-clockwise (with respect to the images). This rotation, as expected, is counter to the rotation direction of the turbine. The tip of each zone spirals clockwise, acting to draw in faster moving fluid. This entrainment effectively facilitates the mixing of high and low velocity regions, breaking down the wake. There is also a clear disturbance caused by the support structure which interferes with wake propagation. This is noticeable throughout but begins disrupting the wake at 7D, resulting in a complete wake recovery by 10D. Figure 6.9 likewise presents the normalized velocity at these same locations. A roughly circular wake is initially seen, again rotating counter-clockwise. The correlation between vorticity and wake velocity is evident with the three zones of impact, stemming from the blade tips, emerging. Interference from the support structure is again observed, showing a roughly recovered velocity deficit by 10D.

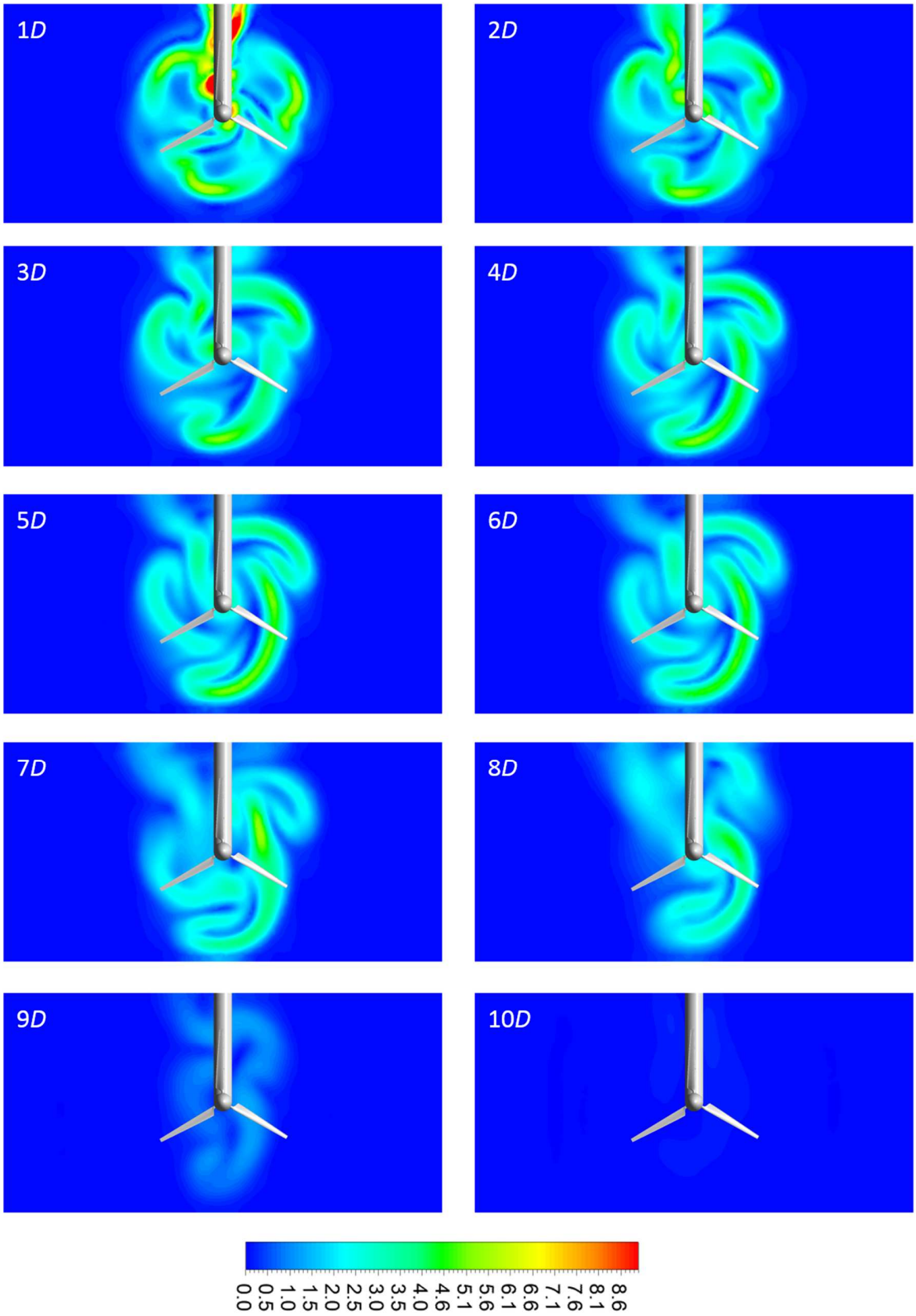

FIGURE 6.8: VORTICITY ON PLANES SITUATED AT 1D THROUGH 10D AT TSR 5

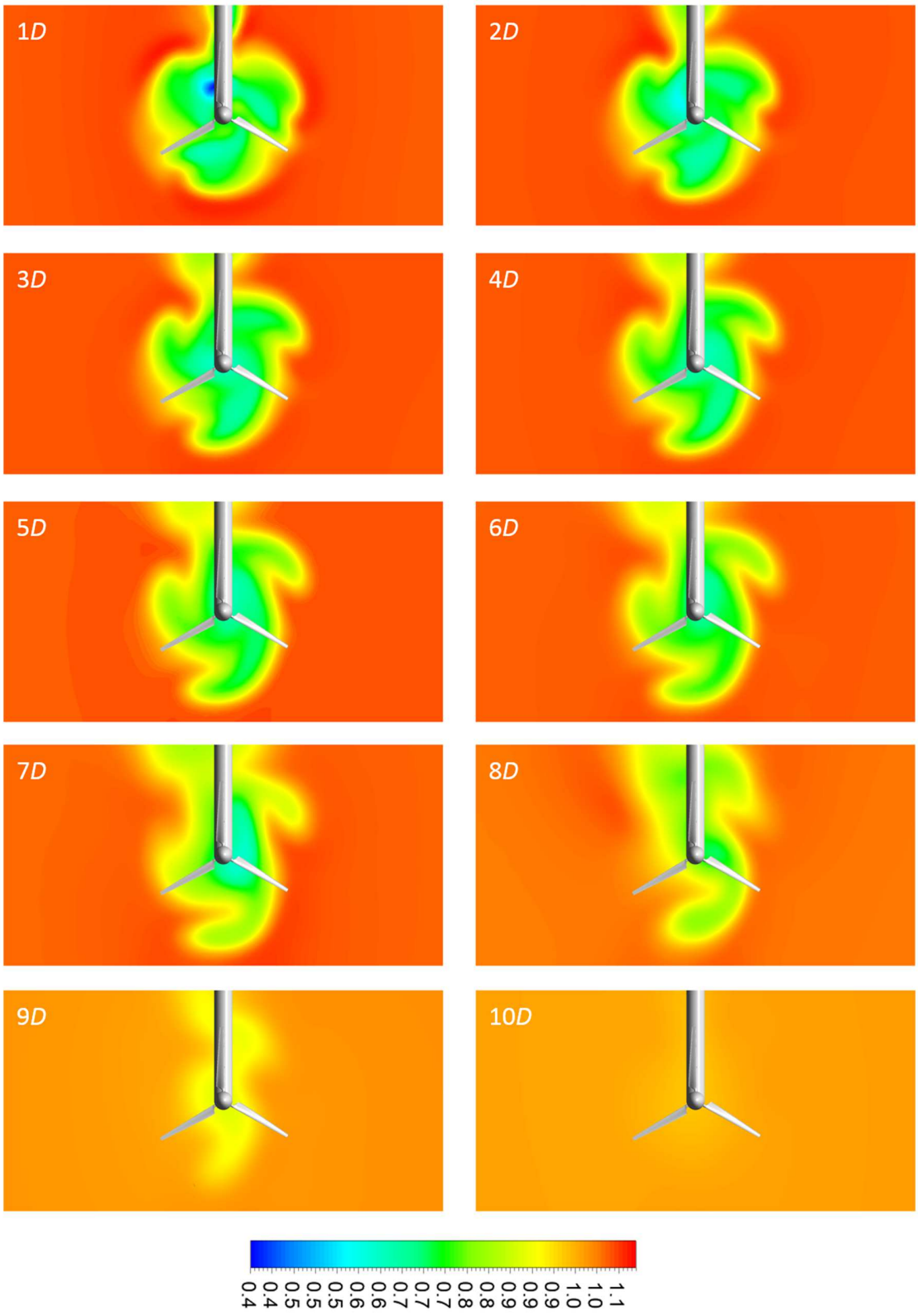

FIGURE 6.9: NORMALIZED VELOCITY V/V_0 ON PLANES SITUATED AT $1D$ THROUGH $10D$ AT TSR 5

Figure 6.1 provides horizontal and vertical velocity deficits throughout the wake for a range of TSRs. Firstly, analyzing the horizontal deficit, the wake tends to be roughly symmetrical about the centre. A few peaks in each is exhibited, as shown before, relating to blade tips and nacelle structure. The higher rotation rates of TSR 6 and 7 experience a shift away from the centre, possibly due to turbulent swirling and wall interaction. Full wake recovery by 20*D* is achieved in some TSRs (3.5, 5, 6, 8) while not in others. This is thought to be due to interaction with the domain walls.

Velocity deficits in the vertical sample lines show similar peaks but with greater fluctuations. This is likely due to flow interaction with the support structure as well as with the top and bottom walls of the domain. Note the proximity of the blade tips (*x/D* or *y/D* = 0.5) to the walls. The vertical depth of the tank is half of its width, likely imparting a blockage effect.

Figure 6.12 presents the centreline solution of velocity deficit and vorticity for a range of TSRs. Each flow scenario begins with a peak in each variable as this measurement is taken in a recirculation pocket directly behind the nacelle. It is clear again that TSRs 3.5, 5 and 8 recover quickly at distances of 14*D*, 10*D* and 6*D*, respectively. TSR 7, expressed as a green line, maintains the largest velocity deficit and vorticity values by 20*D*. It seems that velocity deficit, at least along the centreline, typically follows the peaks and valleys of the experienced vorticity. The genesis contributions of these peaks, *e.g.* wake rotation, spiralling vortices, fluid entrainment and blockage effects, may be too inter-connected to individually discern.

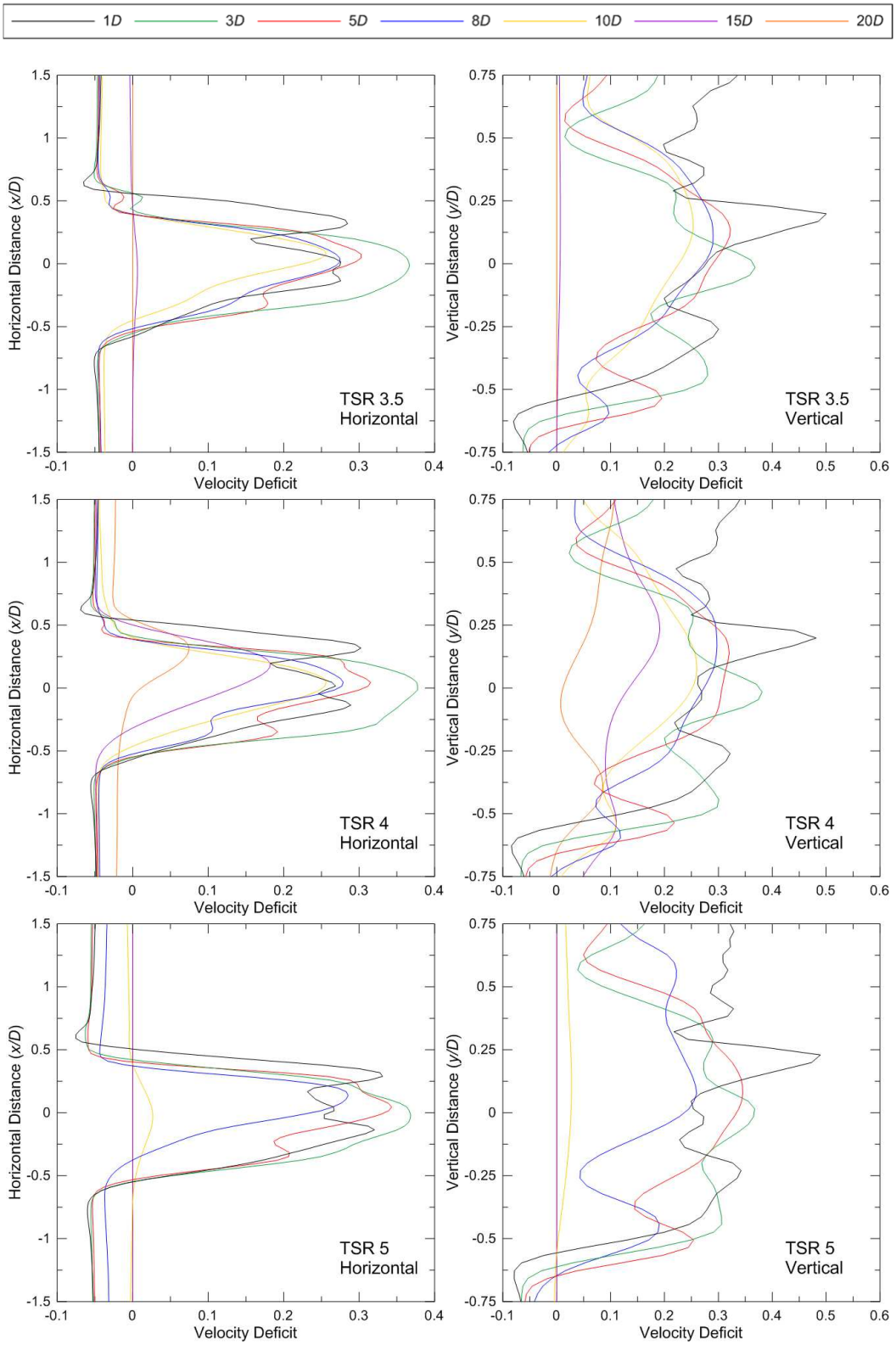

FIGURE 6.10A: HORIZONTAL AND VERTICAL VELOCITY DEFICITS AT VARYING TSRS

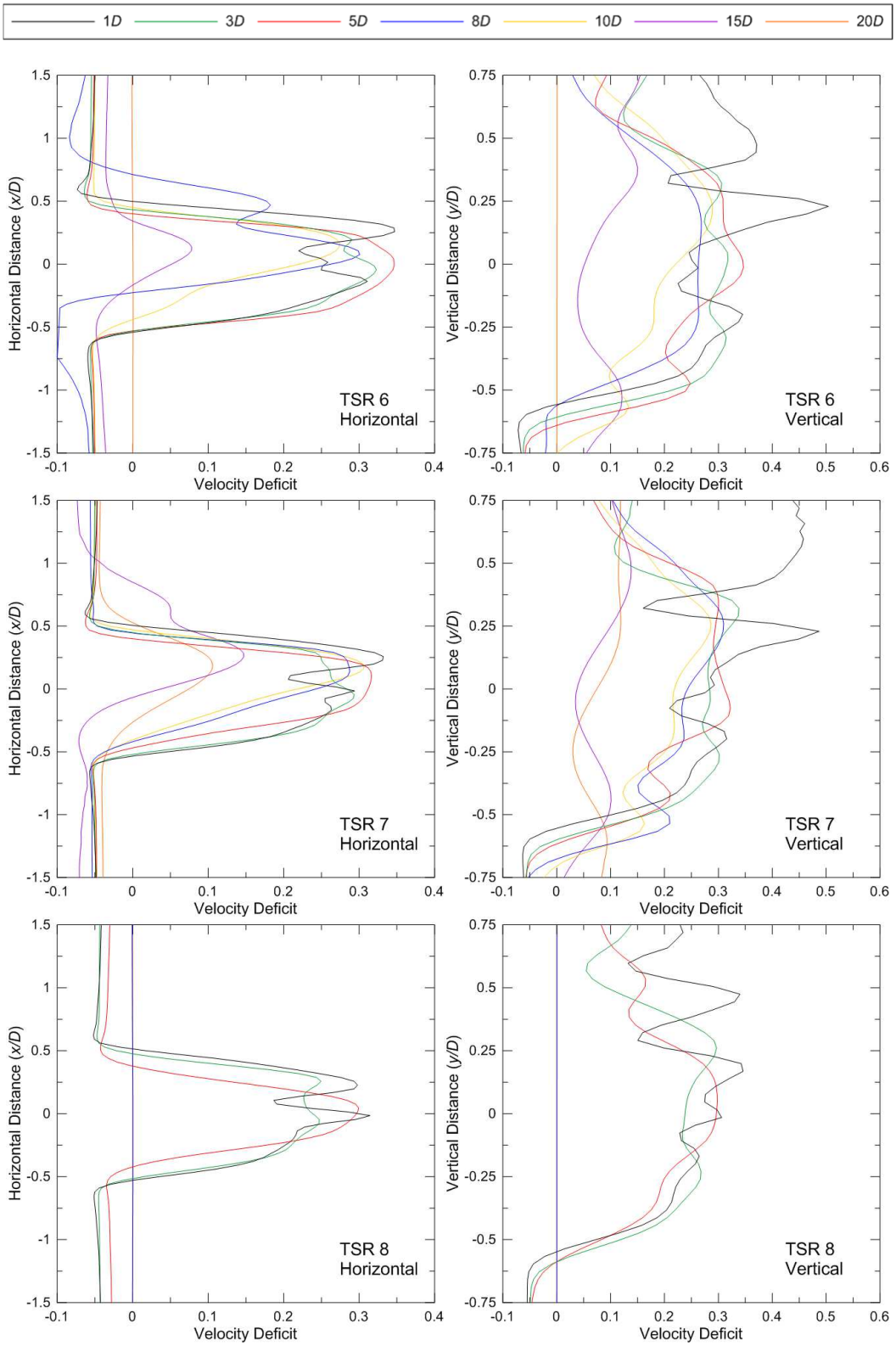

FIGURE 6.11B: HORIZONTAL AND VERTICAL VELOCITY DEFICITS AT VARYING TSRS

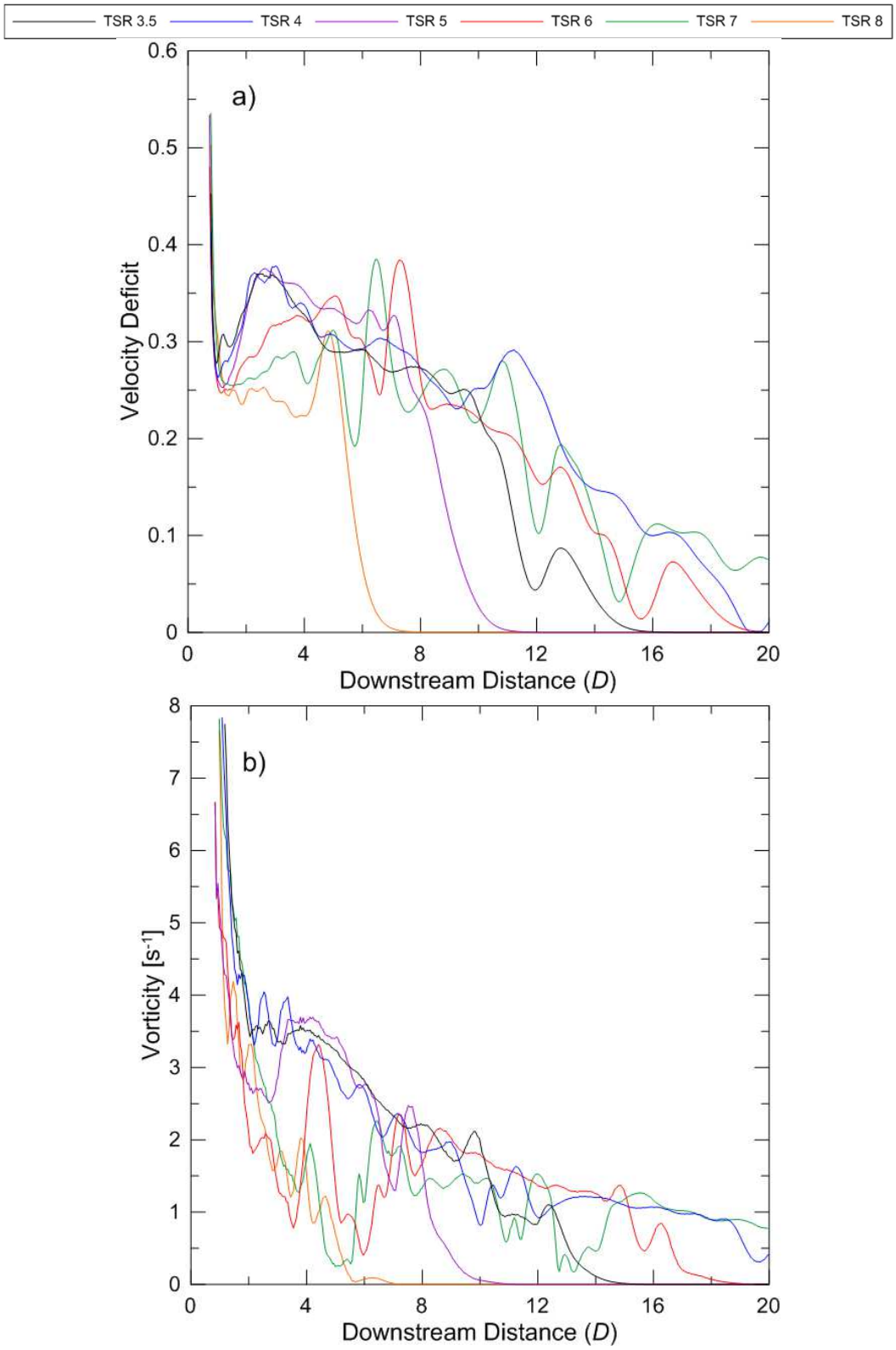

FIGURE 6.12: CENTRELINE RESULTS AT VARYING TSRS: A) VELOCITY DEFICIT, B) VORTICITY

Figure 6.13 provides a view of normalized velocity for varying TSRs with a full view of the 20D domain length. TSRs 3.5, 5 and 8 have noticeably shorter wakes than 4, 6 and 7. A slower wake recovery is expected at low rotation rates as a minimal swirling effect would be imparted on the wake, as well as correlating with minimal thrust. A low thrust load, and axial induction factor, would imply a reduced wake expansion with higher wake velocities to advect downstream. High rotation rates would impart a swirl in the wake, facilitating fluid entrainment, breaking up the wake encapsulation early on.

It is suggested that blockage plays a role in the long recovery distances for TSRs 4, 6 and 7. There is an imaginable trend line in Fig. 6.13 that traces the wake termination points through the various tip speed ratios. TSRs 4, 6 and 7 exhibit turbulent zones at this imaginary line, perhaps due to wake interaction with the wall. Figure 6.15 helps visualize this effect by showing vorticity contours at slices in the wake ranging from 1D to 20D for TSR 7. It is clear that the wake interacts with the wall at the 6D location, causing severe changes to the wake structure. By disrupting the wake, the spiralling zones that draw in fluid are destroyed.

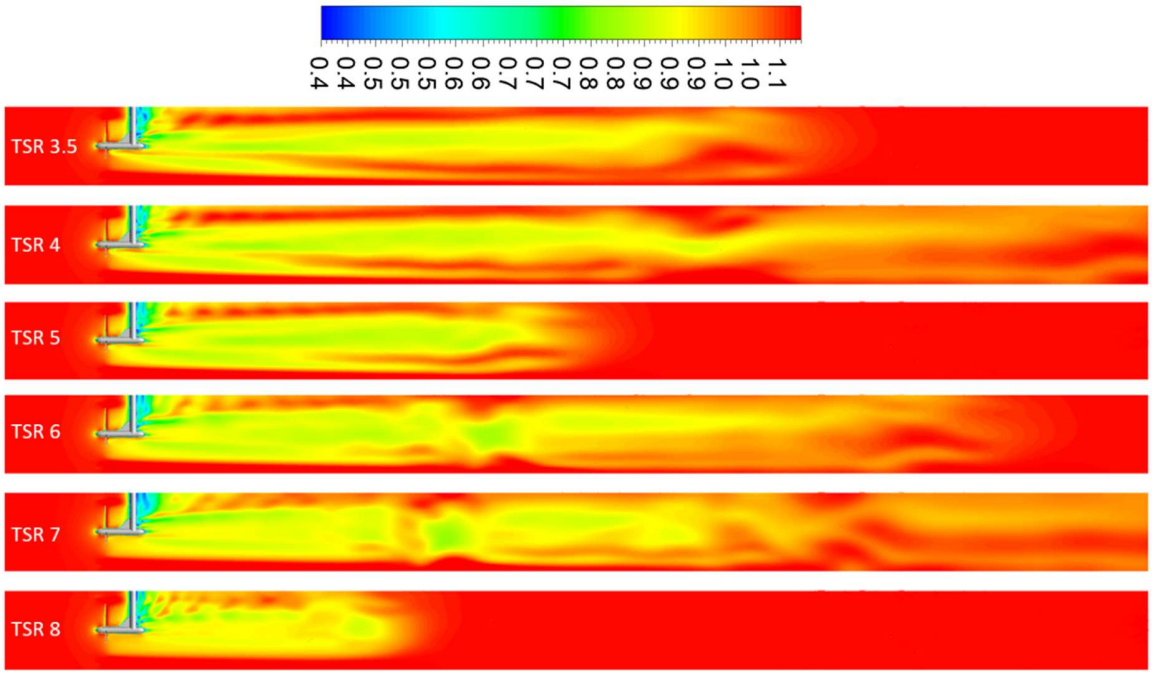

FIGURE 6.13: NORMALIZED VELOCITY V/V_0 ON MID-VERTICAL PLANE FOR VARYING TSRS

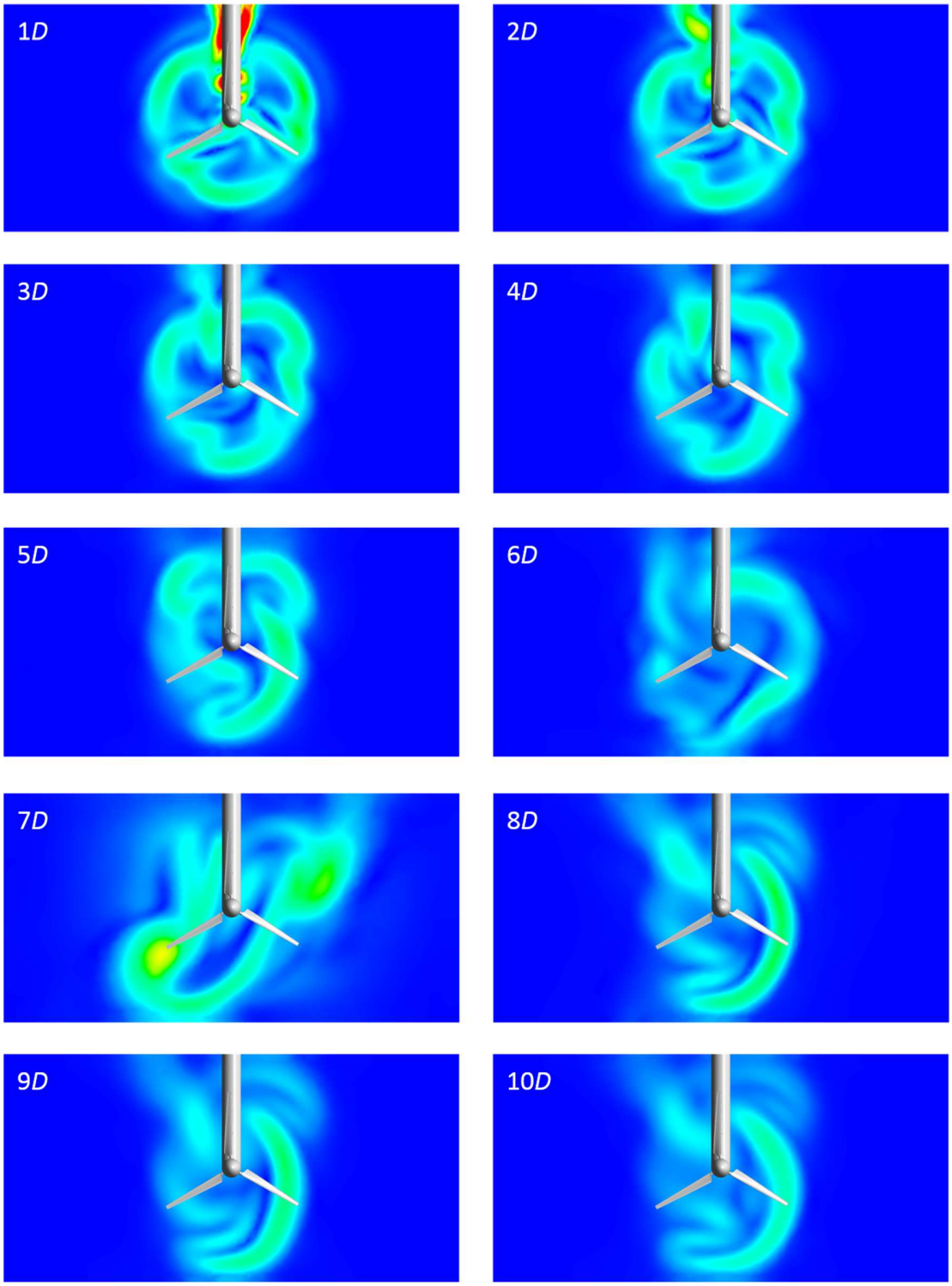

FIGURE 6.14A: VORTICITY ON PLANES SITUATED AT 1*D* THROUGH 20*D* AT TSR 7

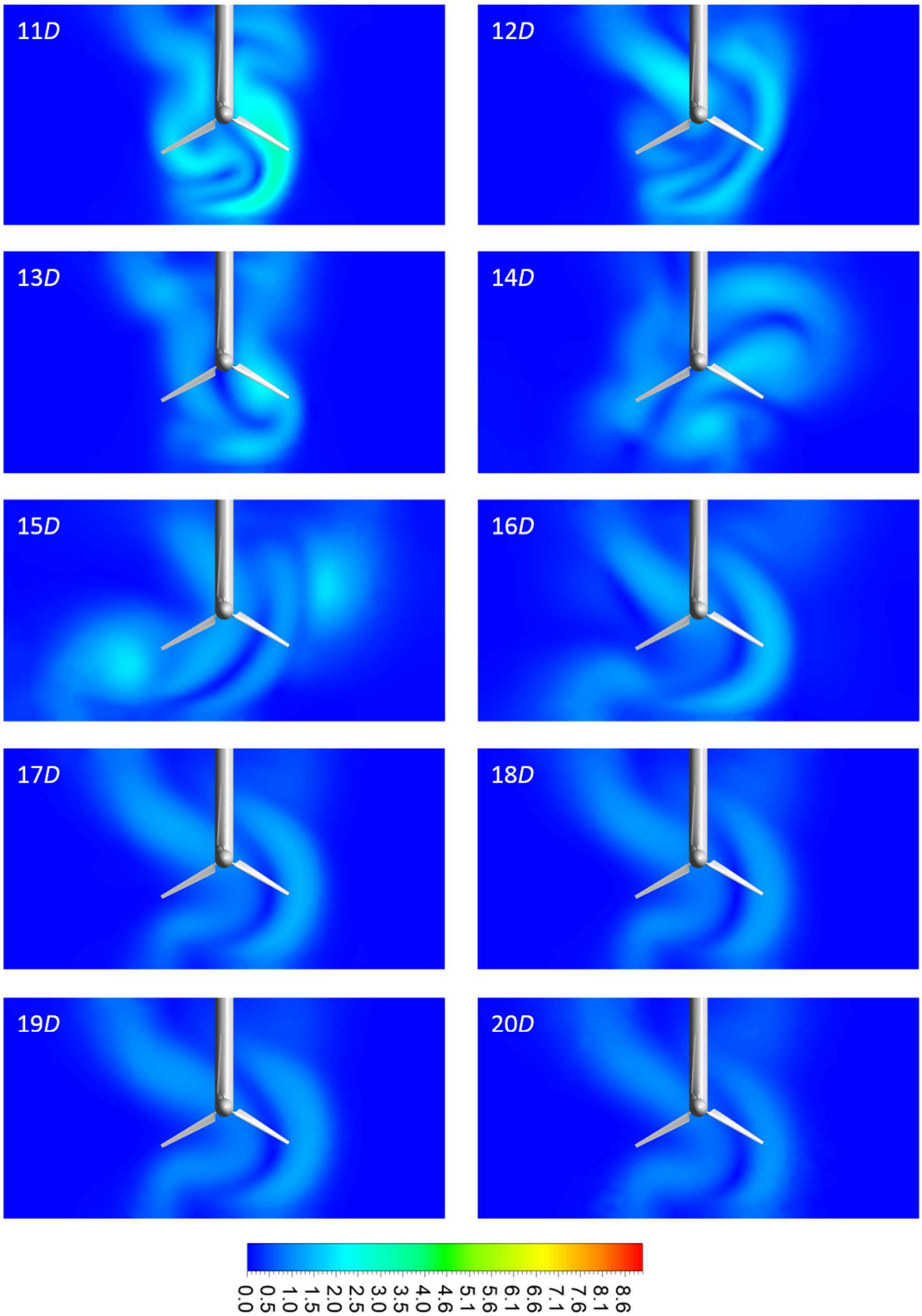

FIGURE 6.15B: VORTICITY ON PLANES SITUATED AT 1*D* THROUGH 20*D* AT TSR 7

6.2.1. BLOCKAGE EFFECTS ON WAKE PHYSICS

Figure 6.16 presents the normalized velocity contour with a doubled domain cross-sectional area. The impact of blockage on wake recovery is clearly discernable. Figure 6.13 showed TSRs 4, 6 and 8 having wakes which extend to near or beyond 20D. It is likely that fluid interaction with the wall impedes rotational and inward movement, focusing flow in the axial direction. This blockage effect would advect the wake downstream while discouraging re-energization. The increased domain size allows for earlier wake recovery for TSRs 4 and 8 as this boundary interaction is not experienced. TSR 6 likely remains to have blockage interactions as this is the point of greatest thrust, refer to Fig. 5.4b). Again, greater expansion is expected at this point.

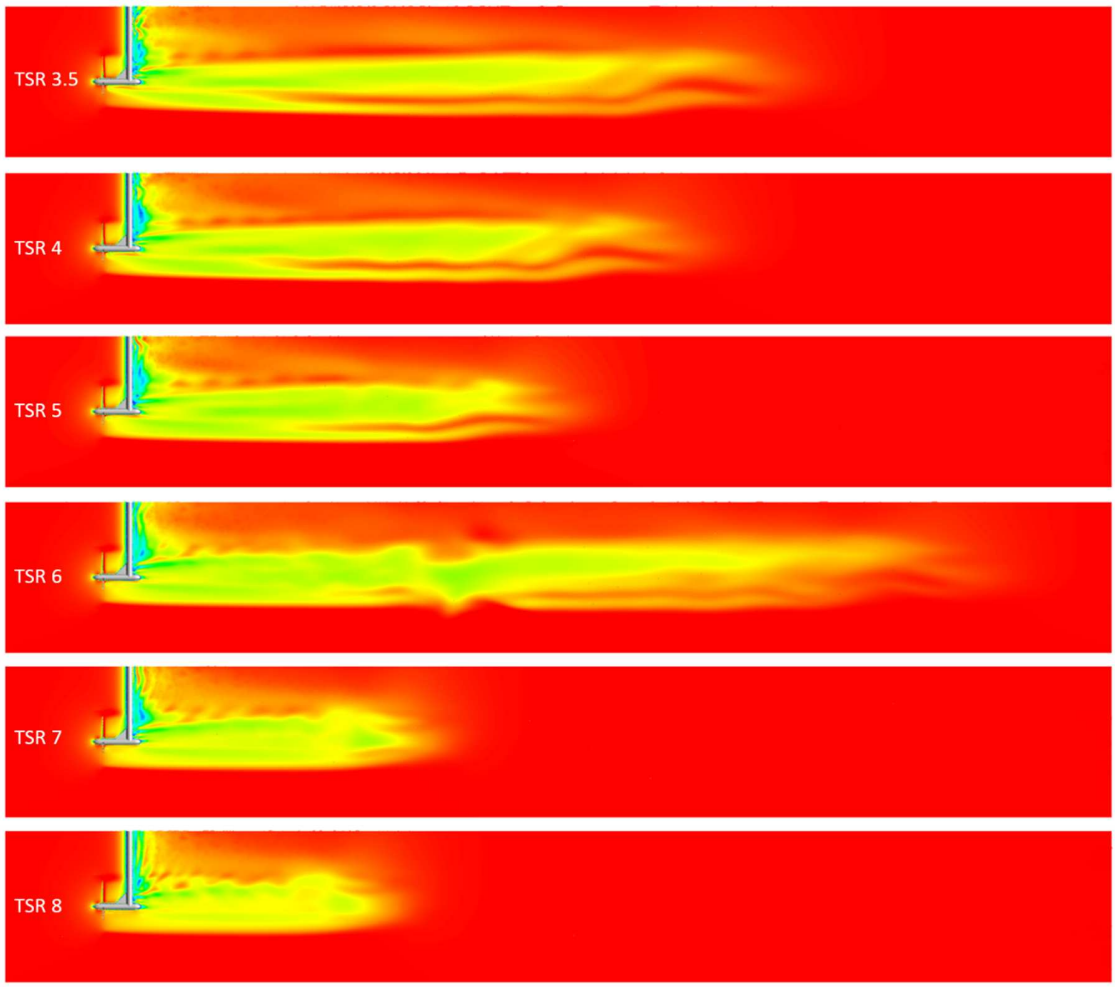

FIGURE 6.16: NORMALIZED VELOCITY V/V_0 ON MID-VERTICAL PLANE FOR VARYING TSRS OF DOUBLE DOMAIN CROSS-SECTION

The TSR 6 solution with a doubled cross-section, seen in Fig. 6.16, still exhibited signs of impact due to blockage. One scenario was completed for TSR 6 wherein a tripled domain cross-section was employed. The normalized velocity for all three TSR 6 solutions are provided in Fig. 6.17. The impact on wake recovery is notable, with a significantly shorter wake recovery distance for the tripled domain.

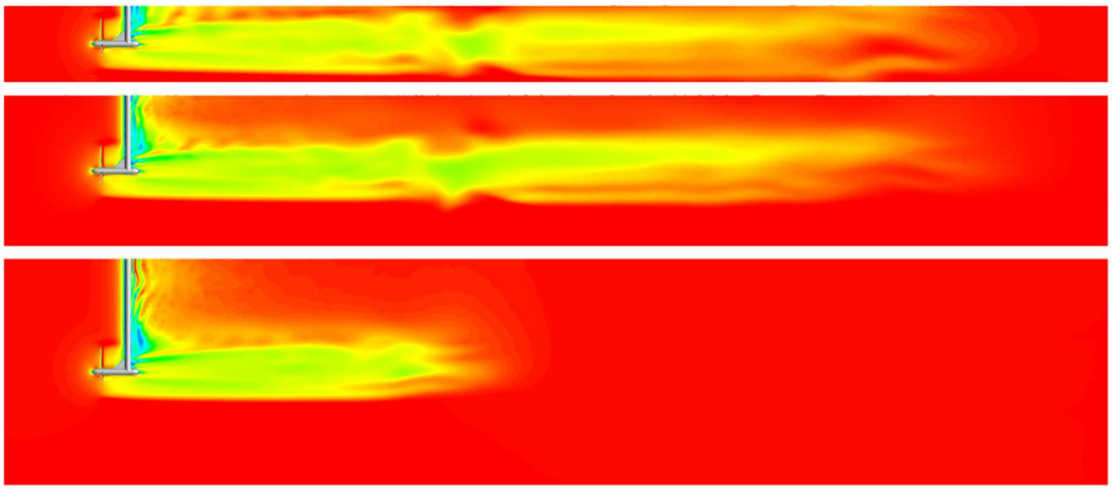

FIGURE 6.17: NORMALIZED VELOCITY V/V_0 ON MID-VERTICAL PLANE FOR TSR 6 WITH ORIGINAL, DOUBLED AND TRIPLED CROSS-SECTION DOMAIN

Figure 6.19 provides the original, and blockage corrected, centreline results of turbulence intensity, velocity deficit and vorticity. The TSR 6 results include that of both the doubled and tripled cross-section domains. Vorticity shows little effect of blockage, save for TSR 4 and 7. In these scenarios, flow interaction with the wall caused an increase in centreline vorticity. Vorticity spikes in the confined domain tend to correlate with turbulence intensity.

One observation is that velocity deficit tends to gradually decrease, roughly linearly, at low TSRs. High TSRs exhibit a gradual initial decrease in velocity deficit, follow by a peak and a sharp descent. It is likely that fluid entrainment with high wake swirl, coupled with nacelle interference, is the cause of this peak and abrupt wake degradation. Earlier it was postulated that flow interaction with the walls impedes wake rotation and flow entrainment. Note the distinguishable impact of the blockage correction for TSRs 4 and 7, particularly in turbulence intensity. A wake with minimal rotation and impeded flow entrainment would then be expected to advect further downstream with a more gradual wake recovery.

Indeed, the velocity deficits for TSR 4 and 7, of the original domain, exhibit a steadier trend to wake recovery. A similar observation is made for TSR 6. The velocity deficit for the original and doubled domain experience a gradual decrease, whereas the tripled domain experiences a rapid recovery around 8*D* downstream.

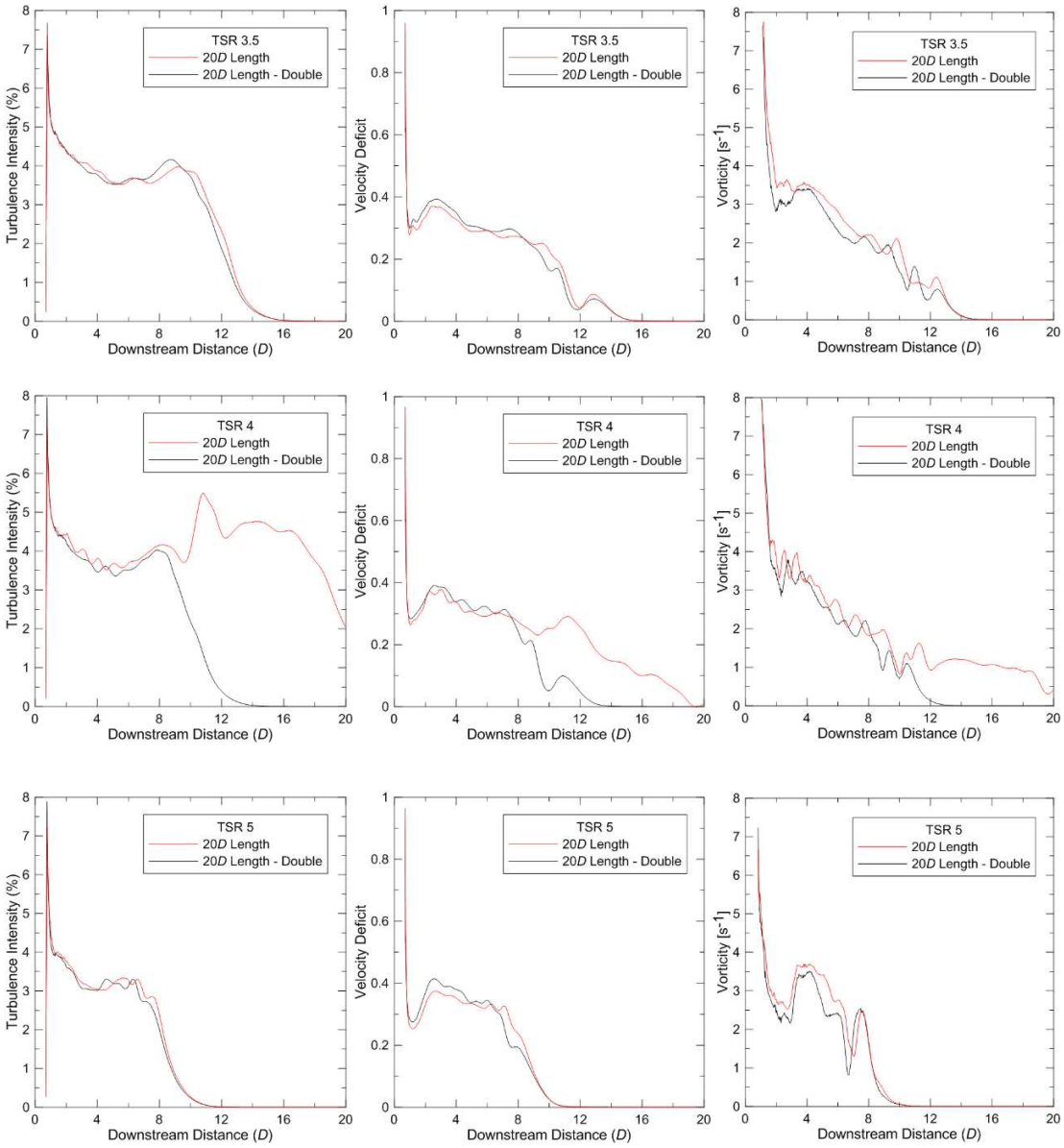

FIGURE 6.18A: BLOCKAGE EFFECT ON TURBULENCE INTENSITY, VELOCITY DEFICIT AND VORTICITY FOR A RANGE OF TSRS

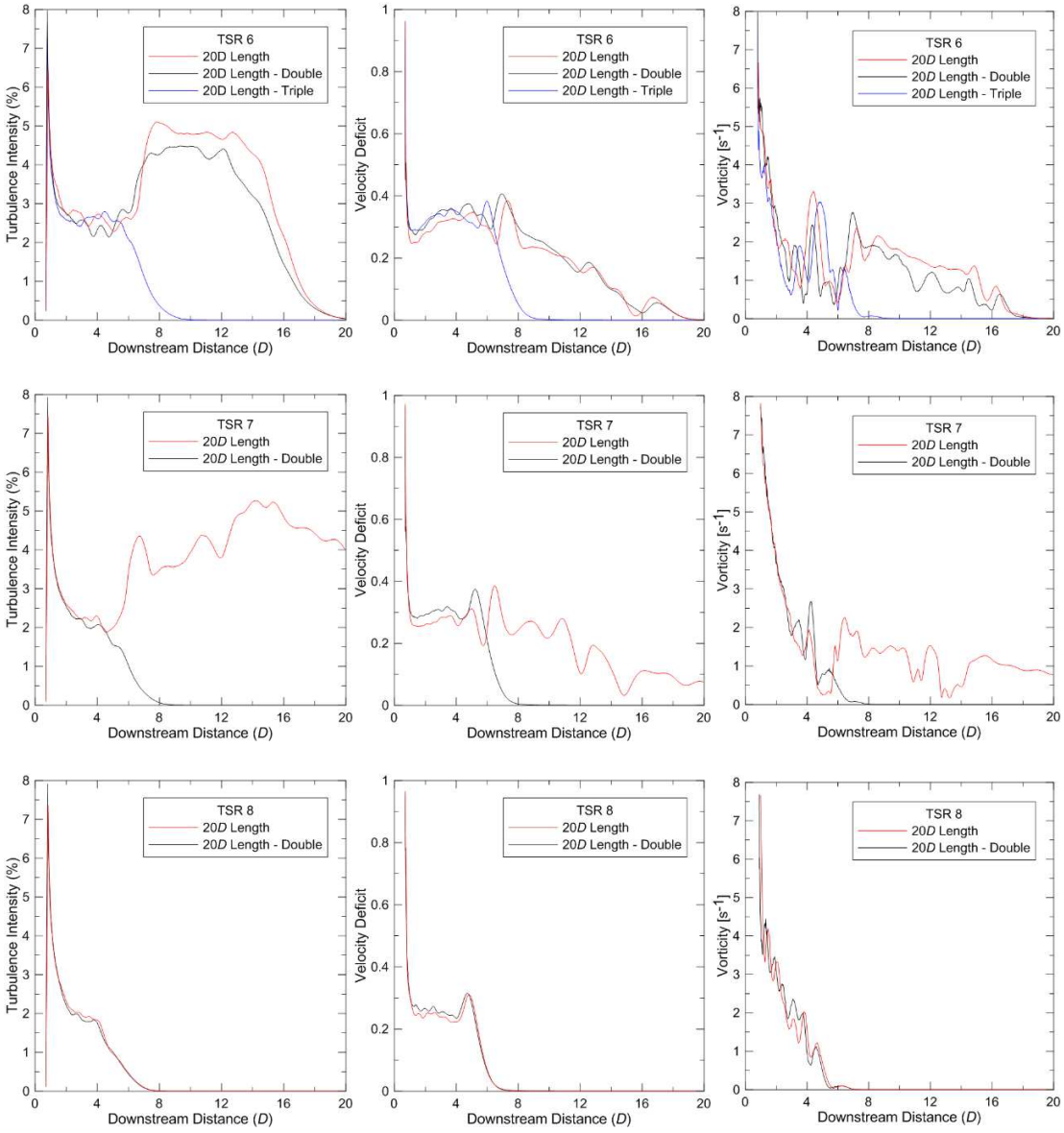

FIGURE 6.19B: BLOCKAGE EFFECT ON TURBULENCE INTENSITY, VELOCITY DEFICIT AND VORTICITY FOR A RANGE OF TSRS

Finally, the wake termination position along the centreline was determined to relate wake recovery distances to TSR and wake swirl, indirectly. The position of wake termination, for the purposes of this analysis, was defined as the centreline position in the wake that first recovers to 99% of the free-stream velocity. Table 6.3 provides the values of the wake recovery distances while Fig. 6.20 visualizes them. There is an apparent correlation between turbine rotation speed and wake recovery distance. This finding implies, and strengthens, the thought that wake swirl is a major contributor to wake recovery. This

analysis should only be considered preliminary however as many others factors contribute to wake recovery. Subsequent studies would need be completed wherein ambient turbulence intensity, freestream velocity and turbine design are considered factors of wake recovery distance.

TABLE 6.3: WAKE RECOVERY DISTANCE

TSR	Downstream Distance (*D*)
3.5	14.78
4	12.96
5	10.45
5.5	9.54
6	8.83
7	7.65
7.5	7.18
8	6.80

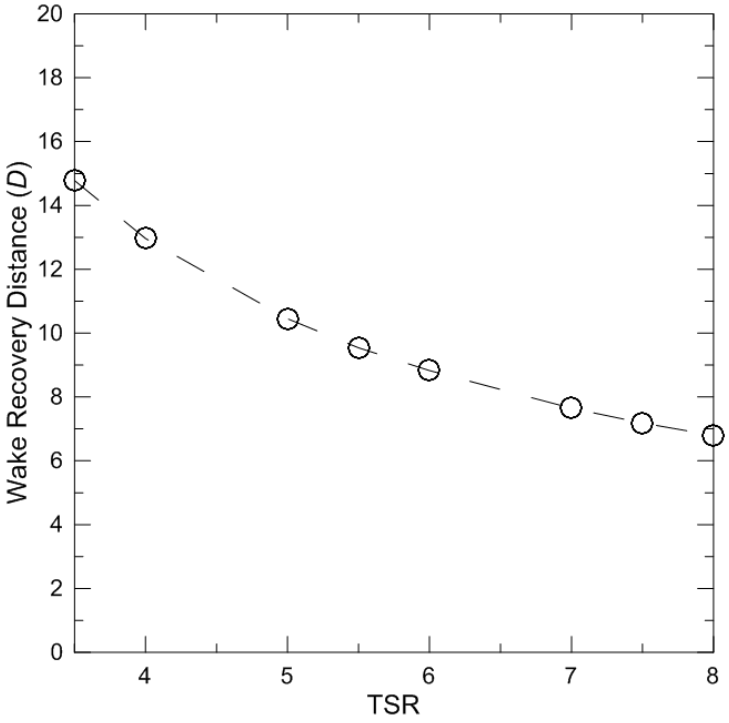

FIGURE 6.20: WAKE RECOVERY DISTANCE

CHAPTER 7 CONCLUSIONS AND FUTURE WORK

7.1. SUMMARY OF WORK DONE

A three-dimensional CFD model of a three bladed horizontal axis tidal turbine was successfully created. The effect of physical parameters, such as twist axis location and blade trailing edge roundness, on the solution were discussed. It was found that locating the blade twist axis away from the leading edge had a significant impact on the power coefficient. Lift tended to be rather independent of twist axis locations beyond 10% of the blade chord. A trailing edge roundness study was done, using a 5 mm thick blade section, in which it was shown that power coefficient is greatly dependent on this variable. For these reasons, all results provided in this study incorporated a blade twist axis at 25% of the chord and a sharp trailing edge.

A wake mesh convergence study was completed by adjusting the mesh density within a cylindrical body of influence situated behind the turbine. Six meshes were studied wherein the local maximum cell size was adjusted. This study showed minimal impact on power and thrust coefficients; a positive result for turbine designers looking to optimize blade design without emphasis on wake mesh density. However, coarse meshes were unable to resolve the oscillating flow behind the support structure. This cyclical flow can cause physical fatigue so structure designers may want to include some emphasis on near wake refinement.

However, the coarser meshes provided insufficient detail for wake analyses. Velocity deficit and turbulence intensity were used as metrics to determine the convergence of wake physics. Meshes 5 and 6, the two finest, agreed in velocity deficit capture while some small differences in turbulence intensity were still observed. Mesh 5 was chosen for the remainder of the simulations as it provides adequate detail while limiting computational effort.

Mesh 5 had a maximum velocity deficit of 0.36 and maximum turbulence intensity of 4.0% at 5D. This result proves that a numerical downstream distance of 5D is insufficient for

complete wake recovery capture. This finding lead to a domain length sensitivity study. Downstream domain lengths of $5D$, $10D$, $20D$ and $30D$ were studied for their impact of turbine performance as well as wake evolution. Differences in power and thrust coefficients were insignificant with less than 0.5% difference in most cases. For TSR 5 it seemed that wake recovery took place within $12D$ of the turbine. Therefore, a $20D$ domain length was chosen for the remainder of the simulation.

A quick two-dimensional study was completed using the approach to be taken for the three-dimensional model. Results of this study were compared to a theoretical inviscid model with reasonable agreement until high angles of attack. Likewise, the three-dimensional results were compared to experimental tests. Power and thrust coefficients were compared for TSRs 3.5 to 8 with relatively good agreement. C_P was found to be under-predicted by 5.3% and C_T by 16.1%. It is suggested that this under-prediction, especially of C_T at high TSRs, is attributed to the occurrence of cavitation in the experimental study. Additionally, as limited detail was provided, possible difference in geometry could contribute to the discrepancy.

Three turbulence models, $k-\varepsilon$, $k-\omega$ and SST, were compared for their solution differences of turbine performance and near wake physics. For this, a downstream domain length of $5D$ was chosen and only TSR 5 was computed. The power coefficient and a monitor of the equation residuals were considered for convergence. $k-\varepsilon$ experienced a fatal error and did not finish its computation. This is likely due to its use of wall functions in the sharp tipped blade mesh region. $k-\omega$ provided a value of power coefficient closest to the expected value. However, this model is known to be inadequate in free shear flows with high gradients, *e.g.* the turbine wake. SST, a blend of these two models, was chosen for all other simulations.

Vorticity, turbulence intensity and normalized velocity were used to study the wake flow. A rotating wake could be visualized using contour plots at multiple downstream distance. Three spiralling zones, stemming from the blade tips, were evident at the wake edge. These effectively drew faster flowing water into the wake, facilitating the re-energization of the fluid. However, it was also evident that the wake expansion and advection was being

influenced by a blockage effect. A domain with double the original cross-sectional area was employed to quantify this effect. As expected, the power and thrust coefficients reduced by 4.85% and 2.86% of the original numerical results, respectively. The impact of blockage on wake recovery was significant, particularly for TSRs 4, 6 and 7. It is thought that the fluid entrainment was ceased upon wake impact with the walls as this broke up the wake structure. This effect was shown visually, again using contours of cross-sectional slices in the wake. Blockage would then allow the wake to be advected further downstream and the fluid entrainment would cease. Centreline velocity deficits exhibited an initial gradual decrease followed by a spike and a sharp decline. However, solutions which were impacted by blockage generally experienced a gradual wake recovery without this sharp decline. This finding further strengthens the importance of flow entrainment for wake recovery.

The TSR 6 wake solution stilled showed effects of blockage with the doubled domain. This case, with maximum thrust, would be expected to have the greatest wake expansion. For this reason, solely for this flow scenario, a tripled domain cross-section was employed. This study significantly reduced the wake recovery distance and any impact with the wall.

Lastly, a preliminary correlation between tip speed ratio and wake recovery distance was found, exhibiting a fairly smooth relation. Factors such as ambient turbulence intensity, freestream velocity and turbine design are also significant for wake recovery. Further studies incorporating these variables could help deduce their level of impact.

7.2. RECOMMENDATIONS FOR FUTURE STUDIES

This study employed the frozen rotor model, specific to ANSYS CFX, which is a quasi-steady state approach. A fully transient model should be the next focus as the impact of wake swirl, specifically tip shed vortices, was shown to be significant for wake recovery. The work in this thesis cannot reveal any discrepancies it may have to a transient model, if any exist.

A transient model would also allow for a changing inlet condition. This would be beneficial as real world data could be fed in, *e.g.* flow conditions from the Bay of Fundy. However, the model's complexity would quickly increase. Currently, with a steady inflow

speed, the turbine rotation rate is set manually to achieve a desired TSR. A continuously adjusting inlet condition would require the user to either base the rotation rate on the dynamic upstream velocity or to have a reactionary turbine which rotates as a response to the flow.

It is recommended that experimental results with wake data be used for future model validation. This would give greater confidence in the model results and perhaps provide information into areas that require refinement. Additionally, some metric of the wake solution should be used as a convergence criterion if wake analysis is a focus. In terms of model continuation, the following approaches should be considered:

- Many researchers employ an actuator disk method and assert that the resolved far wake achieves adequate comparison to an explicit turbine. A comparative analysis of these two methods would help strengthen this assertion or determine any inadequacies.

- A more advanced model, *e.g.* detached eddy simulation (DES), would provide greater detail into wake flow and recovery. DES behaves as a hybrid RANS-LES model, resolving a fine level of detail in the wake while overcoming the deficiencies of LES at solid boundaries.

- This last recommendation would require attention to improve the mesh quality around the blade. For this, either a blade with a slightly rounded edge or an alternative meshing software should be used. The meshing approach taken in this thesis is adequate but not ideal.

- Finally, insight to the interaction of multiple turbines would benefit the industry. It would be possible to study lateral turbines by modelling one turbine and incorporating a mirrored wall boundary. However, the impact of wake shadowing on turbine performance and loading should be considered as this will be experienced in true tidal arrays.

References

Afgan, I., McNaughton, J., Rolfo, S., Apsley, D. D., Stallard, T., & Stansby, P. (2013). Turbulent flow and loading on a tidal stream turbine by LES and RANS. *International Journal of Heat and Fluid Flow, 43*, 96-108. doi: 10.1016/j.ijheatfluidflow.2013.03.010

Agency, I. E. (2014). Key World Energy Statistics (pp. 82).

ANSYS, I. (2013). *ANSYS CFX-Solver Theory Guide: Release 15.0*. 275 Technology Drive, Canonsburg, PA 15317.

Arnold, M., Biskup, F., Matha, D., & Cheng, P. W. (2013, September 2-5). *Simulation of Rotor-Foundation-Interaction on Tidal Current Turbines with Computational Fluid Dynamics.* Paper presented at the The 10th European Wave and Tidal Energy Conference, Aalborg, Denmark.

Bahaj, A. S., Molland, A. F., Chaplin, J. R., & Batten, W. M. J. (2007a). Power and thrust measurements of marine current turbines under various hydrodynamic flow conditions in a cavitation tunnel and a towing tank. *Renewable Energy, 32*(3), 407-426. doi: 10.1016/j.renene.2006.01.012

Bahaj, A. S., Myers, L., Thomson, M., & Jorge, N. (2007b). *Characterising the wake of horizontal axis marine current turbines.* Paper presented at the The 7th European Wave and Tidal Energy Conference, Porto, Portugal.

Bai, G., Li, J., Fan, P., & Li, G. (2013). Numerical investigations of the effects of different arrays on power extractions of horizontal axis tidal current turbines. *Renewable Energy, 53*, 180-186. doi: 10.1016/j.renene.2012.10.048

Barnsley, M. J., & Wellicome, J. F. (1990). Final report on the 2nd phase of development and testing of a horizontal axis wind turbine test rig for the investigation of stall regulation aerodynamics. Carried out under ETSU Agreement E.5A/CON5103/1746.

Batten, W. M. J., Bahaj, A. S., Molland, A. F., & Chaplin, J. R. (2008). The prediction of the hydrodynamic performance of marine current turbines. *Renewable Energy, 33*(5), 1085-1096. doi: 10.1016/j.renene.2007.05.043

Burton Wold Windfarm - A Output. from http://www.variablepitch.co.uk/stations/121/

Clarke, J. A., Connor, G., Grant, A. D., & Johnstone, C. M. (2006). Design and testing of a contra-rotating tidal current turbine. *Proceedings of the Institution of Mechanical Engineers, Part A: Journal of Power and Energy, 221*(2), 171-179. doi: 10.1243/09576509jpe296

Doman, D. A., Murray, R. E., Pegg, M. J., Gracie, K., Johnstone, C. M., & Nevalainen, T. (2015). Tow-tank testing of a 1/20th scale horizontal axis tidal turbine with uncertainty analysis. *International Journal of Marine Energy, 11*, 105-119. doi: 10.1016/j.ijome.2015.06.003

Etemadi, A., Emami, Y., AsefAfshar, O., & Emdadi, A. (2011). Electricity Generation by the Tidal Barrages. *Energy Procedia, 12*, 928-935. doi: 10.1016/j.egypro.2011.10.122

Evans, P., Armstrong, S., Wilson, C., Fairley, I., Wooldridge, C., & Masters, I. (2013, September 2-5). *Characterisation of a Highly Energetic Tidal Energy Site with Specific Reference to Hydrodynamics and Bathymetry.* Paper presented at the The 10th European Wave and Tidal Energy Conference, Aalborg, Denmark.

Faudot, C., Dahlhaug, O. G., & Holst, M. A. (2013, September 2-5). *Tidal turbine blades in runaway situation: experimental and numerical approaches.* Paper presented at the The 10th European Wave and Tidal Energy Conference, Aalborg, Denmark.

Froude, R. E. (1889). On the part played in propulsion by differences of fluid pressure. *Transactions of the Institution of Naval Architects, 30*, pp. 390 - 405.

Froude, W. (1878). On the elementary relation between pitch, slip, and propulsive efficiency. *Transactions of the Institution of Naval Architects, 19*, pp. 47-65.

Glauert, H. (1935). Airplane Propellers. In W. F. Durand (Ed.), *Aerodynamic Theory* (Vol. 4, pp. 169-269). Berlin: Springer Verlag.

Glauert, H. (1947). *The elements of aerofoil and airscrew theory, 2nd ed.* New York: Cambridge University Press.

Gretton, G. I., Bruce, T., & Ingram, D. M. (2009). *Hydrodynamic modelling of a vertical axis tidal current turbine using CFD.* Paper presented at the The 8th European Wave and Tidal Energy Conference, Uppsala, Sweden.

Guo, Q., Zhou, L. J., & Wang, Z. W. (2015). Numerical simulation of cavitation for a horizontal axis marine current turbine. *IOP Conference Series: Materials Science and Engineering, 72*(4), 6 p. doi: 10.1088/1757-899x/72/4/042045

Harrison, M. E., Batten, W. M. J., Myers, L. E., & Bahaj, A. S. (2009). *A comparison between CFD simulations and experiments for predicting the far wake of horizontal axis tidal turbines.* Paper presented at the The 8th European Wave and Tidal Energy Conference, Uppsala, Sweden.

Hooper, T., & Austen, M. (2013). Tidal barrages in the UK: Ecological and social impacts, potential mitigation, and tools to support barrage planning. *Renewable and Sustainable Energy Reviews, 23*, 289-298. doi: 10.1016/j.rser.2013.03.001

Jo, C. H., Lee, J. H., Rho, Y. H., & Lee, K. H. (2014). Performance analysis of a HAT tidal current turbine and wake flow characteristics. *Renewable Energy, 65*, 175-182. doi: 10.1016/j.renene.2013.08.027

Jo, C. H., Lee, K. H., & Lee, J. H. (2013, September 2-5). *Design load analysis of fatigue ion tidal current turbine caused by downstream tower structure.* Paper presented at the The 10th European Wave and Tidal Energy Conference.

Jo, C. h., Yim, J. y., Lee, K. h., & Rho, Y. h. (2012). Performance of horizontal axis tidal current turbine by blade configuration. *Renewable Energy, 42*, 195-206. doi: 10.1016/j.renene.2011.08.017

Johnson, W. (1980). *Helicopter Theory* (Vol. 1). New York: Dover Publications, Inc.

Kang, S., Borazjani, I., Colby, J. A., & Sotiropoulos, F. (2012). Numerical simulation of 3D flow past a real-life marine hydrokinetic turbine. *Advances in Water Resources, 39*, 33-43. doi: 10.1016/j.advwatres.2011.12.012

Karsten, R. H., McMillan, J. M., Lickley, M. J., & Haynes, R. D. (2008). Assessment of tidal current energy in the Minas Passage, Bay of Fundy. *Proceedings of the Institution of Mechanical Engineers, Part A: Journal of Power and Energy, 222*(5), 493-507. doi: 10.1243/09576509jpe555

Keck, R.-E. (2012). A numerical investigation of nacelle anemometry for a HAWT using actuator disc and line models in CFX. *Renewable Energy, 48*, 72-84. doi: 10.1016/j.renene.2012.04.004

Khalid, S. S., Liang, Z., & Qi-hu, S. (2013). CFD Simulation of Twin Vertical Axis Tidal Turbines System. *Research Journal of Applied Sciences, Engineering and Technology, 5*, 6.

Lawson, M. J., Li, Y., & Sale, D. C. (2011, June 19-24). *Development and Verification of a Computational Fluid Dynamics Model of a Horizontal-Axis Tidal Current Turbine.* Paper presented at the The 30th International Conference on Ocean, Offshore, and Arctic Engineering, Rotterdam, The Netherlands.

Lee, J. H., Park, S., Kim, D. H., Rhee, S. H., & Kim, M.-C. (2012). Computational methods for performance analysis of horizontal axis tidal stream turbines. *Applied Energy, 98*, 512-523. doi: 10.1016/j.apenergy.2012.04.018

Lloyd, T. P., Turnock, S. R., & Humphrey, V. F. (2013, September 2-5). *Computation of Inflow Turbulence Noise of a Tidal Turbine.* Paper presented at the The 10th European Wave and Tidal Energy Conference, Aalborg, Denmark.

Majumdar, S. (1988). Role of Underrelaxation in Momentum Interpolation for Calculation of Flow with Nonstaggered Grids. *Numerical Heat Transfer, 13*, 125-132.

Malki, R., Masters, I., Williams, A. J., & Croft, T. N. (2012, June 17-22). *A Numerical Investigation into Tidal Stream Turbine Wake Dynamics and Device Performance in Non-Uniform Flows.* Paper presented at the the 22nd International Offshore and Polar Engineering Conference, Rhodes, Greece.

Malki, R., Williams, A. J., Croft, T. N., Togneri, M., & Masters, I. (2013). A coupled blade element momentum – Computational fluid dynamics model for evaluating tidal stream turbine performance. *Applied Mathematical Modelling, 37*(5), 3006-3020. doi: 10.1016/j.apm.2012.07.025

Marsh, P., Ranmuthugala, D., Penesis, I., & Thomas, G. (2012, 3-7, December 2012). *Three Dimensional Numerical Simulations of a Straight-Bladed Vertical Axis Tidal Turbine.* Paper presented at the 18th Australasian Fluid Mechanics Conference, Launceston, Australia.

Mason-Jones, A., O'Doherty, D. M., Morris, C. E., O'Doherty, T., Byrne, C. B., Prickett, P. W., . . . Poole, R. J. (2012). Non-dimensional scaling of tidal stream turbines. *Energy, 44*(1), 820-829. doi: 10.1016/j.energy.2012.05.010

Masters, I., Malki, R., Williams, A. J., & Croft, T. N. (2012). *A Modified k-epsilon Turbulence Model for Tidal Stream Turbine Simulations Using a Coupled BEM-CFD Model*. Paper presented at the 4th International Conference on Ocean Energy, Dublin.

Masters, I., Malki, R., Williams, A. J., & Croft, T. N. (2013). The influence of flow acceleration on tidal stream turbine wake dynamics: A numerical study using a coupled BEM–CFD model. *Applied Mathematical Modelling, 37*(16-17), 7905-7918. doi: 10.1016/j.apm.2013.06.004

Masters, I., Willis, M., & Orme, J. A. C. (2011). A robust blade element momentum theory model for tidal stream turbines including tip and hub loss corrections. *Journal of Marine Engineering and Technology, 10*(1), 25-35.

McNaughton, J., Rolfo, S., Apsley, D. D., Afgan, I., Stansby, P., & Stallard, T. (2012, Nov. 27-30). *CFD Predicition of Turbulent Flow on an Experimental Tidal Stream Turbine using RANS modelling.* Paper presented at the The 1st Asian Wave and Tidal Energy Conference Series, Jeju Island, Korea.

McSherry, R., Grimwade, J., Jones, I., Mathias, S., Wells, A., & Mateus, A. (2011). *3D CFD modelling of tidal turbine performance with validation against laboratory experiments.* Paper presented at the The 9th European Wave and Tidal Energy Conference, Southampton, UK.

Menter, F. (1994). Two-equation eddy-viscosity turbulence models for engineering applications. *AIAA Journal, 32*(8), 1598-1605.

Mycek, P., Gaurier, B., Germain, G., Facq, J. V., Bacchetti, T., Pinon, G., & Rivoalen, E. (2013, September 2-5). *Characterisation of the Interactions between Horizontal Axis Turbines Aligned with the Flow.* Paper presented at the The 10th European Wave and Tidal Energy Conference, Aalborg, Denmark.

Mycek, P., Gaurier, B., Germain, G., Pinon, G., & Rivoalen, E. (2014a). Experimental study of the turbulence intensity effects on marine current turbines behaviour. Part I: One single turbine. *Renewable Energy, 66*, 729-746. doi: 10.1016/j.renene.2013.12.036

Mycek, P., Gaurier, B., Germain, G., Pinon, G., & Rivoalen, E. (2014b). Experimental study of the turbulence intensity effects on marine current turbines behaviour. Part II: Two interacting turbines. *Renewable Energy, 68*, 876-892. doi: 10.1016/j.renene.2013.12.048

Myers, L. E., & Bahaj, A. S. (2010). Experimental analysis of the flow field around horizontal axis tidal turbines by use of scale mesh disk rotor simulators. *Ocean Engineering, 37*(2-3), 218-227. doi: 10.1016/j.oceaneng.2009.11.004

O'Doherty, T., Mason-Jones, A., O'Doherty, D. M., Byrne, C. B., Owen, I., & Wang, Y. X. (2009). *Experimental and Computational Analysis of a Model Horizontal Axis Tidal Turbine.* Paper presented at the The 8th European Wave and Tidal Energy Conference, Uppsala, Sweden.

Park, N. (2007). Sihwa Tidal Power Plant: a success of environment and energy policy in Korea

Phillips, A. B., Turnock, S. R., & Furlong, M. (2009). Evaluation of manoeuvring coefficients of a self-propelled ship using a blade element momentum propeller model coupled to a Reynolds averaged Navier Stokes flow solver. *Ocean Engineering, 36*(15-16), 1217-1225. doi: 10.1016/j.oceaneng.2009.07.019

Rankine, W. J. M. (1865). On the machanical principles of the action of propellers. *Transactions of the Institution of Naval Architects, 6*, pp. 13-39.

Rhie, C. M., & Chow, W. L. (1982). *A Numerical Study of the Turbulent Flow Past an Isolated Airfoil with Trailing Edge Separation*. Paper presented at the AIAA/ASME 3rd Joint Thermophysics, Fluids, Plasma and Heat Transfer Conference, St. Louis, Missouri.

Sheng, Q., Khalid, S. S., Xiong, Z., Sahib, G., & Zhang, L. (2013). CFD simulation of fixed and variable pitch vertical axis tidal turbine. *Journal of Marine Science and Application, 12*(2), 185-192. doi: 10.1007/s11804-013-1184-z

Shives, M., & Crawford, C. (2014, 4 November). *Turbulence Modelling for Accurate Wake Prediction in Tidal Turbine Arrays.* Paper presented at the 5th International Conference on Ocean Energy (ICOE), Halifax, Nova Scotia.

Sørensen, J. N., & Kock, C. K. (1995). A model for unsteady rotor aerodynamics. *Journal of Wind Engineering and Industrial Aerodynamics, 58*, 259-275.

Turnock, S. R., Phillips, A. B., Banks, J., & Nicholls-Lee, R. (2011). Modelling tidal current turbine wakes using a coupled RANS-BEMT approach as a tool for analysing power capture of arrays of turbines. *Ocean Engineering, 38*(11-12), 1300-1307. doi: 10.1016/j.oceaneng.2011.05.018

Wilcox, D. C. (1986). *Multiscale Model for Turbulent Flows*. Paper presented at the AIAA 24th Aerospace Sciences Meeting, Reno, Nevada.

Yang, B., & Lawn, C. (2011). Fluid dynamic performance of a vertical axis turbine for tidal currents. *Renewable Energy, 36*, 3355-3366.

Appendix A: Blade profile creation code

This Matlab code take a nominal airfoil profile and applies a scale and twist to match that of the experimental blade. Six individual profiles are created with a NACA 63-8XX designation.

```
clc; clear all; close all;

%This section loads and plots the nominal NACA profile
R=400; %Blade radius in [mm]
i=1;

%NACA profile coordinates taken from website http://www.mh-aerotools.de/airfoils/javafoil.htm
load NACA_63_815_From_Java_Foil_Upper.txt; %This loads Upper NACA data points into Matrix
load NACA_63_815_From_Java_Foil_Lower.txt; %This loads Lower NACA data points into Matrix

% The column labelling is this:  Point      X Y

rows = 101;

NACA_63_815_Upper(:,1)=NACA_63_815_From_Java_Foil_Upper(:,1);
NACA_63_815_Upper(:,2)=NACA_63_815_From_Java_Foil_Upper(:,2);
NACA_63_815_Lower(:,1)=NACA_63_815_From_Java_Foil_Lower(:,1);
NACA_63_815_Lower(:,2)=NACA_63_815_From_Java_Foil_Lower(:,2);

x_nom_Upper=NACA_63_815_Upper(:,1); %Gets x data points for the upper half
y_nom_Upper=NACA_63_815_Upper(:,2); %Gets y data points for the upper half
x_nom_Lower=NACA_63_815_Lower(:,1); %Gets x data points for the lower half
y_nom_Lower=NACA_63_815_Lower(:,2); %Gets y data points for the lower half

plot(x_nom_Upper, y_nom_Upper, x_nom_Lower, y_nom_Lower)

%% This section loads chord, radius and pitch data from Bahaj
% and applies it to the NACA profile. 17 Profiles are plotted

load Bahaj_Blade_Data.txt; %This loads Bahaj Blade Parameters
r=Bahaj_Blade_Data(:,2); %Blade Radius Data in [mm]
c=Bahaj_Blade_Data(:,3).*R; %Blade Chord length Data in [mm]
p=Bahaj_Blade_Data(:,4); %Blade Angle Data in [deg]

num=numel(x_nom_Upper);

r80_Upper=zeros(num,3); r80_Upper(:,3)=80;
r100_Upper=zeros(num,3); r100_Upper(:,3)=100;
r120_Upper=zeros(num,3); r120_Upper(:,3)=120;
r140_Upper=zeros(num,3); r140_Upper(:,3)=140;
r160_Upper=zeros(num,3); r160_Upper(:,3)=160;
r180_Upper=zeros(num,3); r180_Upper(:,3)=180;
r200_Upper=zeros(num,3); r200_Upper(:,3)=200;
r220_Upper=zeros(num,3); r220_Upper(:,3)=220;
```

```
r240_Upper=zeros(num,3); r240_Upper(:,3)=240;
r260_Upper=zeros(num,3); r260_Upper(:,3)=260;
r280_Upper=zeros(num,3); r280_Upper(:,3)=280;
r300_Upper=zeros(num,3); r300_Upper(:,3)=300;
r320_Upper=zeros(num,3); r320_Upper(:,3)=320;
r340_Upper=zeros(num,3); r340_Upper(:,3)=340;
r360_Upper=zeros(num,3); r360_Upper(:,3)=360;
r380_Upper=zeros(num,3); r380_Upper(:,3)=380;
r400_Upper=zeros(num,3); r400_Upper(:,3)=400;

r80_Lower=zeros(num,3); r80_Lower(:,3)=80;
r100_Lower=zeros(num,3); r100_Lower(:,3)=100;
r120_Lower=zeros(num,3); r120_Lower(:,3)=120;
r140_Lower=zeros(num,3); r140_Lower(:,3)=140;
r160_Lower=zeros(num,3); r160_Lower(:,3)=160;
r180_Lower=zeros(num,3); r180_Lower(:,3)=180;
r200_Lower=zeros(num,3); r200_Lower(:,3)=200;
r220_Lower=zeros(num,3); r220_Lower(:,3)=220;
r240_Lower=zeros(num,3); r240_Lower(:,3)=240;
r260_Lower=zeros(num,3); r260_Lower(:,3)=260;
r280_Lower=zeros(num,3); r280_Lower(:,3)=280;
r300_Lower=zeros(num,3); r300_Lower(:,3)=300;
r320_Lower=zeros(num,3); r320_Lower(:,3)=320;
r340_Lower=zeros(num,3); r340_Lower(:,3)=340;
r360_Lower=zeros(num,3); r360_Lower(:,3)=360;
r380_Lower=zeros(num,3); r380_Lower(:,3)=380;
r400_Lower=zeros(num,3); r400_Lower(:,3)=400;

while i<rows+1
   r80_Upper(i,1)=x_nom_Upper(i).*c(1); r80_Upper(i,2)=y_nom_Upper(i).*c(1);
   r100_Upper(i,1)=x_nom_Upper(i).*c(2); r100_Upper(i,2)=y_nom_Upper(i).*c(2);
   r120_Upper(i,1)=x_nom_Upper(i).*c(3); r120_Upper(i,2)=y_nom_Upper(i).*c(3);
   r140_Upper(i,1)=x_nom_Upper(i).*c(4); r140_Upper(i,2)=y_nom_Upper(i).*c(4);
   r160_Upper(i,1)=x_nom_Upper(i).*c(5); r160_Upper(i,2)=y_nom_Upper(i).*c(5);
   r180_Upper(i,1)=x_nom_Upper(i).*c(6); r180_Upper(i,2)=y_nom_Upper(i).*c(6);
   r200_Upper(i,1)=x_nom_Upper(i).*c(7); r200_Upper(i,2)=y_nom_Upper(i).*c(7);
   r220_Upper(i,1)=x_nom_Upper(i).*c(8); r220_Upper(i,2)=y_nom_Upper(i).*c(8);
   r240_Upper(i,1)=x_nom_Upper(i).*c(9); r240_Upper(i,2)=y_nom_Upper(i).*c(9);
   r260_Upper(i,1)=x_nom_Upper(i).*c(10); r260_Upper(i,2)=y_nom_Upper(i).*c(10);
   r280_Upper(i,1)=x_nom_Upper(i).*c(11); r280_Upper(i,2)=y_nom_Upper(i).*c(11);
   r300_Upper(i,1)=x_nom_Upper(i).*c(12); r300_Upper(i,2)=y_nom_Upper(i).*c(12);
   r320_Upper(i,1)=x_nom_Upper(i).*c(13); r320_Upper(i,2)=y_nom_Upper(i).*c(13);
   r340_Upper(i,1)=x_nom_Upper(i).*c(14); r340_Upper(i,2)=y_nom_Upper(i).*c(14);
   r360_Upper(i,1)=x_nom_Upper(i).*c(15); r360_Upper(i,2)=y_nom_Upper(i).*c(15);
   r380_Upper(i,1)=x_nom_Upper(i).*c(16); r380_Upper(i,2)=y_nom_Upper(i).*c(16);
   r400_Upper(i,1)=x_nom_Upper(i).*c(17); r400_Upper(i,2)=y_nom_Upper(i).*c(17);

   r80_Lower(i,1)=x_nom_Lower(i).*c(1); r80_Lower(i,2)=y_nom_Lower(i).*c(1);
   r100_Lower(i,1)=x_nom_Lower(i).*c(2); r100_Lower(i,2)=y_nom_Lower(i).*c(2);
   r120_Lower(i,1)=x_nom_Lower(i).*c(3); r120_Lower(i,2)=y_nom_Lower(i).*c(3);
   r140_Lower(i,1)=x_nom_Lower(i).*c(4); r140_Lower(i,2)=y_nom_Lower(i).*c(4);
   r160_Lower(i,1)=x_nom_Lower(i).*c(5); r160_Lower(i,2)=y_nom_Lower(i).*c(5);
   r180_Lower(i,1)=x_nom_Lower(i).*c(6); r180_Lower(i,2)=y_nom_Lower(i).*c(6);
   r200_Lower(i,1)=x_nom_Lower(i).*c(7); r200_Lower(i,2)=y_nom_Lower(i).*c(7);
   r220_Lower(i,1)=x_nom_Lower(i).*c(8); r220_Lower(i,2)=y_nom_Lower(i).*c(8);
```

```
    r240_Lower(i,1)=x_nom_Lower(i).*c(9); r240_Lower(i,2)=y_nom_Lower(i).*c(9);
    r260_Lower(i,1)=x_nom_Lower(i).*c(10); r260_Lower(i,2)=y_nom_Lower(i).*c(10);
    r280_Lower(i,1)=x_nom_Lower(i).*c(11); r280_Lower(i,2)=y_nom_Lower(i).*c(11);
    r300_Lower(i,1)=x_nom_Lower(i).*c(12); r300_Lower(i,2)=y_nom_Lower(i).*c(12);
    r320_Lower(i,1)=x_nom_Lower(i).*c(13); r320_Lower(i,2)=y_nom_Lower(i).*c(13);
    r340_Lower(i,1)=x_nom_Lower(i).*c(14); r340_Lower(i,2)=y_nom_Lower(i).*c(14);
    r360_Lower(i,1)=x_nom_Lower(i).*c(15); r360_Lower(i,2)=y_nom_Lower(i).*c(15);
    r380_Lower(i,1)=x_nom_Lower(i).*c(16); r380_Lower(i,2)=y_nom_Lower(i).*c(16);
    r400_Lower(i,1)=x_nom_Lower(i).*c(17); r400_Lower(i,2)=y_nom_Lower(i).*c(17);

    i=i+1;
end

figure(2)
x80_Upper=r80_Upper(:,1);x80old_Upper=x80_Upper;
y80_Upper=r80_Upper(:,2);y80old_Upper=y80_Upper;
x100_Upper=r100_Upper(:,1);x100old_Upper=x100_Upper;
y100_Upper=r100_Upper(:,2);y100old_Upper=y100_Upper;
x120_Upper=r120_Upper(:,1);x120old_Upper=x120_Upper;
y120_Upper=r120_Upper(:,2);y120old_Upper=y120_Upper;
x140_Upper=r140_Upper(:,1);x140old_Upper=x140_Upper;
y140_Upper=r140_Upper(:,2);y140old_Upper=y140_Upper;
x160_Upper=r160_Upper(:,1);x160old_Upper=x160_Upper;
y160_Upper=r160_Upper(:,2);y160old_Upper=y160_Upper;
x180_Upper=r180_Upper(:,1);x180old_Upper=x180_Upper;
y180_Upper=r180_Upper(:,2);y180old_Upper=y180_Upper;
x200_Upper=r200_Upper(:,1);x200old_Upper=x200_Upper;
y200_Upper=r200_Upper(:,2);y200old_Upper=y200_Upper;
x220_Upper=r220_Upper(:,1);x220old_Upper=x220_Upper;
y220_Upper=r220_Upper(:,2);y220old_Upper=y220_Upper;
x240_Upper=r240_Upper(:,1);x240old_Upper=x240_Upper;
y240_Upper=r240_Upper(:,2);y240old_Upper=y240_Upper;
x260_Upper=r260_Upper(:,1);x260old_Upper=x260_Upper;
y260_Upper=r260_Upper(:,2);y260old_Upper=y260_Upper;
x280_Upper=r280_Upper(:,1);x280old_Upper=x280_Upper;
y280_Upper=r280_Upper(:,2);y280old_Upper=y280_Upper;
x300_Upper=r300_Upper(:,1);x300old_Upper=x300_Upper;
y300_Upper=r300_Upper(:,2);y300old_Upper=y300_Upper;
x320_Upper=r320_Upper(:,1);x320old_Upper=x320_Upper;
y320_Upper=r320_Upper(:,2);y320old_Upper=y320_Upper;
x340_Upper=r340_Upper(:,1);x340old_Upper=x340_Upper;
y340_Upper=r340_Upper(:,2);y340old_Upper=y340_Upper;
x360_Upper=r360_Upper(:,1);x360old_Upper=x360_Upper;
y360_Upper=r360_Upper(:,2);y360old_Upper=y360_Upper;
x380_Upper=r380_Upper(:,1);x380old_Upper=x380_Upper;
y380_Upper=r380_Upper(:,2);y380old_Upper=y380_Upper;
x400_Upper=r400_Upper(:,1);x400old_Upper=x400_Upper;
y400_Upper=r400_Upper(:,2);y400old_Upper=y400_Upper;

x80_Lower=r80_Lower(:,1);x80old_Lower=x80_Lower;
y80_Lower=r80_Lower(:,2);y80old_Lower=y80_Lower;
x100_Lower=r100_Lower(:,1);x100old_Lower=x100_Lower;
y100_Lower=r100_Lower(:,2);y100old_Lower=y100_Lower;
x120_Lower=r120_Lower(:,1);x120old_Lower=x120_Lower;
y120_Lower=r120_Lower(:,2);y120old_Lower=y120_Lower;
```

```
x140_Lower=r140_Lower(:,1);x140old_Lower=x140_Lower;
y140_Lower=r140_Lower(:,2);y140old_Lower=y140_Lower;
x160_Lower=r160_Lower(:,1);x160old_Lower=x160_Lower;
y160_Lower=r160_Lower(:,2);y160old_Lower=y160_Lower;
x180_Lower=r180_Lower(:,1);x180old_Lower=x180_Lower;
y180_Lower=r180_Lower(:,2);y180old_Lower=y180_Lower;
x200_Lower=r200_Lower(:,1);x200old_Lower=x200_Lower;
y200_Lower=r200_Lower(:,2);y200old_Lower=y200_Lower;
x220_Lower=r220_Lower(:,1);x220old_Lower=x220_Lower;
y220_Lower=r220_Lower(:,2);y220old_Lower=y220_Lower;
x240_Lower=r240_Lower(:,1);x240old_Lower=x240_Lower;
y240_Lower=r240_Lower(:,2);y240old_Lower=y240_Lower;
x260_Lower=r260_Lower(:,1);x260old_Lower=x260_Lower;
y260_Lower=r260_Lower(:,2);y260old_Lower=y260_Lower;
x280_Lower=r280_Lower(:,1);x280old_Lower=x280_Lower;
y280_Lower=r280_Lower(:,2);y280old_Lower=y280_Lower;
x300_Lower=r300_Lower(:,1);x300old_Lower=x300_Lower;
y300_Lower=r300_Lower(:,2);y300old_Lower=y300_Lower;
x320_Lower=r320_Lower(:,1);x320old_Lower=x320_Lower;
y320_Lower=r320_Lower(:,2);y320old_Lower=y320_Lower;
x340_Lower=r340_Lower(:,1);x340old_Lower=x340_Lower;
y340_Lower=r340_Lower(:,2);y340old_Lower=y340_Lower;
x360_Lower=r360_Lower(:,1);x360old_Lower=x360_Lower;
y360_Lower=r360_Lower(:,2);y360old_Lower=y360_Lower;
x380_Lower=r380_Lower(:,1);x380old_Lower=x380_Lower;
y380_Lower=r380_Lower(:,2);y380old_Lower=y380_Lower;
x400_Lower=r400_Lower(:,1);x400old_Lower=x400_Lower;
y400_Lower=r400_Lower(:,2);y400old_Lower=y400_Lower;

hold on
plot(x80_Upper,y80_Upper,'k',x100_Upper,y100_Upper,'k',x120_Upper,y120_Upper,'k',...
    x140_Upper,y140_Upper,'k',x160_Upper,y160_Upper,'k',x180_Upper,y180_Upper,'k',...
    x200_Upper,y200_Upper,'k',x220_Upper,y220_Upper,'k',x240_Upper,y240_Upper,'k',...
    x260_Upper,y260_Upper,'k',x280_Upper,y280_Upper,'k',x300_Upper,y300_Upper,'k',...
    x320_Upper,y320_Upper,'k',x340_Upper,y340_Upper,'k',x360_Upper,y360_Upper,'k',...
    x380_Upper,y380_Upper,'k',x400_Upper,y400_Upper,'k',...
    x80_Lower,y80_Lower,'k',x100_Lower,y100_Lower,'k',x120_Lower,y120_Lower,'k',...
    x140_Lower,y140_Lower,'k',x160_Lower,y160_Lower,'k',x180_Lower,y180_Lower,'k',...
    x200_Lower,y200_Lower,'k',x220_Lower,y220_Lower,'k',x240_Lower,y240_Lower,'k',...
    x260_Lower,y260_Lower,'k',x280_Lower,y280_Lower,'k',x300_Lower,y300_Lower,'k',...
    x320_Lower,y320_Lower,'k',x340_Lower,y340_Lower,'k',x360_Lower,y360_Lower,'k',...
    x380_Lower,y380_Lower,'k',x400_Lower,y400_Lower,'k');
%% This section shifts the aerodynamic centre of each to the origin
i=1;
while i<num+1
    x80_Upper(i)=x80old_Upper(i)-0.25*max(x80old_Upper);
    x100_Upper(i)=x100old_Upper(i)-0.25*max(x100old_Upper);
    x120_Upper(i)=x120old_Upper(i)-0.25*max(x120old_Upper);
    x140_Upper(i)=x140old_Upper(i)-0.25*max(x140old_Upper);
    x160_Upper(i)=x160old_Upper(i)-0.25*max(x160old_Upper);
    x180_Upper(i)=x180old_Upper(i)-0.25*max(x180old_Upper);
    x200_Upper(i)=x200old_Upper(i)-0.25*max(x200old_Upper);
    x220_Upper(i)=x220old_Upper(i)-0.25*max(x220old_Upper);
    x240_Upper(i)=x240old_Upper(i)-0.25*max(x240old_Upper);
    x260_Upper(i)=x260old_Upper(i)-0.25*max(x260old_Upper);
    x280_Upper(i)=x280old_Upper(i)-0.25*max(x280old_Upper);
```

```
    x300_Upper(i)=x300old_Upper(i)-0.25*max(x300old_Upper);
    x320_Upper(i)=x320old_Upper(i)-0.25*max(x320old_Upper);
    x340_Upper(i)=x340old_Upper(i)-0.25*max(x340old_Upper);
    x360_Upper(i)=x360old_Upper(i)-0.25*max(x360old_Upper);
    x380_Upper(i)=x380old_Upper(i)-0.25*max(x380old_Upper);
    x400_Upper(i)=x400old_Upper(i)-0.25*max(x400old_Upper);

    x80_Lower(i)=x80old_Lower(i)-0.25*max(x80old_Lower);
    x100_Lower(i)=x100old_Lower(i)-0.25*max(x100old_Lower);
    x120_Lower(i)=x120old_Lower(i)-0.25*max(x120old_Lower);
    x140_Lower(i)=x140old_Lower(i)-0.25*max(x140old_Lower);
    x160_Lower(i)=x160old_Lower(i)-0.25*max(x160old_Lower);
    x180_Lower(i)=x180old_Lower(i)-0.25*max(x180old_Lower);
    x200_Lower(i)=x200old_Lower(i)-0.25*max(x200old_Lower);
    x220_Lower(i)=x220old_Lower(i)-0.25*max(x220old_Lower);
    x240_Lower(i)=x240old_Lower(i)-0.25*max(x240old_Lower);
    x260_Lower(i)=x260old_Lower(i)-0.25*max(x260old_Lower);
    x280_Lower(i)=x280old_Lower(i)-0.25*max(x280old_Lower);
    x300_Lower(i)=x300old_Lower(i)-0.25*max(x300old_Lower);
    x320_Lower(i)=x320old_Lower(i)-0.25*max(x320old_Lower);
    x340_Lower(i)=x340old_Lower(i)-0.25*max(x340old_Lower);
    x360_Lower(i)=x360old_Lower(i)-0.25*max(x360old_Lower);
    x380_Lower(i)=x380old_Lower(i)-0.25*max(x380old_Lower);
    x400_Lower(i)=x400old_Lower(i)-0.25*max(x400old_Lower);

    i=i+1;
end


figure(3)
hold on
plot(x80_Upper,y80_Upper,'k',x100_Upper,y100_Upper,'k',x120_Upper,y120_Upper,'k',...
    x140_Upper,y140_Upper,'k',x160_Upper,y160_Upper,'k',x180_Upper,y180_Upper,'k',...
    x200_Upper,y200_Upper,'k',x220_Upper,y220_Upper,'k',x240_Upper,y240_Upper,'k',...
    x260_Upper,y260_Upper,'k',x280_Upper,y280_Upper,'k',x300_Upper,y300_Upper,'k',...
    x320_Upper,y320_Upper,'k',x340_Upper,y340_Upper,'k',x360_Upper,y360_Upper,'k',...
    x380_Upper,y380_Upper,'k',x400_Upper,y400_Upper,'k',...
    x80_Lower,y80_Lower,'k',x100_Lower,y100_Lower,'k',x120_Lower,y120_Lower,'k',...
    x140_Lower,y140_Lower,'k',x160_Lower,y160_Lower,'k',x180_Lower,y180_Lower,'k',...
    x200_Lower,y200_Lower,'k',x220_Lower,y220_Lower,'k',x240_Lower,y240_Lower,'k',...
    x260_Lower,y260_Lower,'k',x280_Lower,y280_Lower,'k',x300_Lower,y300_Lower,'k',...
    x320_Lower,y320_Lower,'k',x340_Lower,y340_Lower,'k',x360_Lower,y360_Lower,'k',...
    x380_Lower,y380_Lower,'k',x400_Lower,y400_Lower,'k');

%% This section uses a matrix rotation method to rotate the individual profiles


NACA_63_815_profile_80_Upper(:,1)=x80_Upper; NACA_63_815_profile_80_Upper(:,2)=y80_Upper;
NACA_63_815_profile_100_Upper(:,1)=x100_Upper;
NACA_63_815_profile_100_Upper(:,2)=y100_Upper;
NACA_63_815_profile_120_Upper(:,1)=x120_Upper;
NACA_63_815_profile_120_Upper(:,2)=y120_Upper;
NACA_63_815_profile_140_Upper(:,1)=x140_Upper;
NACA_63_815_profile_140_Upper(:,2)=y140_Upper;
```

```
NACA_63_815_profile_160_Upper(:,1)=x160_Upper;
NACA_63_815_profile_160_Upper(:,2)=y160_Upper;
NACA_63_815_profile_180_Upper(:,1)=x180_Upper;
NACA_63_815_profile_180_Upper(:,2)=y180_Upper;
NACA_63_815_profile_200_Upper(:,1)=x200_Upper;
NACA_63_815_profile_200_Upper(:,2)=y200_Upper;
NACA_63_815_profile_220_Upper(:,1)=x220_Upper;
NACA_63_815_profile_220_Upper(:,2)=y220_Upper;
NACA_63_815_profile_240_Upper(:,1)=x240_Upper;
NACA_63_815_profile_240_Upper(:,2)=y240_Upper;
NACA_63_815_profile_260_Upper(:,1)=x260_Upper;
NACA_63_815_profile_260_Upper(:,2)=y260_Upper;
NACA_63_815_profile_280_Upper(:,1)=x280_Upper;
NACA_63_815_profile_280_Upper(:,2)=y280_Upper;
NACA_63_815_profile_300_Upper(:,1)=x300_Upper;
NACA_63_815_profile_300_Upper(:,2)=y300_Upper;
NACA_63_815_profile_320_Upper(:,1)=x320_Upper;
NACA_63_815_profile_320_Upper(:,2)=y320_Upper;
NACA_63_815_profile_340_Upper(:,1)=x340_Upper;
NACA_63_815_profile_340_Upper(:,2)=y340_Upper;
NACA_63_815_profile_360_Upper(:,1)=x360_Upper;
NACA_63_815_profile_360_Upper(:,2)=y360_Upper;
NACA_63_815_profile_380_Upper(:,1)=x380_Upper;
NACA_63_815_profile_380_Upper(:,2)=y380_Upper;
NACA_63_815_profile_400_Upper(:,1)=x400_Upper;
NACA_63_815_profile_400_Upper(:,2)=y400_Upper;

NACA_63_815_profile_80_Lower(:,1)=x80_Lower; NACA_63_815_profile_80_Lower(:,2)=y80_Lower;
NACA_63_815_profile_100_Lower(:,1)=x100_Lower;
NACA_63_815_profile_100_Lower(:,2)=y100_Lower;
NACA_63_815_profile_120_Lower(:,1)=x120_Lower;
NACA_63_815_profile_120_Lower(:,2)=y120_Lower;
NACA_63_815_profile_140_Lower(:,1)=x140_Lower;
NACA_63_815_profile_140_Lower(:,2)=y140_Lower;
NACA_63_815_profile_160_Lower(:,1)=x160_Lower;
NACA_63_815_profile_160_Lower(:,2)=y160_Lower;
NACA_63_815_profile_180_Lower(:,1)=x180_Lower;
NACA_63_815_profile_180_Lower(:,2)=y180_Lower;
NACA_63_815_profile_200_Lower(:,1)=x200_Lower;
NACA_63_815_profile_200_Lower(:,2)=y200_Lower;
NACA_63_815_profile_220_Lower(:,1)=x220_Lower;
NACA_63_815_profile_220_Lower(:,2)=y220_Lower;
NACA_63_815_profile_240_Lower(:,1)=x240_Lower;
NACA_63_815_profile_240_Lower(:,2)=y240_Lower;
NACA_63_815_profile_260_Lower(:,1)=x260_Lower;
NACA_63_815_profile_260_Lower(:,2)=y260_Lower;
NACA_63_815_profile_280_Lower(:,1)=x280_Lower;
NACA_63_815_profile_280_Lower(:,2)=y280_Lower;
NACA_63_815_profile_300_Lower(:,1)=x300_Lower;
NACA_63_815_profile_300_Lower(:,2)=y300_Lower;
NACA_63_815_profile_320_Lower(:,1)=x320_Lower;
NACA_63_815_profile_320_Lower(:,2)=y320_Lower;
NACA_63_815_profile_340_Lower(:,1)=x340_Lower;
NACA_63_815_profile_340_Lower(:,2)=y340_Lower;
NACA_63_815_profile_360_Lower(:,1)=x360_Lower;
NACA_63_815_profile_360_Lower(:,2)=y360_Lower;
```

```
NACA_63_815_profile_380_Lower(:,1)=x380_Lower;
NACA_63_815_profile_380_Lower(:,2)=y380_Lower;
NACA_63_815_profile_400_Lower(:,1)=x400_Lower;
NACA_63_815_profile_400_Lower(:,2)=y400_Lower;

theta=-15*pi/180;
b=[cos(theta) -sin(theta); sin(theta) cos(theta)];
NACA_63_815_profile_80_Upper=NACA_63_815_profile_80_Upper*b;

theta=-12.1*pi/180;
b=[cos(theta) -sin(theta); sin(theta) cos(theta)];
NACA_63_815_profile_100_Upper=NACA_63_815_profile_100_Upper*b;

theta=-9.5*pi/180;
b=[cos(theta) -sin(theta); sin(theta) cos(theta)];
NACA_63_815_profile_120_Upper=NACA_63_815_profile_120_Upper*b;

theta=-7.6*pi/180;
b=[cos(theta) -sin(theta); sin(theta) cos(theta)];
NACA_63_815_profile_140_Upper=NACA_63_815_profile_140_Upper*b;

theta=-6.1*pi/180;
b=[cos(theta) -sin(theta); sin(theta) cos(theta)];
NACA_63_815_profile_160_Upper=NACA_63_815_profile_160_Upper*b;

theta=-4.9*pi/180;
b=[cos(theta) -sin(theta); sin(theta) cos(theta)];
NACA_63_815_profile_180_Upper=NACA_63_815_profile_180_Upper*b;

theta=-3.9*pi/180;
b=[cos(theta) -sin(theta); sin(theta) cos(theta)];
NACA_63_815_profile_200_Upper=NACA_63_815_profile_200_Upper*b;

theta=-3.1*pi/180;
b=[cos(theta) -sin(theta); sin(theta) cos(theta)];
NACA_63_815_profile_220_Upper=NACA_63_815_profile_220_Upper*b;

theta=-2.4*pi/180;
b=[cos(theta) -sin(theta); sin(theta) cos(theta)];
NACA_63_815_profile_240_Upper=NACA_63_815_profile_240_Upper*b;

theta=-1.9*pi/180;
b=[cos(theta) -sin(theta); sin(theta) cos(theta)];
NACA_63_815_profile_260_Upper=NACA_63_815_profile_260_Upper*b;

theta=-1.5*pi/180;
b=[cos(theta) -sin(theta); sin(theta) cos(theta)];
NACA_63_815_profile_280_Upper=NACA_63_815_profile_280_Upper*b;

theta=-1.2*pi/180;
b=[cos(theta) -sin(theta); sin(theta) cos(theta)];
NACA_63_815_profile_300_Upper=NACA_63_815_profile_300_Upper*b;
```

```
theta=-0.9*pi/180;
b=[cos(theta) -sin(theta); sin(theta) cos(theta)];
NACA_63_815_profile_320_Upper=NACA_63_815_profile_320_Upper*b;

theta=-0.6*pi/180;
b=[cos(theta) -sin(theta); sin(theta) cos(theta)];
NACA_63_815_profile_340_Upper=NACA_63_815_profile_340_Upper*b;

theta=-0.4*pi/180;
b=[cos(theta) -sin(theta); sin(theta) cos(theta)];
NACA_63_815_profile_360_Upper=NACA_63_815_profile_360_Upper*b;

theta=-0.2*pi/180;
b=[cos(theta) -sin(theta); sin(theta) cos(theta)];
NACA_63_815_profile_380_Upper=NACA_63_815_profile_380_Upper*b;

theta=-0*pi/180;
b=[cos(theta) -sin(theta); sin(theta) cos(theta)];
NACA_63_815_profile_400_Upper=NACA_63_815_profile_400_Upper*b;


theta=-15*pi/180;
b=[cos(theta) -sin(theta); sin(theta) cos(theta)];
NACA_63_815_profile_80_Lower=NACA_63_815_profile_80_Lower*b;

theta=-12.1*pi/180;
b=[cos(theta) -sin(theta); sin(theta) cos(theta)];
NACA_63_815_profile_100_Lower=NACA_63_815_profile_100_Lower*b;

theta=-9.5*pi/180;
b=[cos(theta) -sin(theta); sin(theta) cos(theta)];
NACA_63_815_profile_120_Lower=NACA_63_815_profile_120_Lower*b;

theta=-7.6*pi/180;
b=[cos(theta) -sin(theta); sin(theta) cos(theta)];
NACA_63_815_profile_140_Lower=NACA_63_815_profile_140_Lower*b;

theta=-6.1*pi/180;
b=[cos(theta) -sin(theta); sin(theta) cos(theta)];
NACA_63_815_profile_160_Lower=NACA_63_815_profile_160_Lower*b;

theta=-4.9*pi/180;
b=[cos(theta) -sin(theta); sin(theta) cos(theta)];
NACA_63_815_profile_180_Lower=NACA_63_815_profile_180_Lower*b;

theta=-3.9*pi/180;
b=[cos(theta) -sin(theta); sin(theta) cos(theta)];
NACA_63_815_profile_200_Lower=NACA_63_815_profile_200_Lower*b;

theta=-3.1*pi/180;
b=[cos(theta) -sin(theta); sin(theta) cos(theta)];
NACA_63_815_profile_220_Lower=NACA_63_815_profile_220_Lower*b;
```

```
theta=-2.4*pi/180;
b=[cos(theta) -sin(theta); sin(theta) cos(theta)];
NACA_63_815_profile_240_Lower=NACA_63_815_profile_240_Lower*b;

theta=-1.9*pi/180;
b=[cos(theta) -sin(theta); sin(theta) cos(theta)];
NACA_63_815_profile_260_Lower=NACA_63_815_profile_260_Lower*b;

theta=-1.5*pi/180;
b=[cos(theta) -sin(theta); sin(theta) cos(theta)];
NACA_63_815_profile_280_Lower=NACA_63_815_profile_280_Lower*b;

theta=-1.2*pi/180;
b=[cos(theta) -sin(theta); sin(theta) cos(theta)];
NACA_63_815_profile_300_Lower=NACA_63_815_profile_300_Lower*b;

theta=-0.9*pi/180;
b=[cos(theta) -sin(theta); sin(theta) cos(theta)];
NACA_63_815_profile_320_Lower=NACA_63_815_profile_320_Lower*b;

theta=-0.6*pi/180;
b=[cos(theta) -sin(theta); sin(theta) cos(theta)];
NACA_63_815_profile_340_Lower=NACA_63_815_profile_340_Lower*b;

theta=-0.4*pi/180;
b=[cos(theta) -sin(theta); sin(theta) cos(theta)];
NACA_63_815_profile_360_Lower=NACA_63_815_profile_360_Lower*b;

theta=-0.2*pi/180;
b=[cos(theta) -sin(theta); sin(theta) cos(theta)];
NACA_63_815_profile_380_Lower=NACA_63_815_profile_380_Lower*b;

theta=-0*pi/180;
b=[cos(theta) -sin(theta); sin(theta) cos(theta)];
NACA_63_815_profile_400_Lower=NACA_63_815_profile_400_Lower*b;


x80old_Upper=x80_Upper; y80old_Upper=y80_Upper;
x100old_Upper=x100_Upper; y100old_Upper=y100_Upper;
x120old_Upper=x120_Upper; y120old_Upper=y120_Upper;
x140old_Upper=x140_Upper; y140old_Upper=y140_Upper;
x160old_Upper=x160_Upper; y160old_Upper=y160_Upper;
x180old_Upper=x180_Upper; y180old_Upper=y180_Upper;
x200old_Upper=x200_Upper; y200old_Upper=y200_Upper;
x220old_Upper=x220_Upper; y220old_Upper=y220_Upper;
x240old_Upper=x240_Upper; y240old_Upper=y240_Upper;
x260old_Upper=x260_Upper; y260old_Upper=y260_Upper;
x280old_Upper=x280_Upper; y280old_Upper=y280_Upper;
x300old_Upper=x300_Upper; y300old_Upper=y300_Upper;
x320old_Upper=x320_Upper; y320old_Upper=y320_Upper;
x340old_Upper=x340_Upper; y340old_Upper=y340_Upper;
x360old_Upper=x360_Upper; y360old_Upper=y360_Upper;
x380old_Upper=x380_Upper; y380old_Upper=y380_Upper;
x400old_Upper=x400_Upper; y400old_Upper=y400_Upper;
```

```
x80old_Lower=x80_Lower; y80old_Lower=y80_Lower;
x100old_Lower=x100_Lower; y100old_Lower=y100_Lower;
x120old_Lower=x120_Lower; y120old_Lower=y120_Lower;
x140old_Lower=x140_Lower; y140old_Lower=y140_Lower;
x160old_Lower=x160_Lower; y160old_Lower=y160_Lower;
x180old_Lower=x180_Lower; y180old_Lower=y180_Lower;
x200old_Lower=x200_Lower; y200old_Lower=y200_Lower;
x220old_Lower=x220_Lower; y220old_Lower=y220_Lower;
x240old_Lower=x240_Lower; y240old_Lower=y240_Lower;
x260old_Lower=x260_Lower; y260old_Lower=y260_Lower;
x280old_Lower=x280_Lower; y280old_Lower=y280_Lower;
x300old_Lower=x300_Lower; y300old_Lower=y300_Lower;
x320old_Lower=x320_Lower; y320old_Lower=y320_Lower;
x340old_Lower=x340_Lower; y340old_Lower=y340_Lower;
x360old_Lower=x360_Lower; y360old_Lower=y360_Lower;
x380old_Lower=x380_Lower; y380old_Lower=y380_Lower;
x400old_Lower=x400_Lower; y400old_Lower=y400_Lower;

x80_Upper=NACA_63_815_profile_80_Upper(:,1); y80_Upper=NACA_63_815_profile_80_Upper(:,2);
x100_Upper=NACA_63_815_profile_100_Upper(:,1);
y100_Upper=NACA_63_815_profile_100_Upper(:,2);
x120_Upper=NACA_63_815_profile_120_Upper(:,1);
y120_Upper=NACA_63_815_profile_120_Upper(:,2);
x140_Upper=NACA_63_815_profile_140_Upper(:,1);
y140_Upper=NACA_63_815_profile_140_Upper(:,2);
x160_Upper=NACA_63_815_profile_160_Upper(:,1);
y160_Upper=NACA_63_815_profile_160_Upper(:,2);
x180_Upper=NACA_63_815_profile_180_Upper(:,1);
y180_Upper=NACA_63_815_profile_180_Upper(:,2);
x200_Upper=NACA_63_815_profile_200_Upper(:,1);
y200_Upper=NACA_63_815_profile_200_Upper(:,2);
x220_Upper=NACA_63_815_profile_220_Upper(:,1);
y220_Upper=NACA_63_815_profile_220_Upper(:,2);
x240_Upper=NACA_63_815_profile_240_Upper(:,1);
y240_Upper=NACA_63_815_profile_240_Upper(:,2);
x260_Upper=NACA_63_815_profile_260_Upper(:,1);
y260_Upper=NACA_63_815_profile_260_Upper(:,2);
x280_Upper=NACA_63_815_profile_280_Upper(:,1);
y280_Upper=NACA_63_815_profile_280_Upper(:,2);
x300_Upper=NACA_63_815_profile_300_Upper(:,1);
y300_Upper=NACA_63_815_profile_300_Upper(:,2);
x320_Upper=NACA_63_815_profile_320_Upper(:,1);
y320_Upper=NACA_63_815_profile_320_Upper(:,2);
x340_Upper=NACA_63_815_profile_340_Upper(:,1);
y340_Upper=NACA_63_815_profile_340_Upper(:,2);
x360_Upper=NACA_63_815_profile_360_Upper(:,1);
y360_Upper=NACA_63_815_profile_360_Upper(:,2);
x380_Upper=NACA_63_815_profile_380_Upper(:,1);
y380_Upper=NACA_63_815_profile_380_Upper(:,2);
x400_Upper=NACA_63_815_profile_400_Upper(:,1);
y400_Upper=NACA_63_815_profile_400_Upper(:,2);

x80_Lower=NACA_63_815_profile_80_Lower(:,1); y80_Lower=NACA_63_815_profile_80_Lower(:,2);
```

```
x100_Lower=NACA_63_815_profile_100_Lower(:,1);
y100_Lower=NACA_63_815_profile_100_Lower(:,2);
x120_Lower=NACA_63_815_profile_120_Lower(:,1);
y120_Lower=NACA_63_815_profile_120_Lower(:,2);
x140_Lower=NACA_63_815_profile_140_Lower(:,1);
y140_Lower=NACA_63_815_profile_140_Lower(:,2);
x160_Lower=NACA_63_815_profile_160_Lower(:,1);
y160_Lower=NACA_63_815_profile_160_Lower(:,2);
x180_Lower=NACA_63_815_profile_180_Lower(:,1);
y180_Lower=NACA_63_815_profile_180_Lower(:,2);
x200_Lower=NACA_63_815_profile_200_Lower(:,1);
y200_Lower=NACA_63_815_profile_200_Lower(:,2);
x220_Lower=NACA_63_815_profile_220_Lower(:,1);
y220_Lower=NACA_63_815_profile_220_Lower(:,2);
x240_Lower=NACA_63_815_profile_240_Lower(:,1);
y240_Lower=NACA_63_815_profile_240_Lower(:,2);
x260_Lower=NACA_63_815_profile_260_Lower(:,1);
y260_Lower=NACA_63_815_profile_260_Lower(:,2);
x280_Lower=NACA_63_815_profile_280_Lower(:,1);
y280_Lower=NACA_63_815_profile_280_Lower(:,2);
x300_Lower=NACA_63_815_profile_300_Lower(:,1);
y300_Lower=NACA_63_815_profile_300_Lower(:,2);
x320_Lower=NACA_63_815_profile_320_Lower(:,1);
y320_Lower=NACA_63_815_profile_320_Lower(:,2);
x340_Lower=NACA_63_815_profile_340_Lower(:,1);
y340_Lower=NACA_63_815_profile_340_Lower(:,2);
x360_Lower=NACA_63_815_profile_360_Lower(:,1);
y360_Lower=NACA_63_815_profile_360_Lower(:,2);
x380_Lower=NACA_63_815_profile_380_Lower(:,1);
y380_Lower=NACA_63_815_profile_380_Lower(:,2);
x400_Lower=NACA_63_815_profile_400_Lower(:,1);
y400_Lower=NACA_63_815_profile_400_Lower(:,2);

figure(4)
title('17 Blade Cross Section Profiles - NACA 63-815','fontweight','bold','fontsize',18)
xlabel('Horizontal Distance [mm]','fontweight','bold','fontsize',14)
ylabel('Vertical Distance [mm]','fontweight','bold','fontsize',14)
hold on

% plot(x240_Upper,y240_Upper,'k',x240_Lower,y240_Lower,'k');

plot(x80_Upper,y80_Upper,'k',x100_Upper,y100_Upper,'k',x120_Upper,y120_Upper,'k',...
    x140_Upper,y140_Upper,'k',x160_Upper,y160_Upper,'k',x180_Upper,y180_Upper,'k',...
    x200_Upper,y200_Upper,'k',x220_Upper,y220_Upper,'k',x240_Upper,y240_Upper,'k',...
    x260_Upper,y260_Upper,'k',x280_Upper,y280_Upper,'k',x300_Upper,y300_Upper,'k',...
    x320_Upper,y320_Upper,'k',x340_Upper,y340_Upper,'k',x360_Upper,y360_Upper,'k',...
    x380_Upper,y380_Upper,'k',x400_Upper,y400_Upper,'k',...
    x80_Lower,y80_Lower,'k',x100_Lower,y100_Lower,'k',x120_Lower,y120_Lower,'k',...
    x140_Lower,y140_Lower,'k',x160_Lower,y160_Lower,'k',x180_Lower,y180_Lower,'k',...
    x200_Lower,y200_Lower,'k',x220_Lower,y220_Lower,'k',x240_Lower,y240_Lower,'k',...
    x260_Lower,y260_Lower,'k',x280_Lower,y280_Lower,'k',x300_Lower,y300_Lower,'k',...
    x320_Lower,y320_Lower,'k',x340_Lower,y340_Lower,'k',x360_Lower,y360_Lower,'k',...
    x380_Lower,y380_Lower,'k',x400_Lower,y400_Lower,'k');

r80_Upper(:,1)=x80_Upper; r80_Upper(:,2)=y80_Upper;
```

```
r100_Upper(:,1)=x100_Upper; r100_Upper(:,2)=y100_Upper;
r120_Upper(:,1)=x120_Upper; r120_Upper(:,2)=y120_Upper;
r140_Upper(:,1)=x140_Upper; r140_Upper(:,2)=y140_Upper;
r160_Upper(:,1)=x160_Upper; r160_Upper(:,2)=y160_Upper;
r180_Upper(:,1)=x180_Upper; r180_Upper(:,2)=y180_Upper;
r200_Upper(:,1)=x200_Upper; r200_Upper(:,2)=y200_Upper;
r220_Upper(:,1)=x220_Upper; r220_Upper(:,2)=y220_Upper;
r240_Upper(:,1)=x240_Upper; r240_Upper(:,2)=y240_Upper;
r260_Upper(:,1)=x260_Upper; r260_Upper(:,2)=y260_Upper;
r280_Upper(:,1)=x280_Upper; r280_Upper(:,2)=y280_Upper;
r300_Upper(:,1)=x300_Upper; r300_Upper(:,2)=y300_Upper;
r320_Upper(:,1)=x320_Upper; r320_Upper(:,2)=y320_Upper;
r340_Upper(:,1)=x340_Upper; r340_Upper(:,2)=y340_Upper;
r360_Upper(:,1)=x360_Upper; r360_Upper(:,2)=y360_Upper;
r380_Upper(:,1)=x380_Upper; r380_Upper(:,2)=y380_Upper;
r400_Upper(:,1)=x400_Upper; r400_Upper(:,2)=y400_Upper;

r80_Lower(:,1)=x80_Lower; r80_Lower(:,2)=y80_Lower;
r100_Lower(:,1)=x100_Lower; r100_Lower(:,2)=y100_Lower;
r120_Lower(:,1)=x120_Lower; r120_Lower(:,2)=y120_Lower;
r140_Lower(:,1)=x140_Lower; r140_Lower(:,2)=y140_Lower;
r160_Lower(:,1)=x160_Lower; r160_Lower(:,2)=y160_Lower;
r180_Lower(:,1)=x180_Lower; r180_Lower(:,2)=y180_Lower;
r200_Lower(:,1)=x200_Lower; r200_Lower(:,2)=y200_Lower;
r220_Lower(:,1)=x220_Lower; r220_Lower(:,2)=y220_Lower;
r240_Lower(:,1)=x240_Lower; r240_Lower(:,2)=y240_Lower;
r260_Lower(:,1)=x260_Lower; r260_Lower(:,2)=y260_Lower;
r280_Lower(:,1)=x280_Lower; r280_Lower(:,2)=y280_Lower;
r300_Lower(:,1)=x300_Lower; r300_Lower(:,2)=y300_Lower;
r320_Lower(:,1)=x320_Lower; r320_Lower(:,2)=y320_Lower;
r340_Lower(:,1)=x340_Lower; r340_Lower(:,2)=y340_Lower;
r360_Lower(:,1)=x360_Lower; r360_Lower(:,2)=y360_Lower;
r380_Lower(:,1)=x380_Lower; r380_Lower(:,2)=y380_Lower;
r400_Lower(:,1)=x400_Lower; r400_Lower(:,2)=y400_Lower;


%% I have commented this out to assure that the good profiles don't get erased due to changes in the code.
% If a change is needed, remove the comments. The code will still work and
% output profiles
%
% save('Sections/r80_Upper.txt','r80_Upper','-ASCII')
% save('Sections/r100_Upper.txt','r100_Upper','-ASCII')
% save('Sections/r120_Upper.txt','r120_Upper','-ASCII')
% save('Sections/r140_Upper.txt','r140_Upper','-ASCII')
% save('Sections/r160_Upper.txt','r160_Upper','-ASCII')
% save('Sections/r180_Upper.txt','r180_Upper','-ASCII')
% save('Sections/r200_Upper.txt','r200_Upper','-ASCII')
% save('Sections/r220_Upper.txt','r220_Upper','-ASCII')
% save('Sections/r240_Upper.txt','r240_Upper','-ASCII')
% save('Sections/r260_Upper.txt','r260_Upper','-ASCII')
% save('Sections/r280_Upper.txt','r280_Upper','-ASCII')
% save('Sections/r300_Upper.txt','r300_Upper','-ASCII')
% save('Sections/r320_Upper.txt','r320_Upper','-ASCII')
% save('Sections/r340_Upper.txt','r340_Upper','-ASCII')
% save('Sections/r360_Upper.txt','r360_Upper','-ASCII')
```

```
% save('Sections/r380_Upper.txt','r380_Upper','-ASCII')
% save('Sections/r400_Upper.txt','r400_Upper','-ASCII')
%
% save('Sections/r80_Lower.txt','r80_Lower','-ASCII')
% save('Sections/r100_Lower.txt','r100_Lower','-ASCII')
% save('Sections/r120_Lower.txt','r120_Lower','-ASCII')
% save('Sections/r140_Lower.txt','r140_Lower','-ASCII')
% save('Sections/r160_Lower.txt','r160_Lower','-ASCII')
% save('Sections/r180_Lower.txt','r180_Lower','-ASCII')
% save('Sections/r200_Lower.txt','r200_Lower','-ASCII')
% save('Sections/r220_Lower.txt','r220_Lower','-ASCII')
% save('Sections/r240_Lower.txt','r240_Lower','-ASCII')
% save('Sections/r260_Lower.txt','r260_Lower','-ASCII')
% save('Sections/r280_Lower.txt','r280_Lower','-ASCII')
% save('Sections/r300_Lower.txt','r300_Lower','-ASCII')
% save('Sections/r320_Lower.txt','r320_Lower','-ASCII')
% save('Sections/r340_Lower.txt','r340_Lower','-ASCII')
% save('Sections/r360_Lower.txt','r360_Lower','-ASCII')
% save('Sections/r380_Lower.txt','r380_Lower','-ASCII')
% save('Sections/r400_Lower.txt','r400_Lower','-ASCII')
```

Appendix B: Blade profile linearization code

This Matlab code inputs the six profiles and applies a linear distribution. This blends the profiles together, starting with NACA 63-824 at the blade root and ending with NACA 63-812 at the blade tip.

```
clc; clear all; close all;

%This section loads the appropriate profiles for the sections

r80_63_824_Upper=load('NACA_63_824/r80_Upper.txt');
r100_63_824_Upper=load('NACA_63_824/r100_Upper.txt');
r120_63_824_Upper=load('NACA_63_824/r120_Upper.txt');
r140_63_824_Upper=load('NACA_63_824/r140_Upper.txt');

r80_63_824_Lower=load('NACA_63_824/r80_Lower.txt');
r100_63_824_Lower=load('NACA_63_824/r100_Lower.txt');
r120_63_824_Lower=load('NACA_63_824/r120_Lower.txt');
r140_63_824_Lower=load('NACA_63_824/r140_Lower.txt');

r100_63_821_Upper=load('NACA_63_821/r100_Upper.txt');
r120_63_821_Upper=load('NACA_63_821/r120_Upper.txt');
r140_63_821_Upper=load('NACA_63_821/r140_Upper.txt');
r160_63_821_Upper=load('NACA_63_821/r160_Upper.txt');
r180_63_821_Upper=load('NACA_63_821/r180_Upper.txt');
r200_63_821_Upper=load('NACA_63_821/r200_Upper.txt');
r220_63_821_Upper=load('NACA_63_821/r220_Upper.txt');

r100_63_821_Lower=load('NACA_63_821/r100_Lower.txt');
r120_63_821_Lower=load('NACA_63_821/r120_Lower.txt');
r140_63_821_Lower=load('NACA_63_821/r140_Lower.txt');
r160_63_821_Lower=load('NACA_63_821/r160_Lower.txt');
r180_63_821_Lower=load('NACA_63_821/r180_Lower.txt');
r200_63_821_Lower=load('NACA_63_821/r200_Lower.txt');
r220_63_821_Lower=load('NACA_63_821/r220_Lower.txt');

r180_63_818_Upper=load('NACA_63_818/r180_Upper.txt');
r200_63_818_Upper=load('NACA_63_818/r200_Upper.txt');
r220_63_818_Upper=load('NACA_63_818/r220_Upper.txt');
r240_63_818_Upper=load('NACA_63_818/r240_Upper.txt');
r260_63_818_Upper=load('NACA_63_818/r260_Upper.txt');
r280_63_818_Upper=load('NACA_63_818/r280_Upper.txt');
r300_63_818_Upper=load('NACA_63_818/r300_Upper.txt');

r180_63_818_Lower=load('NACA_63_818/r180_Lower.txt');
r200_63_818_Lower=load('NACA_63_818/r200_Lower.txt');
r220_63_818_Lower=load('NACA_63_818/r220_Lower.txt');
r240_63_818_Lower=load('NACA_63_818/r240_Lower.txt');
r260_63_818_Lower=load('NACA_63_818/r260_Lower.txt');
r280_63_818_Lower=load('NACA_63_818/r280_Lower.txt');
```

```
r300_63_818_Lower=load('NACA_63_818/r300_Lower.txt');

r260_63_815_Upper=load('NACA_63_815/r260_Upper.txt');
r280_63_815_Upper=load('NACA_63_815/r280_Upper.txt');
r300_63_815_Upper=load('NACA_63_815/r300_Upper.txt');
r320_63_815_Upper=load('NACA_63_815/r320_Upper.txt');
r340_63_815_Upper=load('NACA_63_815/r340_Upper.txt');
r360_63_815_Upper=load('NACA_63_815/r360_Upper.txt');
r380_63_815_Upper=load('NACA_63_815/r380_Upper.txt');

r260_63_815_Lower=load('NACA_63_815/r260_Lower.txt');
r280_63_815_Lower=load('NACA_63_815/r280_Lower.txt');
r300_63_815_Lower=load('NACA_63_815/r300_Lower.txt');
r320_63_815_Lower=load('NACA_63_815/r320_Lower.txt');
r340_63_815_Lower=load('NACA_63_815/r340_Lower.txt');
r360_63_815_Lower=load('NACA_63_815/r360_Lower.txt');
r380_63_815_Lower=load('NACA_63_815/r380_Lower.txt');

r340_63_812_Upper=load('NACA_63_812/r340_Upper.txt');
r360_63_812_Upper=load('NACA_63_812/r360_Upper.txt');
r380_63_812_Upper=load('NACA_63_812/r380_Upper.txt');
r400_63_812_Upper=load('NACA_63_812/r400_Upper.txt');

r340_63_812_Lower=load('NACA_63_812/r340_Lower.txt');
r360_63_812_Lower=load('NACA_63_812/r360_Lower.txt');
r380_63_812_Lower=load('NACA_63_812/r380_Lower.txt');
r400_63_812_Lower=load('NACA_63_812/r400_Lower.txt');
%%

r80_Upper=r80_63_824_Upper;
r100_Upper=0.75.*r100_63_824_Upper+0.25.*r100_63_821_Upper;
r120_Upper=0.5.*r120_63_824_Upper+0.5.*r120_63_821_Upper;
r140_Upper=0.25.*r140_63_824_Upper+0.75.*r140_63_821_Upper;
r160_Upper=r160_63_821_Upper;

r80_Lower=r80_63_824_Lower;
r100_Lower=0.75.*r100_63_824_Lower+0.25.*r100_63_821_Lower;
r120_Lower=0.5.*r120_63_824_Lower+0.5.*r120_63_821_Lower;
r140_Lower=0.25.*r140_63_824_Lower+0.75.*r140_63_821_Lower;
r160_Lower=r160_63_821_Lower;

r180_Upper=0.75.*r180_63_821_Upper+0.25.*r180_63_818_Upper;
r200_Upper=0.5.*r200_63_821_Upper+0.5.*r200_63_818_Upper;
r220_Upper=0.25.*r220_63_821_Upper+0.75.*r220_63_818_Upper;
r240_Upper=r240_63_818_Upper;

r180_Lower=0.75.*r180_63_821_Lower+0.25.*r180_63_818_Lower;
r200_Lower=0.5.*r200_63_821_Lower+0.5.*r200_63_818_Lower;
r220_Lower=0.25.*r220_63_821_Lower+0.75.*r220_63_818_Lower;
r240_Lower=r240_63_818_Lower;

r260_Upper=0.75.*r260_63_818_Upper+0.25.*r260_63_815_Upper;
r280_Upper=0.5.*r280_63_818_Upper+0.5.*r280_63_815_Upper;
r300_Upper=0.25.*r300_63_818_Upper+0.75.*r300_63_815_Upper;
```

```
r320_Upper=r320_63_815_Upper;

r260_Lower=0.75.*r260_63_818_Lower+0.25.*r260_63_815_Lower;
r280_Lower=0.5.*r280_63_818_Lower+0.5.*r280_63_815_Lower;
r300_Lower=0.25.*r300_63_818_Lower+0.75.*r300_63_815_Lower;
r320_Lower=r320_63_815_Lower;

r340_Upper=0.75.*r340_63_815_Upper+0.25.*r340_63_812_Upper;
r360_Upper=0.5.*r360_63_815_Upper+0.5.*r360_63_812_Upper;
r380_Upper=0.25.*r380_63_815_Upper+0.75.*r380_63_812_Upper;
r400_Upper=r400_63_812_Upper;

r340_Lower=0.75.*r340_63_815_Lower+0.25.*r340_63_812_Lower;
r360_Lower=0.5.*r360_63_815_Lower+0.5.*r360_63_812_Lower;
r380_Lower=0.25.*r380_63_815_Lower+0.75.*r380_63_812_Lower;
r400_Lower=r400_63_812_Lower;


%% This section is for plotting purposes

x80_Upper=r80_Upper(:,1); y80_Upper=r80_Upper(:,2);
x100_Upper=r100_Upper(:,1); y100_Upper=r100_Upper(:,2);
x120_Upper=r120_Upper(:,1); y120_Upper=r120_Upper(:,2);
x140_Upper=r140_Upper(:,1); y140_Upper=r140_Upper(:,2);
x160_Upper=r160_Upper(:,1); y160_Upper=r160_Upper(:,2);
x180_Upper=r180_Upper(:,1); y180_Upper=r180_Upper(:,2);
x200_Upper=r200_Upper(:,1); y200_Upper=r200_Upper(:,2);
x220_Upper=r220_Upper(:,1); y220_Upper=r220_Upper(:,2);
x240_Upper=r240_Upper(:,1); y240_Upper=r240_Upper(:,2);
x260_Upper=r260_Upper(:,1); y260_Upper=r260_Upper(:,2);
x280_Upper=r280_Upper(:,1); y280_Upper=r280_Upper(:,2);
x300_Upper=r300_Upper(:,1); y300_Upper=r300_Upper(:,2);
x320_Upper=r320_Upper(:,1); y320_Upper=r320_Upper(:,2);
x340_Upper=r340_Upper(:,1); y340_Upper=r340_Upper(:,2);
x360_Upper=r360_Upper(:,1); y360_Upper=r360_Upper(:,2);
x380_Upper=r380_Upper(:,1); y380_Upper=r380_Upper(:,2);
x400_Upper=r400_Upper(:,1); y400_Upper=r400_Upper(:,2);

x80_Lower=r80_Lower(:,1); y80_Lower=r80_Lower(:,2);
x100_Lower=r100_Lower(:,1); y100_Lower=r100_Lower(:,2);
x120_Lower=r120_Lower(:,1); y120_Lower=r120_Lower(:,2);
x140_Lower=r140_Lower(:,1); y140_Lower=r140_Lower(:,2);
x160_Lower=r160_Lower(:,1); y160_Lower=r160_Lower(:,2);
x180_Lower=r180_Lower(:,1); y180_Lower=r180_Lower(:,2);
x200_Lower=r200_Lower(:,1); y200_Lower=r200_Lower(:,2);
x220_Lower=r220_Lower(:,1); y220_Lower=r220_Lower(:,2);
x240_Lower=r240_Lower(:,1); y240_Lower=r240_Lower(:,2);
x260_Lower=r260_Lower(:,1); y260_Lower=r260_Lower(:,2);
x280_Lower=r280_Lower(:,1); y280_Lower=r280_Lower(:,2);
x300_Lower=r300_Lower(:,1); y300_Lower=r300_Lower(:,2);
x320_Lower=r320_Lower(:,1); y320_Lower=r320_Lower(:,2);
x340_Lower=r340_Lower(:,1); y340_Lower=r340_Lower(:,2);
x360_Lower=r360_Lower(:,1); y360_Lower=r360_Lower(:,2);
x380_Lower=r380_Lower(:,1); y380_Lower=r380_Lower(:,2);
```

```
x400_Lower=r400_Lower(:,1); y400_Lower=r400_Lower(:,2);

% figure(1)
% title('17 Linearly Distributed Blade Cross Section Profiles','fontweight','bold','fontsize',18)
% xlabel('Horizontal Distance [mm]','fontweight','bold','fontsize',14)
% ylabel('Vertical Distance [mm]','fontweight','bold','fontsize',14)
% hold on
% plot(x160_Upper,y160_Upper,'k',x160_Lower,y160_Lower,'k');

figure(2)
title('17 Linearly Distributed Blade Cross Section Profiles','fontweight','bold','fontsize',32)
xlabel('Horizontal Distance [mm]','fontweight','bold','fontsize',28)
ylabel('Vertical Distance [mm]','fontweight','bold','fontsize',28)
hold on
box on
plot(x80_Upper,y80_Upper,'k',x100_Upper,y100_Upper,'k',x120_Upper,y120_Upper,'k',...
    x140_Upper,y140_Upper,'k',x160_Upper,y160_Upper,'k',x180_Upper,y180_Upper,'k',...
    x200_Upper,y200_Upper,'k',x220_Upper,y220_Upper,'k',x240_Upper,y240_Upper,'k',...
    x260_Upper,y260_Upper,'k',x280_Upper,y280_Upper,'k',x300_Upper,y300_Upper,'k',...
    x320_Upper,y320_Upper,'k',x340_Upper,y340_Upper,'k',x360_Upper,y360_Upper,'k',...
    x380_Upper,y380_Upper,'k',x400_Upper,y400_Upper,'k',...
    x80_Lower,y80_Lower,'k',x100_Lower,y100_Lower,'k',x120_Lower,y120_Lower,'k',...
    x140_Lower,y140_Lower,'k',x160_Lower,y160_Lower,'k',x180_Lower,y180_Lower,'k',...
    x200_Lower,y200_Lower,'k',x220_Lower,y220_Lower,'k',x240_Lower,y240_Lower,'k',...
    x260_Lower,y260_Lower,'k',x280_Lower,y280_Lower,'k',x300_Lower,y300_Lower,'k',...
    x320_Lower,y320_Lower,'k',x340_Lower,y340_Lower,'k',x360_Lower,y360_Lower,'k',...
    x380_Lower,y380_Lower,'k',x400_Lower,y400_Lower,'k');
set(gca,'fontsize',20)

% This plot is for putting in reports where an extra title is unneccesary
figure(3)
xlabel('Horizontal Distance [mm]','fontweight','bold','fontsize',36)
ylabel('Vertical Distance [mm]','fontweight','bold','fontsize',36)
hold on
box on
point=0;
plot(x80_Upper,y80_Upper,'k',x100_Upper,y100_Upper,'k',x120_Upper,y120_Upper,'k',...
    x140_Upper,y140_Upper,'k',x160_Upper,y160_Upper,'k',x180_Upper,y180_Upper,'k',...
    x200_Upper,y200_Upper,'k',x220_Upper,y220_Upper,'k',x240_Upper,y240_Upper,'k',...
    x260_Upper,y260_Upper,'k',x280_Upper,y280_Upper,'k',x300_Upper,y300_Upper,'k',...
    x320_Upper,y320_Upper,'k',x340_Upper,y340_Upper,'k',x360_Upper,y360_Upper,'k',...
    x380_Upper,y380_Upper,'k',x400_Upper,y400_Upper,'k',...
    x80_Lower,y80_Lower,'k',x100_Lower,y100_Lower,'k',x120_Lower,y120_Lower,'k',...
    x140_Lower,y140_Lower,'k',x160_Lower,y160_Lower,'k',x180_Lower,y180_Lower,'k',...
    x200_Lower,y200_Lower,'k',x220_Lower,y220_Lower,'k',x240_Lower,y240_Lower,'k',...
    x260_Lower,y260_Lower,'k',x280_Lower,y280_Lower,'k',x300_Lower,y300_Lower,'k',...
    x320_Lower,y320_Lower,'k',x340_Lower,y340_Lower,'k',x360_Lower,y360_Lower,'k',...
    x380_Lower,y380_Lower,'k',x400_Lower,y400_Lower,'k');
set(gca,'fontsize',30)


h=plot(point,point,'.','MarkerSize',75);

%% I've commented this out to ensure good profiles don't get overwritten if there is a change to the code
```

```
% save('Sections/r80_Upper.txt','r80_Upper','-ASCII')
% save('Sections/r100_Upper.txt','r100_Upper','-ASCII')
% save('Sections/r120_Upper.txt','r120_Upper','-ASCII')
% save('Sections/r140_Upper.txt','r140_Upper','-ASCII')
% save('Sections/r160_Upper.txt','r160_Upper','-ASCII')
% save('Sections/r180_Upper.txt','r180_Upper','-ASCII')
% save('Sections/r200_Upper.txt','r200_Upper','-ASCII')
% save('Sections/r220_Upper.txt','r220_Upper','-ASCII')
% save('Sections/r240_Upper.txt','r240_Upper','-ASCII')
% save('Sections/r260_Upper.txt','r260_Upper','-ASCII')
% save('Sections/r280_Upper.txt','r280_Upper','-ASCII')
% save('Sections/r300_Upper.txt','r300_Upper','-ASCII')
% save('Sections/r320_Upper.txt','r320_Upper','-ASCII')
% save('Sections/r340_Upper.txt','r340_Upper','-ASCII')
% save('Sections/r360_Upper.txt','r360_Upper','-ASCII')
% save('Sections/r380_Upper.txt','r380_Upper','-ASCII')
% save('Sections/r400_Upper.txt','r400_Upper','-ASCII')
%
% save('Sections/r80_Lower.txt','r80_Lower','-ASCII')
% save('Sections/r100_Lower.txt','r100_Lower','-ASCII')
% save('Sections/r120_Lower.txt','r120_Lower','-ASCII')
% save('Sections/r140_Lower.txt','r140_Lower','-ASCII')
% save('Sections/r160_Lower.txt','r160_Lower','-ASCII')
% save('Sections/r180_Lower.txt','r180_Lower','-ASCII')
% save('Sections/r200_Lower.txt','r200_Lower','-ASCII')
% save('Sections/r220_Lower.txt','r220_Lower','-ASCII')
% save('Sections/r240_Lower.txt','r240_Lower','-ASCII')
% save('Sections/r260_Lower.txt','r260_Lower','-ASCII')
% save('Sections/r280_Lower.txt','r280_Lower','-ASCII')
% save('Sections/r300_Lower.txt','r300_Lower','-ASCII')
% save('Sections/r320_Lower.txt','r320_Lower','-ASCII')
% save('Sections/r340_Lower.txt','r340_Lower','-ASCII')
% save('Sections/r360_Lower.txt','r360_Lower','-ASCII')
% save('Sections/r380_Lower.txt','r380_Lower','-ASCII')
% save('Sections/r400_Lower.txt','r400_Lower','-ASCII')
```

Appendix C: CEL Example

This is an example of CFX expression language (CEL) used during pre-processing and post-processing. The use of CEL can reduce complications with pre-processing as well as allowing user defined functions during post-processing.

```
LIBRARY:
  CEL:
    EXPRESSIONS:
        A = 0.502655
        Accumulated Time Step = 721
        Angular Velocity = -RotSpeed [radian s^-1]
        CoPow = (RotSpeed*Torque)/(0.5*rho*A*(velo^3))
        CoThrust = (force_z()@Turbine Wall)/(0.5*rho*A*(velo^2))
        Current Time Step = 721
        Radi = 0.4
        Reference Pressure = 1 [atm]
        RotSpeed = TSR*velo/Radi
        Sequence Step = 721
        TSR = 6
        Time = 0 [s]
        Torque = torque_z()@Turbine Wall
        Vel Deficit = 1[m s^-1]-vNorm
        VortNorm = (Vorticity*2*Radi)/(velo)
        atstep = Accumulated Time Step
        ctstep = Current Time Step
        omega = Angular Velocity
        rho = 997
        sstep = Sequence Step
        t = Time
        turbIntensity = (100/velo)*sqrt((2/3)*(Turbulence Kinetic Energy))
        turbNorm = (Turbulence Kinetic Energy)/(velo^2)
        vNorm = (Velocity in Stn Frame)/velo
        velo = 1.54    END
  END
END
```